Univerzita Karlova v Praze

Přírodovědecká fakulta

BAKALÁŘSKÁ PRÁCE

Dorota Kaščáková

Příprava a charakterizace nanokompozitů oxidu železitého substituovaného skandiem

Katedra anorganické chemie

Vedoucí bakalářské práce:	RNDr. Daniel Nižňanský, Ph.D.
Konzultant:	RNDr. Jana Kalbáčová Vejpravová, Ph.D.
Studijní obor:	Chemie v přírodních vědách

Praha 2014

Charles University in Prague
Faculty of Science

BACHELOR THESIS

Dorota Kaščáková

Preparation and Characterization of Iron (III) Oxide Nanocomposites Substituted with Scandium

Department of Inorganic Chemistry

Supervisor: RNDr. Daniel Nižňanský, Ph.D.
Consultant: RNDr. Jana Kalbáčová Vejpravová, Ph.D.
Study programme: Chemistry in Natural Sciences

Prague 2014

Prohlašuji, že jsem tuto bakalářskou práci vypracovala samostatně pod vedením školitele RNDr. Daniela Nižňanského, Ph.D. a RNDr. Jany Vejpravové, Ph.D., že jsem uvedla všechny použité informační zdroje a literaturu.

Jsem si vědoma toho, že případné využití výsledků, získaných v této práci, mimo Univerzitu Karlovu v Praze je možné pouze po písemném souhlasu této univerzity.

V .... dne .... Dorota Kaščáková

I declare that I carried out this bachelor thesis independently under supervision of RNDr. Daniel Nižňanský, Ph.D. and RNDr. Jana Kalbáčová Vejpravová, Ph.D. and that I cited all used information and literary sources properly.

I am aware that any use of the results obtained in this work outside the Charles University in Prague is possible only with the written consent of the University.

In .... date .... Dorota Kaščáková

Název práce: Příprava a charakterizace nanokompozitů oxidu železitého substituovaného skandiem

Autor: Dorota Kaščáková

Katedra: Katedra anorganické chemie, PřF UK Praha

Vedoucí bakalářské práce: RNDr. Daniel Nižňanský, Ph.D.

Konzultant: RNDr. Jana Kalbáčová Vejpravová, Ph.D.

Abstrakt: Tato práce je zaměřena na přípravu a charakterizaci nanočástic oxidu železitého substituovaného skandiem v matrici SiO_2. Nanočástice byly připraveny metodou sol-gel a výsledkem byl převážně β-Fe_2O_3 substituovaný různým obsahem skandia.

Nanokompozity byly charakterizovány pomocí Mossbauerovy spektroskopie a magnetických měření a z výsledků práškové rentgenové difrakce byly vypočteny mřížkové parametry a velikost částic β-fáze substituované různým množstvím skandia.

β-Fe_2O_3 v daných systémech vzniká žíháním při teplotě 1000 °C a 1100 °C při složení $Fe_{2-x}Sc_xO_3$ když $x \geq 0.2$ a při žíhání na 1100 °C když $x = 0.1$. Mřížkový parametr substituované β-fáze je lineárně závislý na obsahu skandia a mění se rovněž s teplotou. Při žíhání na 1250 °C se takto připravený β-Fe_2O_3 mění na hematit.

Klíčová slova: oxid železitý, skandium, sol-gel, rtg. difrakce, Mossbauerova spektroskopie, magnetická měření

Title: Preparation and Characterization of Iron (III) Oxide Nanocomposites Substituted with Scandium

Author: Dorota Kaščáková

Department: Department of Inorganic Chemistry, Faculty of Science, Charles University of Prague

Supervisor: RNDr. Daniel Nižňanský, Ph.D.

Consultant: RNDr. Jana Kalbáčová Vejpravová, Ph.D.

Abstract:

In this work a preparation and characterization of nanoparticles of iron(III) oxide substituted with scandium in SiO_2 matrix is described. The nanoparticles were prepared by the sol–gel method yielding mostly β-Fe_2O_3 substituted with various amount of scandium(III) ions.

Mossbauer spectroscopy was carried out to determine purity of the samples and the content of other iron oxides phases. System was characterized by magnetic measurements. Powder X – ray diffraction was used to verify the composition and to determine the lattice parameter and particle size.

β-Fe_2O_3 is formed at the temperatures of 1000 and 1100 °C at composition $Fe_{2-x}Sc_xO_3$ for $x \geq 0.2$ and at temperature 1100 °C for $x = 0.1$. Lattice parameter is linearly dependent on the scandium content and depends also on the annealing temperature. At temperatures higher than 1250 °C, β-Fe_2O_3 is transformed into hematite.

Key words: iron(III) oxide, scandium, sol-gel, Mossbauer spectroscopy, X-ray diffraction, magnetic measurement

Content

1. Introduction

Besides two natural phases, α-Fe_2O_3 (hematite) and γ-Fe_2O_3 (maghemite), iron(III) oxide forms two other phases, ε- and β-Fe_2O_3, prepared only in laboratory. All these four phases find application in several fields as pigments, catalysts or magnetic recording media. The main reasons for the intensive studies of the iron(III) oxides are their surprising magnetic properties, especially in case of ε-Fe_2O_3, but also a possibility to study the relations between the crystal structure and magnetism. Eventual substitution of iron by other trivalent cations opens another dimension of research.

The studies concerning Fe_2O_3 have been focused mostly on ε-phase and the possibility to prepare the nanoparticles of this phase embedded in silica matrix has been known for several years. Later studies showed that substitution of iron by aluminium and galium influences the phase and magnetic transitions in the systems containing ε-Fe_2O_3.

This work aims to study the influence of substitution of iron by scandium to the phase relations in the Fe_2O_3/SiO_2 system, the influence on the phase and magnetic transitions and eventual stabilization of the iron(III) oxide phases.

2. Iron oxides

Iron, the most common transition metal in the Earth, forms 16 compounds that are either oxides, hydroxides or oxide-hydroxides, composed of Fe together with O and/or OH. Currently, six iron oxides are known; four iron(III) oxides: α-, β-, γ- and ε- Fe_2O_3, magnetite Fe_3O_4 and wüstite FeO [1]. These compounds have application in several fields. They have been widely used as inorganic pigments where the colour depends on crystallinity [2], they are used as catalysts for Fischer-Tropsch synthesis of hydrocarbons [3] and are considered a suitable material for anodes in photochemical cells.[4]

2.1 α-Fe_2O_3

α-Fe_2O_3, known as hematite, is the oldest known Fe oxide mineral. Its name comes from Greek haima - blood, because of its red colour when the mineral is finely ground. Hematite gives many rocks and soils their vivid yellow-red to purple-red colour. It is very stable and usually is the final product of transformation of other iron oxides.

Hematite has the corundum α-Al_2O_3 structure. Unit cell is hexagonal with $a = 0.5034$ nm and $c = 1.375$ nm, with six formula units per unit cell.

Space group is $R\bar{3}c$, and the structure can be described as hexagonal close packing array of oxygen ions, where planes of anions are parallel to the (001) plane. Fe^{III} fills two thirds of the sites regularly; two filled sites are followed by one vacant site in the (001) plane. This arrangement of cations forms pairs of FeO_6 octahedra. Each octahedron has common edges with three neighbouring octahedra in the same plane and shares one face with an octahedron in an adjacent plane. [1]

The unit cell of hematite viewed from different angles is shown in Fig. 2.1.

Figure 2.1: Hematite structure viewed from the c axis direction [5]

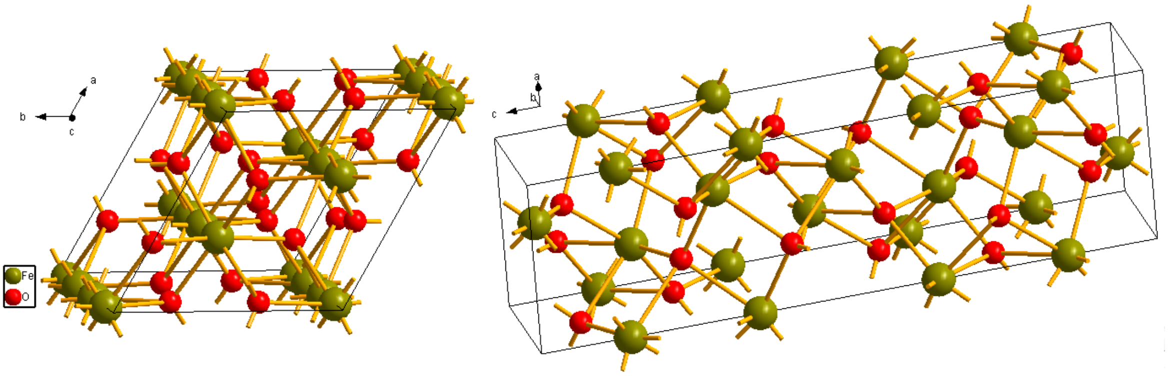

At temperatures above Curie temperature of 956 K, hematite is paramagnetic. Weakly ferromagnetic structure undergoes a phase transition to an antiferromagnetic state at 260 K. This temperature is known as Morin temperature. Particles smaller than 8 nm display superparamagnetic behaviour at room temperature. [1]

2.2 β-Fe_2O_3

Existence of β-phase was first reported by M. Bonnevie-Svendsen in 1958 [6]. Reaction with water vapour led to the hydrolytic decomposition of iron(III) chloride and to the formation of a new iron(III) oxide phase with diffractogram similar to that of β-Mn_2O_3. That's why the author suggested the name β-Fe_2O_3 for the new oxide.

His article was not noticed by Braun and Gallagher. In 1972 they published preparation of new iron(III) oxide phase by dehydroxylation of β-FeOOH, akaganéite, at 165-170°C under high vacuum. Porous tubular akaganéite crystals were prepared by hydrolysis of a dilute solution of iron(III) chloride and they contained large channels, that enabled the oxide hydroxide to decompose to the oxide by allowing the water to escape from the solid with minor disruption of the lattice.

Authors reported that the diffractogram of the new structure was remarkably similar to that of β-FeOOH. This was the reason why they also gave the new compound the name β-Fe_2O_3. At high vacuum the oxide was stable until 200 °C, where oxygen loss with production of Fe_3O_4 was observed. No oxygen loss occurred when heated in air or oxygen and the structure was stable until prolonged heating at 400 °C. Since γ-Fe_2O_3 is transformed to hematite more rapidly at this temperatures, authors suggested that the new phase was more stable than γ-Fe_2O_3 [7].

Recently, few works concerning preparation of β-Fe_2O_3 were published. However, only few reports describe obtaining a single phase, and magnetic properties were studied in very few works.

Carraro et al. [8] studied synthesis of layers of β- and ε-Fe_2O_3 deposited on different substrates using chemical vapour deposition method. Formation of the requested phase depends on the preparation conditions. The square-like pyramidal β-phase crystals were formed at 773 K in dry oxygen, the ε-phase crystals had the nanorods shape. Since the temperature growth of 100 °C led to phase transformation into hematite only in the ε systems, authors reported higher stability of β-phase compared to ε-Fe_2O_3 under these conditions.

Dependence of magnetisation on temperature in applied field of 50 kOe, parallel to the substrate surface of the β-Fe_2O_3 systems, was also studied in their work. Estimated Néel temperature was 117 K and the samples exhibited the behaviour typical for paramagnetic and antiferromagnetic state above and below T_N, respectively [8].

Ikeda et al. [9] reported preparation of pure β phase from mixture of $Fe_2(SO_4)_3$ and NaCl heated at 500 °C.

Significant contribution to this topic was brought by Danno et al. [10]. They prepared small particles of β-Fe_2O_3 from mixture of $NaFe(SO_4)_2$ with NaCl in different molar ratios heated at 350 and 500 °C for one hour. Decomposition was studied using differential thermogravimetric analysis. The mixture started to react at 320 °C, which was lower than the reaction temperature of $Fe_2(SO_4)_3$ and NaCl.

SEM pictures of the particles heated at 350 °C showed that the particles had granular shape and their size was between 50 and 100 nm. Particles prepared at 500 °C were cubic and their sizes reached up to 1 μm. TG/DTA analysis confirmed that formation of liquid phase at 490 °C was the reason of this significant difference.

Authors reported different Néel temperatures measuring dependence of magnetisation on temperature in applied field of 0.2 kOe. For the particles prepared at 500 °C estimated T_N was 119 K, the value consistent with other works; reported T_N for the smaller particles was 113 K [10].

Bréard et al. [17] studied the substitution of iron by scandium using the direct solid state synthesis. They prepared samples of composition $Fe_{2-x}Sc_xO_3$ in compositional steps Δx=0.2 by mixing the Fe_2O_3 and Sc_2O_3 powders in corresponding ratio and annealing at 1400 °C for 24 hours. The resulting phase had the bixbyite structure with iron and scandium atoms randomly distributed over the cation sites. In the cases where $x < 1$, hematite appeared as a secondary phase. Magnetic measurements showed that the magnetic lattice was frustrated and resembled cluster glass [17].

β-Fe_2O_3 has cubic structure with space group $Ia\bar{3}$, structural type bixbyite $(Mn,Fe)_2O_3$. Different authors report similar values of the lattice parameter: 9.3930 Å [12], 9.4039 Å [10] and 9.4040 Å [9].

Positions of the atoms in the structure are still ambiguous. The cubic unit contains 16 formula units per unit cell; 48 oxygen atoms in *e* sites and 32 iron atoms in two nonequivalent distorted octahedrons. 24 Fe^{3+} ions occupy C_2 symmetry *d* sites and 8 Fe^{3+} ions occupy C_{3i} symmetry sites. Danno et al. [10] and Ben-Dor et al. [13] report positions of the 8 ions in *b* sites, but the paper written by Danno et al. was later corrected. In [11] positions in *a* sites are obtained by Rietveld refinement on cubic-shaped crystals with particle size 1 μm. Positions in *a* sites are also reported in [12]. Positions in *b* sites are reported by Bréard et al. in [17].

Structure is metastable and undergoes a transition into hematite above temperatures about 550 °C. Different authors describe transformation of β- into α-Fe_2O_3 starting at 500 °C, completed at 600 °C[13]. In paper written by Danno et al. the transformation was described as fully completed at 700 °C because of the larger particles size [11].

Concerning magnetic properties, β-phase is the only phase of Fe_2O_3 that is paramagnetic at room temperature [8]. Below Néel temperature, which has been reported between 110 K and 119 K, the structure is antiferromagnetic. Due to the difficult preparation of the single β-phase, it is the least studied phase among iron(III) oxides.

2.3 γ-Fe_2O_3

The γ-phase, usually known as maghemite, is a red-brown mineral with a cubic structure. In nature, it occurs as a weathering product of magnetite, therefore it is isostructural with the magnetite structure, the difference is that all or most of iron atoms are present in oxidation state (III) and the charge is compensated by cation vacancies.

Maghemite can exist in three different structures, depending on the vacancies ordering. If the vacancies are randomly distributed over the crystal, space group is $Fd\bar{3}m$, what is typical for spinel; unit cell is cubic, with lattice parameter 8.3300 Å[14]. There are 32 oxygen atoms, 21 1/3 iron (III) ions and 2 1/3 vacancies in

Figure 2.2: β-phase structure viewed from the c axis direction [13]

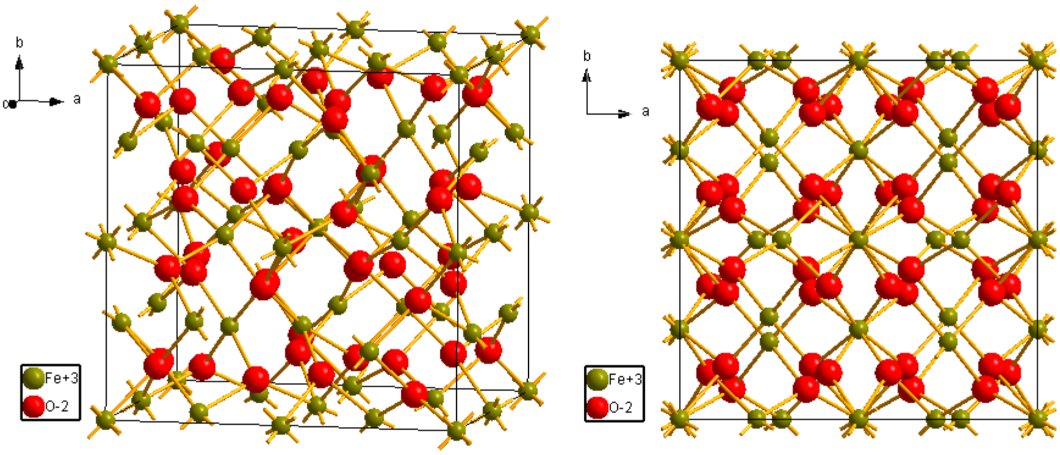

Figure 2.3: Maghemite structure viewed from the c axis direction (left) and a axis direction (right) [14]

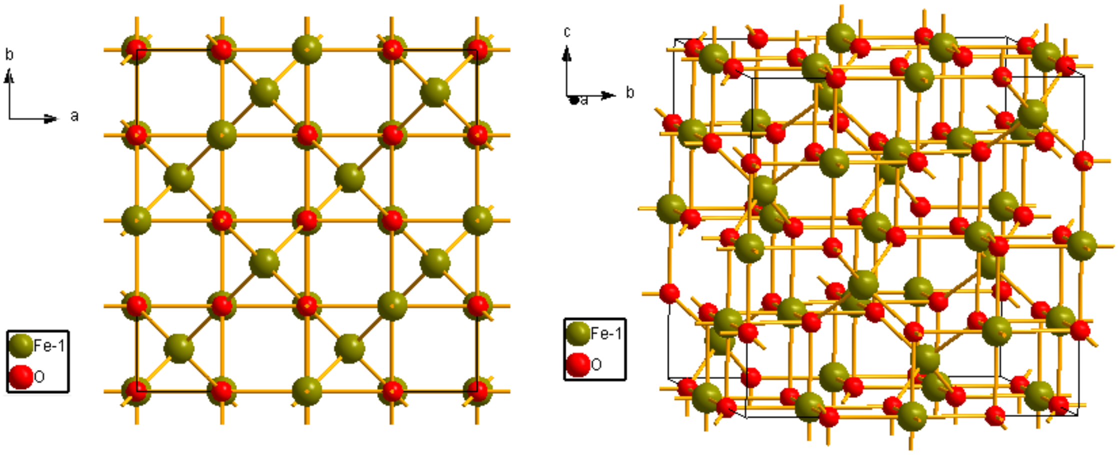

the unit cell. Eight cations occupy tetrahedral sites, the remaining cations are randomly distributed over the octahedral sites. If maghemite is prepared as small particles, the vacancies distribution is usually random and structure has the space group Fd$\bar{3}$m.

Vacancies ordering leads to the cubic space group P$4_3$32. The structure is sometimes reported as tetragonal with space group P$4_1 2_1$2, where the tetragonal unit cell is tripled along the c axis [1].

γ-Fe_2O_3 is ferrimagnetic at room temperature. Positions of iron in two different cation sites in the structure – tetrahedral and octahedral – lead to formation of two antiparallel magnetic sublattices. Curie temperature has not been estimated yet, because of transformation into hematite at temperatures above 500 °C. For its magnetic properties and low preparation costs, maghemite has been widely used in recording media [1].

2.4 ε-Fe_2O_3

This phase was first described in 1934 by Forestier & Guillot-Guillain. Its structure was first considered to be monoclinic, later works reported orthorhombic structure with space group $Pna2_1$, isostructural with $AlFeO_3$ and κ-Al_2O_3 [1]. Iron atoms occupy four different sites, three with octahedral and one with tetrahedral symmetry, leaving no vacancies in the unit cell. All of the cation polyhedra are distorted, what is believed to be the reason for its interesting magnetic properties [16].

On the Fig. 2.4, four tetrahedral Fe^{3+} ions can be seen. The other cations occupy octahedral sites. There are 8 formula units per unit cell [15].

Figure 2.4: ε-phase structure viewed along the a axis direction [15]

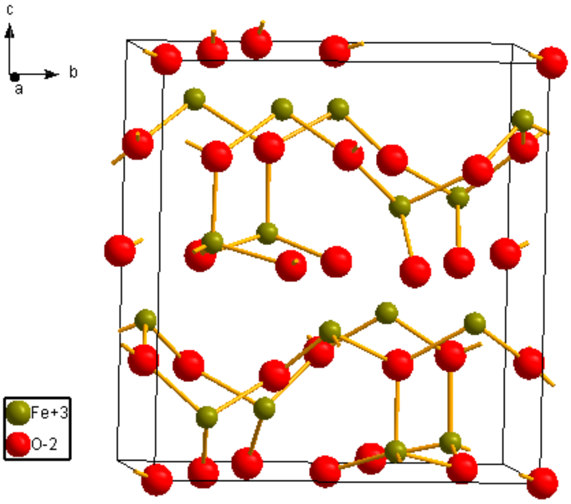

The magnetic behaviour is still not fully understood. At room temperature, the ε-phase behaves either as a collinear ferrimagnet or as a canted antiferromagnet [16]. The ferrimagnetic structure has coercive field of 2 T and Curie temperature 495 K. This giant room-temperature coercive field is a strategic feature for high-coercivity recording media and for use in tunable electric/magnetic field or multiple-state memory devices [8].

At approximately 110 K, the phase undergoes a magnetic transition, what leads to full loss of coercivity. At temperatures below 80 K, the coercivity rises to approximately 0.4 T. At 9 K, it behaves as a non-collinear ferrimagnet [18].

Similar to β-phase, ε-phase has not been found in nature and it can be only synthesized in laboratory in the form of nanomaterial. It is also metastable and transforms to hematite at 500-750 °C, depending on the preparation method [1]. However, ε-Fe_2O_3 nanoparticles embedded in silica matrix have been reported as stable at temperatures up to 1400 °C [19].

3. Sol-gel method of preparation of nanoparticles

Nanoparticles and metal clusters represent an important state of condensed matter. These systems display many special chemical and physical properties and specific behaviour that is not generally observed in bulk materials [20].

Nanostructures can be difficult to describe: on the one hand, they consist of too few atoms (usually thousands to hundreds of thousands) to describe their behaviour by the means of classical mechanics. On the other hand, they contain too many atoms to be described using simple quantum mechanics. The movement of electrons is significantly limited due to the small volume of the particle. That's why the nanostructures can exhibit different and often surprising behaviour compared to bulk materials.

Since nanochemistry is in a stage of rapid development, the exact difference between such terms as "cluster", "nanoparticle", and "quantum dot" are still evolving in the literature [20].

Sergeev [20] defines nanoparticles as "entities measuring from 1 to 10 nm and built of atoms of one or several elements," Kreibig [21] divides particles into four domains by the number of atoms and Takeo [22] divides particles with diameter smaller than 100 nm into three groups by comparing the number of surface atoms to those in the bulk. In general, the particles with diameter greater than 100 nm are called the bulk material [23].

There are two approaches to the synthesis of nanomaterials: bottom-up and top-down. Attrition, milling or etching belong to the typical top-down methods. However, using the physical way of preparation, there is a problem with imperfection of the crystal structure, with a significant impact on physical properties and surface chemistry [24].

Chemical route permits the manipulation with the material at the molecular level, what helps in achieving good chemical homogeneity . Special attention is paid to the synthesis of monodispersed particles [25]. The most used chemical methods of preparation of nanoparticles are coprecipitation, sol-gel, microemulsion synthesis, hydrothermal method and thermal decomposition in organic solvents [26].

3.1 Sol-gel

Sol-gel synthesis of nanoparticles was first described by Grimaux in 1884, when he prepared colloidal iron oxides from iron alkoxides. In 1923 W. A. Patrick synthesized porous catalysts using sol-gel method and his work was soon followed by many other papers and patents. [27]

Sol-gel method is a method of obtaining the ceramic materials by preparation of sol, gelation of the sol, and removal of the solvent. Sol, which means a colloidal suspension of solid particles in a liquid, can be produced from inorganic or organic precursors: nitrates, alkoxides etc.

Metal alkoxides, metalorganic compounds with organic ligand attached to a metal or metalloid atom, are common precursors because they react readily with water. Tetraethoxysilane (TEOS), $Si(OCH_2CH_3)_4$ is the most intensively studied metal alkoxide from those used in sol-gel science.

This compound was first prepared in 1845 by Ebelmen, who later described the hydrolysis and forming of amorphous gels that can be dried for a longer time to yield optical components [28].

The advantage of use of alkoxysilanes is their slower reaction with water; unlike the most of other metal alkoxides, they don't react with atmospheric water, what makes working with them much easier.

3.2 Mechanism of sol-gel reaction

In this chapter the reasons for the used experimental conditions will be illustrated. Mechanism of formation of gel can be described by three processes: hydrolysis, condensation and ageing. This three steps can be described using a few simple equations, but the actual process is much more complicated.

3.2.1 Hydrolysis

First step of the mechanism is the hydrolysis [27]. Oxygen from the water molecule attacks the Si-O bonds of the alkoxide to form silicic acid $Si(OH)_4$ and ethanol (or another alcohol) as a by-product following the equation:

$$\mathrm{Si(OR)_4 + 4\,H_2O \longrightarrow Si(OH)_4 + 4\,ROH} \tag{3.1}$$

The reaction can be catalyzed by acid:

$$\mathrm{H_2O + Si(OR)_4 + H^+ \longleftrightarrow [(H_2O)Si(OR)_3(ROH)]^+ \longleftrightarrow (HO)Si(OR)_3 + ROH + H^+} \tag{3.2}$$

or by a base:

$$\mathrm{Si(OR)_4 + OH^- \longleftrightarrow [(OH)Si(OR)_4]^- \longleftrightarrow (HO)Si(OR)_3 + OR^-} \tag{3.3}$$

Coltrain et al [29]. studied the effect of the catalysis by comparing reaction rates at various pH values. Since the isoelectric point of silica is at pH 2.2, the gelation time is the longest at this pH and rapidly decreases with both decreasing and increasing pH value.

The effect of substituent on the silicon atom was studied by Aelion et al [30]. They compared hydrolysis rate constants of the different silicon alkoxides with a conclusion that the larger alkoxy groups lead to higher steric repulsion and overcrowding of the transition state, and thus lead to slower reaction. The hydrolysis rate constant of tetramethoxysilane TMOS is the highest and it decreases with increasing length of organic chain.

A disadvantage of TEOS is the hydrophobic character of the ethoxy groups. Water and TEOS are immiscible in all proportions, and to enable hydrolysis, it is necessary to add a co-solvent to the system. As the co-solvents, alcohols are usually used, but using an alcohol different from that generated by hydrolysis, trans-esterification can occur and affect whole process. The choice of co-solvent also affects the drying process [27].

From the reaction stoichiometry in the equation 3.1, the molar ratio of water and alkoxide is 4. However, less water can be added since there is water produced in the condensation reaction. If the amount of water is very small, hydrolysis slows down due to low reactant concentration. When the amount of water is too high, the alkoxide as a reactant is diluted, and the reaction rate decreases. Generally, the smaller amounts of co-solvent lead to the higher reaction rate [27], [31].

3.2.2 Condensation

Partially hydrolysed TEOS starts polymerizing forming siloxane bonds. This process can occur either by the water-producing condensation:

$$\mathrm{Si(OEt)_3OH + HOSi(OEt)_3 \longleftrightarrow (EtO)_3SiOSi(OEt)_3 + H_2O} \tag{3.4}$$

or by the alcohol-producing condensation:

$$\mathrm{Si(OEt)_3OR + HOSi(OEt)_3 \longleftrightarrow (EtO)_3SiOSi(OEt)_3 + ROH} \tag{3.5}$$

As catalysts, many compounds were studied, generally compounds that exhibit acid or basic properties, but also neutral salts and transition metal alkoxides [28].

When acid or base catalysed, the reaction with H^+ or OH^- leads to formation of charged intermediate and it is followed by slow attack of a second neutral silicon species.

As for hydrolysis, the transition state of the the acid catalysed condensation is positively charged and stabilised by electron donating groups. That is why the compound $(RO)_3SiOH$ condenses faster than $(RO)_2Si(OH)_2$ which condenses faster than $(RO)Si(OH)_3$; the first step of condensation is the fastest. The result is an open network structure, that undergoes further hydrolysis and cross-condensation reactions.

In the base catalysed conditions, the negatively charged transition state becomes more stable as more hydroxy groups replace more electron donating alkoxy groups. The hydrolysis rate increases and the condensation reaction is fastest for the fully hydrolysed TEOS.

This mechanism shows that for the base catalysed reaction the highly cross-linked large sol particles are obtained. This particles can later link to form gels with large pores [27]. For example, using ammonia as catalyst, well known Stöber monodisperse SiO_2 spheres with typical opalescence and particles size between 0.05 μm and 2 μm for different experimental conditions can be obtained [32]

In real systems, condensation and hydrolysis proceed concurrently. Large number of compounds of the formula $[SiO_x(OH)_y(OR)_z]_n$, where $2x+y+z = 4$ exist together, what gives large number of reactions. That makes sol-gel process rather empirical and developing of full kinetic model for sol-gel method impossible [27].

3.2.3 Gelation

Gelation occurs when the silica sol particles produced by the hydrolysis and condensation link to form a giant cluster that fills the containing vessel. At this point, many sol particles are still not linked, entrapped in the giant cluster; this gel has high viscosity, but low elasticity and it doesn't pour out of vessel. There is no phase transition during gelation; only the viscosity increases progressively.

3.2.4 Ageing

The cross-linking of the sol-particles continues for long time after gelation. The time period depends on temperature, pH and gel composition. The net effect of these changes is stiffening and shrinkage of the sample because of forming covalent bonds instead of former interactions between surface hydroxy and alkoxy groups. Shrinkage leads to extrusion of solvent from the pores in the gel, if sealed, the gel appearance changes from homogeneous gel into solid monolith immersed in liquid [27].

3.3 Drying

Drying of the gelled sample proceeds in four main steps: The Constant Rate Period, The Critical Point, First Falling-Rate Period and Second Falling-Rate Period.

Initially a gel shrinks proportionally to amount of water and other liquids evaporated.

As the gel dries and shrinks, its stiffness increases. At the critical point, stiffness is strong enough to resist further shrinkage as liquid continues to evaporate. Liquid recedes into the porous structure and due to the surface tension, very large pressures up to 100 MPa are generated. At this point, if not carefully prepared, gel cracking occurs due to this capillary stress [27].

3.3.1 Cracking prevention

When one attempts to produce gel monolith using sol-gel process, fracture and crack formation is one of the most serious problems. It is caused by stress due to changes in pore size and by capillary forces arising from evaporation of the solvent and it can lead up to full disintegration of the gel [28].

From a number of methods developed in order to avoid cracking, three methods are the most frequently used.

The “slow rate evaporation method”, where evaporation of the solvent is very slow and carefully controlled, gives good results, but requires long processing times.

During supercritical drying, the solvent is removed under controlled pressure. This method is the fastest and the most reliable, but its industrial application is limited because of the practical difficulties.

Use of the *Drying Control Chemical Additives* DCCA's such as formamide, dimethylformamide, acetonitrile or oxalic acid allows drying at elevated temperatures and atmospheric pressure without crack formation [27].

3.3.2 Drying Control Chemical Additives

Firstly, DCCA's were used empirically without deep studies of their function. Later, it was shown that these agents influence the gel preparation at every stage, from hydrolysis up to drying and the mechanisms are very complex.

In the early stage of condensation, formamide stabilizes formation of oligomers and avoids random propagation of silica networks. Cross linking of these oligomers leads to a better organization at gelation and stronger Si-O bonds and hence to the lower sensitivity to drying stresses [33].

Since the DCCA causes the generation of large pores with narrow size distribution, capillary forces are weaker and the stress is smaller. Another mechanism of action is binding of the DCCA to the silica surface through hydrogen bonds. Preventing the interactions between water and silanol groups on the pore walls, it facilitates the water removal. Additionally, the pore fluid will contain DCCA, which lowers the surface tension of the liquid phase [27].

3.4 Nanocomposites with silica matrix

The sol-gel method produces porous materials with pore-size distribution that can be controlled using different reactants and by the processing conditions. If an inorganic solid is incorporated into the pores, composite of particles embedded in silica matrix with well-controlled size distribution can be obtained.

3.5 Leaching

Silica matrix from the nanocomposite can be removed using a conventional leaching process. If the particles embedded in the matrix don't react with sodium hydroxide, ground composite can be poured into high-concentrated solution of sodium hydroxide and heated over a sufficiently long time. Silicon oxide reacts with sodium hydroxide to form liquid glass.

Since sodium silicate is soluble in water, after washing and centrifugation individual nanoparticles can be obtained.

4. Characterization methods

4.1 Powder X-ray diffraction

In the synthesis of solid materials, especially inorganic, powder X-ray diffraction is the basic method of characterization of prepared material. For the preparation of nanoparticles, its main advantages are the possibility to measure polycrystallic and polyphase sample, the low amount of material that is needed for characterization and the possibility to estimate particles size.

The light emitted from the X-ray tube is diffracted on the polycrystallic sample. To diffract constructively, the angle of the incident radiation must meet the Bragg law:

$$2d\sin\theta = n\lambda, \quad n = 1, 2, 3... \tag{4.1}$$

where θ is the angle between the incident radiation and the crystal plane, λ is the wavelength of the radiation and d is the interplanar distance.

Every plane in the crystal structure can be characterized by the Miller indices h, k, l. The interplanar distance d in the cubic structure can then be calculated using the equation 4.2, where a is lattice parameter of the cubic cell.

$$\frac{1}{d^2} = \frac{a^2}{h^2 + k^2 + l^2} \tag{4.2}$$

4.1.1 Peaks position shift

The change in the lattice parameter leads to change in the interplanar distances, what leads to the different diffraction angle. The peak position shift follows the Bragg equation and is indirectly proportional to the change of the lattice parameter; the increase in lattice parameter leads to decrease in the diffraction angle.

Another reason of the changed peak position has its origin in instrumental error. In the ideal case, positions of the sample, X-rays source and the detector form an imaginary focusing circle. However, when the sample height is changed, diffracted beams are no longer focused on the detector and the maximal intensity is detected at different angle. The difference between the peak position for the standard configuration and peak position in the diffractogram of displaced sample $\Delta 2\theta$ depends on the diffraction angle as:

$$\Delta 2\theta = \frac{2s}{R}\cos\theta \tag{4.3}$$

where s is the sample height displacement and R is the goniometer radius.

Peak position can also be changed as the result of the microscopic strain in the bulk sample, shifted zero position of the goniometer and axial divergence of the beam.

4.1.2 Végard law

In 1921, Végard published a study of the lattice parameter of the system KBr-KCl. In this study he describes, that the experimental lattice parameter followed an equation:

$$a = x_{\mathrm{KBr}} \cdot a_{\mathrm{KBr}} + x_{\mathrm{KCl}} \cdot a_{\mathrm{KCl}} \tag{4.4}$$

where a is the lattice parameter of the resulting crystal, x_{KBr} and x_{KCl} are the molar ratios of KBr and KCl and a_{KBr} and a_{KCl} are the lattice parameters of pure KBr and KCl.

The peak positions shift in the diffractogram allows us to calculate the lattice parameter of the mixed crystal using the equations 4.1, 4.2 and 4.3 and to verify the validity of the Végard law in our samples.

4.1.3 Peaks broadening

The interference function reaches its maximum value in the nodes of reciprocal space and the diffracted intensity is non-zero in very little volume near the each node. In the diffractogram, we observe non-zero diffracted intensity at the angles close to the angle determined by the Bragg equation.

Full width in half maximum (FWHM or $2\,w$) is usually used to describe the peak width. If the peak profile is fitted with Gauss function with the same maximum intensity and area FWHM depends on the radiation wavelength λ and is indirectly proportional to the particles size in the a direction D for cubic crystals. This dependence is described by the Scherrer equation:

$$2\,w \cong \frac{0.94\,\lambda}{D\cos\theta} \tag{4.5}$$

Since the cosine function values decrease with increasing angle, the broadening effect is stronger for the higher diffraction angles.

For non-cubic materials, Scherrer equation can also be used, where D is interpreted as average size of the coherent diffracting domain in the direction perpendicular to the diffracting plane. The use of peak broadening to determine crystallite size is normally limited to cases where the average crystallite size is smaller than 1 μm, otherwise the instrumental broadening caused by divergence of the beam overcomes the broadening effect of small particles.

Another reason for the increased peak width is non-homogeneous deformation of the grain or increased number of dislocations and other lattice defects, which causes variations of the interplanar distances in the sample. Conditions determined by the Bragg equation are fulfilled for different angles and distribution of the interplanar distance results in the distribution of the diffraction angle; the diffraction peak profile broadens.

The analysis of the real measured profiles is complicated by the convolution of the physical and instrumental broadening and partial overlap of peaks corresponding to Kα1 and Kα2 wavelengths of the characteristic spectrum. To determine the instrumental broadening, measurements of standard samples, for example LaB_6 are usually carried out. Since the profile broadening caused by the small particles size results in Lorentz profile peaks and the microdeformations broadening profiles are of Gauss type, profile analysis can help to determine both effects together [34].

4.2 Mossbauer spectroscopy

Mossbauer spectroscopy is the spectroscopy based on resonant emission and absorption of γ-rays.

The method uses Doppler effect to tune energy of the incident radiation at very fine levels. The most studied isotope is ^{57}Fe, with natural abundance of 2.17 % [36].

Fig. 4.1 shows the decay scheme of ^{57}Co that leads to emission of γ-ray with the energy of 14.4 keV. This energy can excite other stable nuclei of the isotope ^{57}Fe leading to nuclear resonant absorption.

Figure 4.1: Nuclear decay scheme of ^{57}Co

showing the transition giving the 14.4 keV γ-ray.

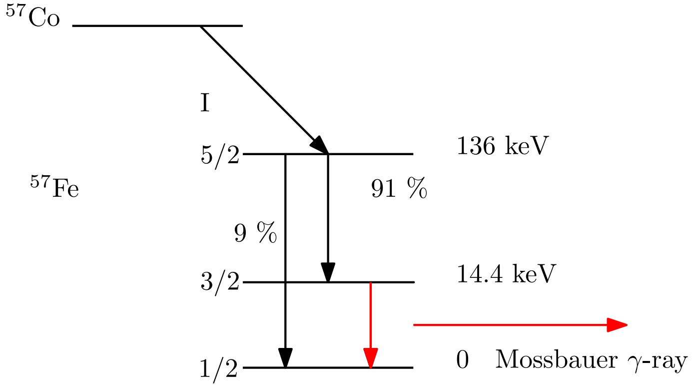

Under normal circumstances, for the free atoms, the recoil energy prevents the absorption. A nucleus in a solid, however, can sometimes emit and absorb γ-rays without a recoil. If the atom is fixed in the lattice and the recoil energy is less than the lowest quantised lattice vibrational energy, the γ-rays can be emitted without any loss of energy. This limits the Mossbauer effect to the isotopes with low-lying excited states.

The energy levels of the nucleus situated in a solid are affected by the environment of the nucleus. If the processes are recoil-free, resonant absorption has very precise energy. This enables to investigate the very small energy changes resulting from the hyperfine interactions between the nucleus and its surrounding electrons and the nucleus can be used as a local probe of its environment.

In the usual transmision experiment, the source nuclei are embedded in a matrix, which provides the necessary solid environment, but gives the simplest possible hyperfine interactions. The γ-rays emitted by the source nuclei pass through the sample, where they are partially absorbed and then they continue to a suitable detector. In order to investigate the energy levels of the ^{57}Fe nuclei in the sample, the emitted radiation energy has to be modified to have the correct energy for resonant absorption.

This is usually accomplished by the oscillatory motion of the source relative to a stationary absorber, what modifies the energy of the γ-rays as a result of the relativistic Doppler effect.

In the typical Mossbauer spectrum, the dependence of the counts on the velocity (in mm/s) is plotted.

In the simplest case, where the emitter and absorber belong to the same isotope with the same cubic environment, the spectrum consists of a single line at zero velocity. Otherwise, the spectrum is split into a doublet or a sextet, that can be characterized by three parameters, isomer shift, quadrupole splitting and hyperfine splitting [37].

4.2.1 Isomer shift δ

The isomer shift, sometimes known also as a chemical shift, is a result of the electric monopole interaction between the nuclear charge distribution and electronic charge density over the finite nuclear volume. For this interaction, the electron charge density in the nucleus has to be non-zero.

The electrostatic attraction for the overlap of a finite nucleus with a constant charge density is stronger when the nucleus is smaller. The effective nuclear radius of the excited ^{57}Fe nucleus is lower than the radius of the ground state. This leads to a difference in energy between the nuclear excited state and ground state in the presence of a constant electron density. The electronic charge density, however, is usually different for the source and absorber nuclei and is dependent on the chemical surrounding of the nucleus. This leads to different energy level correction and hence to the different energy needed for resonant absorption [36].

A possible type of experiment using the isomer shift is determining the valence state of iron. Since 3d electrons partially screen the s electrons, if the number of 3d electrons increases, the screening is stronger and the electron charge density in the nucleus decreases [38]. This causes a more positive isomer shift. For the iron atoms in the valence state VI, the screening is lower than for the source nucleus and the isomer shift is negative.

If there would be no other hyperfine interactions, the resulting spectrum would consist of a single line located at a velocity determined by the isomer shift [37]. Since the lineshape of each nuclear transition is close to a Lorentzian function, the spectral line can be fitted by the Lorentzian peak profile [38].

Table 4.1: Isomer shift ranges (in mm/s) for the iron in different compounds with respect to metal iron [37]

	High spin	Low spin
Fe(VI)	−0.8 to −0.9	
Fe(IV)	−0.2 to +0.2	+0.1 to +0.2
Fe(III)	+0.1 to +0.5	−0.1 to +0.5
Fe(II)	+0.6 to +1.7	−0.2 to +0.5
Fe(0)		−0.2 to −0.1

4.2.2 Quadrupole splitting ΔE_Q

So far, situations where nuclear charge distribution is spherical were discussed. However, nuclei with the nuclear angular momentum quantum number $I > 1/2$ have non-spherical charge distributions which are characterized by a nuclear quadrupole moment. If the nuclear quadrupole moment experiences an asymmetric electric field produced by an non-spherical electronic charge distribution or ligand arrangement, an electric quadrupole interaction occurs. This interaction leads to splitting of the nuclear energy levels.

The ^{57}Fe nucleus in the first excited state has $I = 3/2$. In the presence of an non-spherical electronic charge distribution this state splits into two substates characterized by $m_l = \pm 1/2$ and $m_l = \pm 3/2$. The spectrum in this situation consists of two lines separated by the quadrupole splitting $\Delta \mathrm{E_Q}$. Each line represents the transition form the ground state to one of the substates.

The value of the nuclear quadrupole moment is constant for each nuclide and the quadrupole splitting depends only on the electric field gradient. The gradient contains different contributions.

Partially occupied shells on the Mossbauer atom lead to asymmetric distribution of the valence electrons and hence the Mossbauer spectrum can give us information about electronic populations of various orbitals.

Asymmetric arrangement of the ligands in the lattice also affects the electric field and from the quadrupole splitting the information about the ligand structure can be obtained [37].

4.2.3 Hyperfine splitting $\mathrm{B_{hf}}$

When a nucleus with $I > 0$ is placed in the magnetic field, there is a magnetic dipole interaction between any nuclear magnetic moment and the magnetic field. This interaction splits the degenerated nuclear state into 2I+1 substates, with $m_l = +1/2$ and $m_l = -1/2$ for the ground state and $m_l = +3/2$, $m_l = +1/2$, $m_l = -1/2$ and $m_l = -3/2$ for the excited nuclear state (Zeeman splitting). With the selection rule for the γ-rays absorption $\Delta m_l = 0, \pm 1$, it gives six transitions and the Mossbauer spectrum consists of six lines.

The splitting energy depends on the magnetic field experienced by the nucleus called effective field ($\mathrm{B_{eff}}$). $\mathrm{B_{eff}}$ can have its origin in the hyperfine field $\mathrm{B_{hf}}$ and the external magnetic field $\mathrm{B_{ext}}$ and is given by the vector sum of these contributions as follows:

$$\mathbf{B}_{\mathrm{eff}} = \mathbf{B}_{\mathrm{hf}} + \mathbf{B}_{\mathrm{ext}} \tag{4.6}$$

The hyperfine field arises only from the unpaired spin of the atoms' own electrons and therefore depends on the oxidation and spin state of the atom. The transition probabilities determine the spectral lines intensities, what can give information about the relative magnetic field orientation at the nucleus [37].

4.2.4 Mossbauer spectra of iron(III) oxides

The spectra of the individual iron oxides depend on their magnetic properties and the number of the iron sublattices.

The simplest spectrum is that of hematite. Iron is present in one crystallographic position, which is magnetically split into two sublattices with antiparallely oriented moments. In the ferromagnetic region above Morin temperature the minor spin canting leads to the weak parallel spin component and the ferromagnetic behaviour. In the Mossbauer spectrum of hematite with good crystallinity, we can see a sextet with parameters listed in Tab. 4.2.

Superparamagnetic relaxation causes the magnetic hyperfine splitting to break down at room temperature for particles smaller than 8 nm. The spectrum then consists of a doublet with quadrupole splitting which can increase up to about 1 mm/s with decreasing particle size.

In the samples with particle size lower than 10 nm, the spectrum can be fitted with two Voigt profile doublets of different quadrupole splitting, corresponding to the bulk- and surface-near atoms. The fit using Voigt profile doublet can be explained by the particle size distribution.

Due to superexchange interaction, hematite is antiferromagnetic under the Morin temperature. The spectrum consists of a sextet with parameters listed in Tab. 4.2 at 4.2 K.

Decreased particles size can cause lowering of the Morin temperature. For the particles smaller than 20 nm, the Morin transition is totally suppressed and the particles are present in the weakly ferromagnetic state.

Table 4.2: Mossbauer parameters for the different iron (III) oxides with respect to metal iron [39], [41]

phase	T(K)	δ(mm/s)	ΔE_Q (mm/s)	B_{hf} (T)
α-Fe_2O_3	295	0.37	-0.197	51.75
	4.2	0.49	0.41	54.17
$\beta-Fe_2O_3$	295	0.38	0.76	-
γ-Fe_2O_3	295	0.32	0.02	49.9

Well-crystallized maghemite is magnetically ordered at room temperature. Mossbauer spectrum consists of a sextet with a low quadrupole splitting and hyperfine field characteristic for high-spin Fe(III).

In the applied magnetic field, the ferrimagnetic ordering of the spins of the cations in different sites causes the splitting of the resonances resulting in the different B_{eff}. The relative intensities of the sextets can therefore give us the information about the relative sites occupancies.

In the maghemite samples, the superparamagnetic relaxation has also been described. The hyperfine magnetic splitting vanishes at room temperature, but appears again at temperatures below the blocking temperature. If an external magnetic field is applied, the different sites resonances split up.

Pankhurst and Pollard [40] studied the Mossbauer spectra of the antiferromagnetic powders in external applied magnetic field. This situation is different from that of ferrimagnetic materials because the antiferromagnetic materials have zero magnetisation value. Therefore, there is no alignment of internal magnetic moment parallely or antiparallely to the external magnetic field and the spectrum is not split into two sextets as in the case of ferrimagnetic arrangement. Instead, the peaks of the spectrum show broadening due to distribution of the effective field values.

4.3 Magnetic properties

Magnetic properties of materials are determined by electron configuration of the individual atoms and their mutual interactions. Materials with the filled electron shell show a diamagnetic behaviour. If an external magnetic field is applied, the diamagnetic material acquires a magnetic moment oriented antiparallel to the direction of magnetic field intensity.

In all materials, the closed electron shells contribute diamagnetically. However, if unpaired electrons are present, the overall behaviour is paramagnetic and the magnetic moment of the material is oriented parallel to the magnetic field intensity. When so-called exchange interaction between the unpaired electrons occurs, the material undergoes a magnetic ordering resulting in ferromagnetic, antiferromagnetic or ferrimagnetic state.

The exchange interactions are the result of the electrostatic interactions between the unpaired electrons. In metals, this exchange is usually direct, leading to parallel magnetic moments ordering. In oxides, the distances between the magnetic atoms are too long and the direct exchange is very weak. However, in this materials another exchange mechanism, the superexchange through a diamagnetic atom occurs. Depending on the electronic structure, this exchange can lead to parallel or antiparallel ordering of the magnetic moments.

4.3.1 Magnetisation

Magnetisation M is defined as the sum of the magnetic moments in a volume unit. The change of magnetisation with the magnetic field intensity H, magnetic susceptibility χ, is defined by the equation:

$$\chi = \frac{\partial M}{\partial H}. \tag{4.7}$$

In diamagnetic materials, the dependence of magnetisation on the magnetic field intensity is linear, while in paramagnetic materials the susceptibility is described by the so-called Brillouin function, which approaches a linear dependence at higher temperatures.

Susceptibility of diamagnetic materials is negative. Paramagnetic materials have a small, positive magnetic susceptibility that is dependent on the temperature following the Curie law:

$$\chi = \frac{C}{T}, \tag{4.8}$$

where C is the Curie constant and T is temperature.

The ferromagnetic materials show a parallel ordering of the magnetic moments, leading to spontaneous magnetisation. In these materials, the magnetisation reaches its maximum value at 0 K, and decreases with increasing temperature. At high temperatures, influence of the thermal energy dominates the energy of the exchange interactions and at a critical temperature, Curie temperature T_{C}, the spontaneous magnetisation has zero value.

Above the Curie temperature, the ferromagnetic materials behave as paramagnetic and their susceptibility depends on the temperature following the

Curie-Weiss law:

$$\chi = \frac{C}{T - T_{\mathrm{C}}}. \tag{4.9}$$

In the antiferromagnetic materials, the magnetic moments of the neighbouring cations are oriented antiparallely to form two crystallographically equivalent sublattices with the different magnetic moment orientation. At a critical temperature, usually called Néel temperature, the spontaneous magnetisation disappears and the materials show paramagnetic behaviour following the above mentioned Curie-Weiss law with a negative T_{C} [43].

Parallel ordering of the magnetic moments within individual sublattices, which are coupled antiparallely leads to non-zero spontaneous magnetisation value in the ferrimagnetic materials.

The ferro- and ferrimagnetic materials show a typical hysteresis when inserted into the magnetic field. The dependence of the magnetisation on the magnetic field intensity forms the hysteresis loop, as shown in Fig. 4.2. When the magnetic field higher than the saturation magnetic field is applied, all magnetic moments are aligned in the direction of the applied field; the value of magnetisation at a given temperature is known as the saturation magnetisation M_{S}. If no magnetic field is present, the magnetisation reaches the remanent magnetisation value M_{r} and for the coercive magnetic field with intensity $-H_{\mathrm{c}}$, the magnetisation of the sample is zero.

Figure 4.2: Hysteresis loop of the ferromagnetic material

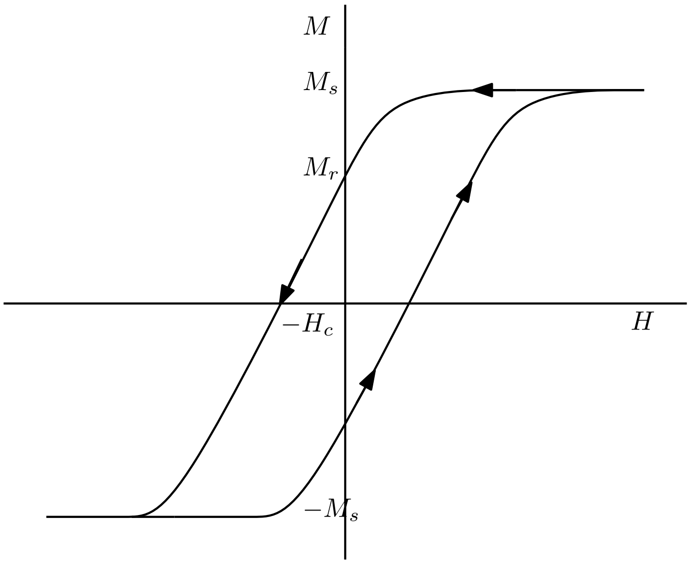

For the materials with a spontaneous magnetisation, formation of the magnetic domains is characteristic. Magnetic domain is an area with the same direction of the magnetic moments, surrounded by the domains with different orientation of the magnetic moment. Inside a domain, the magnetisation is saturated, but the magnetisation directions in different domains are different, what leads to the magnetisation of the whole sample lower than the saturation magnetisation. If the external magnetic field is applied, volume of the domains with the magnetic moment oriented parallel to the magnetic field increases and the volume of the domains with the non-preferred orientation decreases [42].

4.3.2 Superparamagnetism

The number of domains decreases with the decreasing particle size. If a particle size is small enough, the material is present in the form of single-domain particles. Superparamagnetism describes the state of a single-domain-sized grain, when thermal energy is sufficient to overcome the barriers between the two equivalent directions of the magnetic moment orientation. These barriers arise from the magnetocrystallic anisotropy and shape anisotropy and are proportional to the grain volume. When the energy barriers are high compared to the thermal energy, the magnetisation is blocked, the particle is in the blocked state. For the given volume of the particle, above the blocking temperature T_{B} the thermal excitations can result in the reversal of the magnetisation over short time scales and particle is present in the superparamagnetic state. The blocking temperature hence depends on the type of material and the particle shape and size. For a given temperature, the particle is present in the blocked state if the particle volume is higher than a blocking volume V_{B} [44].

4.3.3 Spin glass

As described above, for the existence of the spontaneous magnetisation, ferromagnetic or ferrimagnetic ordering of magnetic moments in the whole crystal is necessary. If a magnetic ion in the structure is substituted by a non-magnetic one, the chain of the moments connected by the exchange interactions is disturbed. If the number of substituted atoms increases, the exchange interactions are weakened, what leads to decreasing of the saturation magnetisation and the Curie temperature. At certain level of dilution, the long-range order is not stable and such system can be described in terms of spin glass, disordered magnetic material with frustrated interactions.

Above the spin glass transition temperature (called glassy temperature), the spin glass exhibits paramagnetic behaviour. When cooled in the presence of applied magnetic field, magnetisation of the spin glass follows the Curie law, until the glassy temperature is reached. Under the glassy temperature, the further cooling leads only to small change in the magnetisation. If the magnetic field is applied after the sample was cooled below the glassy temperature, initially, the magnetisation increases rapidly and then decreases slowly as the temperature increases [45].

5. Preparation

In this chapter preparation and characterization of nanocomposites is described. Samples were prepared using sol-gel method and annealed to different temperatures. Powder diffraction, mossbauer spectroscopy and magnetic measurements were done to characterize prepared composites.

5.1 Sol-gel

Reaction mixture was prepared from different amounts of iron(III) nitrate $Fe(NO_3)_3 \cdot 9H_2O$ and scandium(III) nitrate $Sc(NO_3)_3 \cdot 4H_2O$. For typical preparation 10.6 g of tetraethoxysilane (TEOS), 7 g of methanol, 2.25 g of formamide and 4.5 g of 0.1M nitric acid were added and mixture was stirred for five minutes. Gelation proceeded at 45 °C for 48 hours and gels were dried in nitrogen atmosphere at 45 °C for four days.

Samples were heated to 300 °C in low vacuum for 22 hours, after that temperature increased to 900 °C and samples were annealed at 900 °C at atmospheric pressure for 2 hours. Part of the sample was removed, the rest was then heated to 1000 °C and annealed at that temperature for two hours. Part of the sample was removed again and the rest was heated to 1100 °C and annealed at this temperature for two hours, resulting in three samples of same composition but different annealing temperature, as shown in Tab 5.1.

Part of sample $Fe_{1.4}Sc_{0.6}O_3$ N annealed at 900 °C was heated to 1250 °C, one third of sample $Fe_{1.5}Sc_{0.5}O_3$ annealed at 900 °C was heated to 1250 °C and one third of sample $Fe_{1.5}Sc_{0.5}O_3$ annealed at 900 °C was annealed at 1300 °C for 4 hours.

Table 5.1 shows weighed amounts of iron(III) nitrate and scandium(III) nitrate. Table 5.2 shows temperatures at which different samples were annealed and expected formula of the composites, table 5.3 shows time course of annealing temperature starting at room temperature.

Table 5.1: Weighed amounts of reactants

sample	m($Fe(NO_3)_3 \cdot 9H_2O$) (g)	m ($Sc(NO_3)_3 \cdot 4H_2O$) (g)	c in matrix
$Fe_{1.9}Sc_{0.1}O_3$	1.95	0.077	10:100
$Fe_{1.8}Sc_{0.2}O_3$	1.85	0.154	10:100
$Fe_{1.6}Sc_{0.4}O_3$ N	3.23	0.606	10:100
$Fe_{1.6}Sc_{0.4}O_3$ V	3.23	0.606	20:100
$Fe_{1.5}Sc_{0.5}O_3$	3.03	0.757	20:100
$Fe_{1.4}Sc_{0.6}O_3$ V	2.83	0.91	20:100
$Fe_{1.4}Sc_{0.6}O_3$ N	1.41	0.455	10:100

Table 5.2: Annealing temperatures

expected composition	temperatures (°C)				
$Fe_{1.9}Sc_{0.1}O_3/SiO_2$ 10:100	900	1000	1100		
$Fe_{1.8}Sc_{0.2}O_3/SiO_2$ 10:100	900	1000	1070	1100	
$Fe_{1.6}Sc_{0.4}O_3/SiO_2$ 10:100	900	1000	1100		
$Fe_{1.6}Sc_{0.4}O_3/SiO_2$ 20:100	900	1000	1100		
$Fe_{1.5}Sc_{0.5}O_3/SiO_2$ 20:100	900	1000	1100	1250	1300
$Fe_{1.4}Sc_{0.6}O_3/SiO_2$ 20:100	900	1000	1100		
$Fe_{1.4}Sc_{0.6}O_3/SiO_2$ 10:100	900	1000	1100	1250	

Table 5.3: Dependence of annealing temperature on time

time (min)	1380	120	690	120	30	120	30	120
final temperature (°C)	300	300	900	900	1000	1000	1100	1100

5.2 Leaching of SiO_2 matrix

For typical leaching procedure aproximately 1 g of ground sample was suspended in 30 grams of 50 % sodium hydroxide solution and heated in autoclave for 24 hours at 130 °C. Suspension of nanoparticles was then centrifugated and washed with distilled water until neutral pH. Table 5.4 shows six leached samples, their names differ from non-leached samples in the letter L.

Table 5.4: List of leached samples

$Fe_{1.9}Sc_{0.1}O_3$ 900 °C L	$Fe_{1.8}Sc_{0.2}O_3$ 900 °C L	$Fe_{1.6}Sc_{0.4}O_3$ 1100 °C L
$Fe_{1.5}Sc_{0.5}O_3$ 9000 °C L	$Fe_{1.4}Sc_{0.6}O_3$ 1000 °C V L	$Fe_{1.4}Sc_{0.6}O_3$ 1100 °C V L

5.3 Characterization

5.3.1 Powder X-ray Diffraction

Bragg-Brentano geometry diffractometer PANalytical X'pert PRO equipped with copper tube (Kα_1 0.1541 nm, Kα_2 0.1544 nm), secondary monochromator and PIXcel detector was used for sample measurements.

Small amount of ground sample was placed on the top of glass kyvette. Data was obtained at room temperature, 2θ ranging from 10 ° to 80 ° with step 0.05 ° 2θ. Peak positions were calibrated using LaB_6 as standard.

5.3.2 Mossbauer spectroscopy

Measurements were carried out at three different conditions; at room temperature, at low temperatures and at 4.2 K under magnetic field of 6 T.

Room temperature measurements

RT measurements were performed using spectrometer with ^{57}Co source of γ-rays; isomer shift was calibrated using α-Fe foil as standard. For typical measurement 70 to 100 mg of non-leached powdered sample was inserted into mossbauer kyvette, data was being collected for 3 days at room temperature.

Low temperature measurements

This measurements were carried out using spectrometer Wissel with ^{57}Co as a source of gama rays and scintillating detector ND-220-M (NaI:Tl^{+}) in transmission arrangement. Low temperatures down to 4.2 K were reached using liquid He cooling. Isomer shift was calibrated using α-Fe foil as standard, fitting procedure was done using NORMOS program. Measurement at low temperature (4 K) in applied magnetic field 6 T was done in perpendicular arrangement.

5.3.3 Electron microscopy

TEM was carried out using the JEOL 200CX device operating at 200 kV.

HRTEM images were captured with the JEM 2010 UHR device equipped with the Gatan Imaging Filter (GIF) and the 794 slow scan CCD. The samples for the TEM and HRTEM analysis were prepared by drying the dispersion of nanoparticles on the coated copper grid.

5.3.4 Magnetic measurements

The zero-field-cooled (ZFC) and field-cooled (FC) magnetizations (applied field of 10 mT) and magnetization isotherms at different temperatures were measured on the Quantum Design MPMS7XL device (SQUID). The temperature dependences of the a.c. susceptibility were recorded in zero external magnetic field at frequencies: 0.1, 1, 10, 102 and 103 Hz with the amplitude of the a.c. magnetic field of 0.3 mT. For the typical measurement the prepared sample was put into the capsule and fixed with a piece of polystyrene.

6. Results and discussion

In this chapter the results of PXRD, Mossbauer spectroscopy, electron microscopy and magnetic measurements for the samples with different substitution will be described.

6.1 Sample $Fe_{1.9}Sc_{0.1}O_3$

The sample of the composition $Fe_{1.9}Sc_{0.1}O_3/SiO_2$ was prepared in matrix in the molar concentration ratio of 10:100. Sample was annealed at three different temperatures, 900 °C, 1000 °C and 1100 °C. Results of PXRD measured at room temperature are shown in Fig. 6.1.

Figure 6.1: Powder X-ray diffractograms of samples annealed at 900, 1000 and 1100 °C measured at room temperature

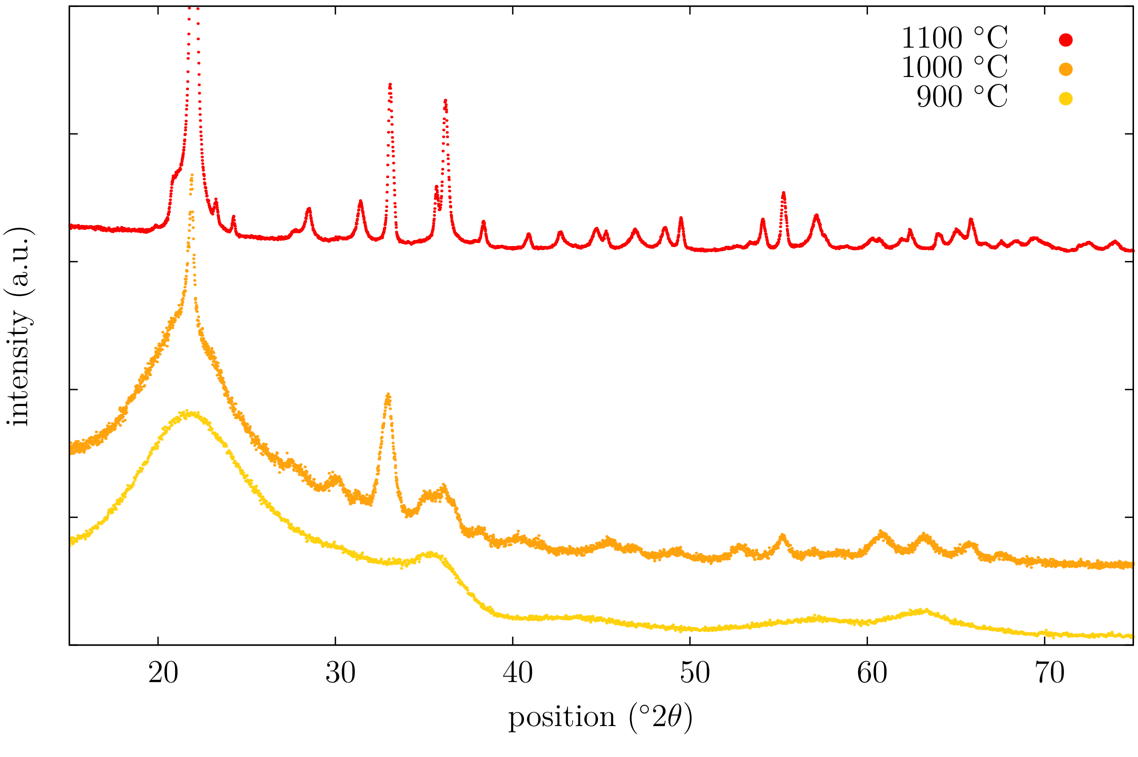

6.1.1 Sample annealed at 900 °C

PXRD results given in Fig. 6.1 consist of five wide peaks. Broad band at 22 °2θ belongs to amorphous phases. Comparison of peaks at 35.8, 44.2, 57.2 and 63.2 °2θ with PDF database shows match with the spinel structure of Fe_2O_3 and does not show presence of any other Fe_2O_3 phases. Particles size estimated using Scherrer equation is approximately 3 nm.

Mossbauer spectrum measured at 4.2 K without applied magnetic field in Fig. 6.2 shows sextet and low intensity doublet in the center. The signal in the center of the spectrum does not represent the sample properties and comes from metallic iron present in aluminium foil used as sample holder. The fit shows two overlapping sextets; one of iron in octahedral and the second of iron in tetrahedral sites. In zero field measurements, these two sextets are overlapped, and it is not possible to determine the amount of iron in octahedral and tetrahedral positions. For this reason, the in-field measurements was carried out.

In spectrum measured in applied magnetic field in Fig. 6.2, we can see separation of these two sextets. From this fact we can conclude that the sample is ferrimagnetic. The isomer shift values 0.38 and 0.48 mm/s are typical for those of atoms in tetrahedral and octahedral sites, respectively[39]. Since maghemite is the only ferrimagnetic Fe_2O_3 phase with iron in two sublattices, we can conclude that at this conditions, maghemite γ-Fe_2O_3 is formed.

Figure 6.2: Mossbauer spectra of sample annealed at 900 °C measured in applied field 0 T and 6 T at 4.2 K

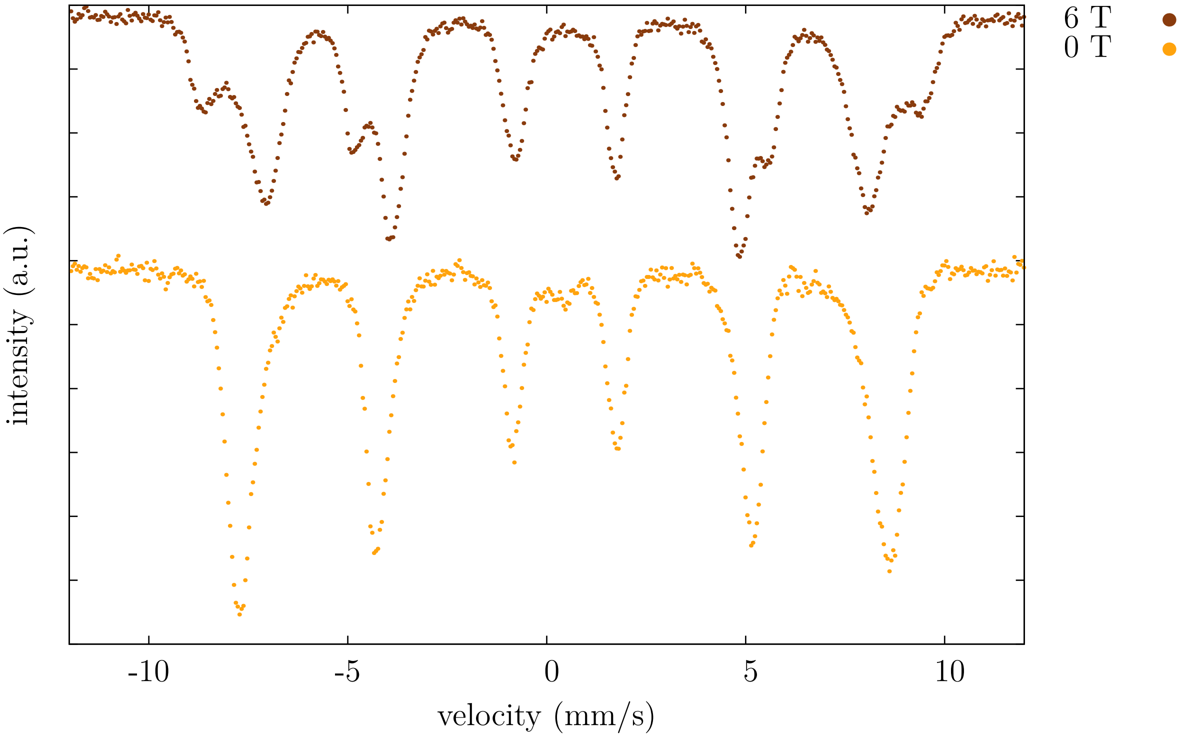

Table 6.1: Subspectra of Mossbauer spectrum of sample $Fe_{1.9}Sc_{0.1}O_3$ annealed at 900 °C measured at 4.2 K without (top) and with applied magnetic field (bottom)

subspectrum	δ (mm/s)	ΔE_Q (mm/s)	B_{hf} (T)	relative area (%)
sextet 1	0.43	-0.022	49.6	30
sextet 2	0.46	0.023	51.9	70
sextet 1	0.38	0.002	55.7	30
sextet 2	0.48	0.011	47.1	70

6.1.2 Sample annealed at 1000 °C

PXRD results in Fig. 6.1 show the broad band of amorphous phases at 22 °2θ and peaks of β- and $\varepsilon-\mathrm{Fe}_2\mathrm{O}_3$. We can observe a partial crystallisation of the matrix manifested by sharp peak at 22 °2θ, which belongs to cristobalite. The diffraction peaks of the sample annealed at 1000 °C are narrower compared to the peaks of the sample annealed at 900 °C due to the crystal growth that took place during the annealing. There are no signals suggesting presence of hematite.

Table 6.2: Diffraction peak assignment of the PXRD of the sample $\mathrm{Fe}_{1.9}\mathrm{Sc}_{0.1}\mathrm{O}_3$ annealed at 1000 °C

peak position (°2θ)	27.6	30.2	33.0	36.4	38.2	40.3	41.5	45.5
corresponding phase	ε	ε	ε and β	ε	β	ε	ε	β
peak position (°2θ)	47.0	49.3	52.9	55.2	60.7	63.1	65.9	
corresponding phase	cristobalite	β	ε	β	ε	ε	β	

Fit of Mossbauer spectrum in Fig. 6.3 shows 3 sextets of ε-phase and doublet of β-phase; the fit parameters are listed in Tab. 6.3. Isomer shift 0.38 mm/s and quadrupole splitting 0.76 are parameters typicall for β-$\mathrm{Fe}_2\mathrm{O}_3$, molar content of β-phase is 26 %. Relative intensities for ε-phase sextets are not listed, the sextet intensities ratio is approximately 1:1:1 and the molar content of ε-phase is 74 %.

Figure 6.3: Mossbauer spectra of samples with two annealing temperatures measured at room temperature

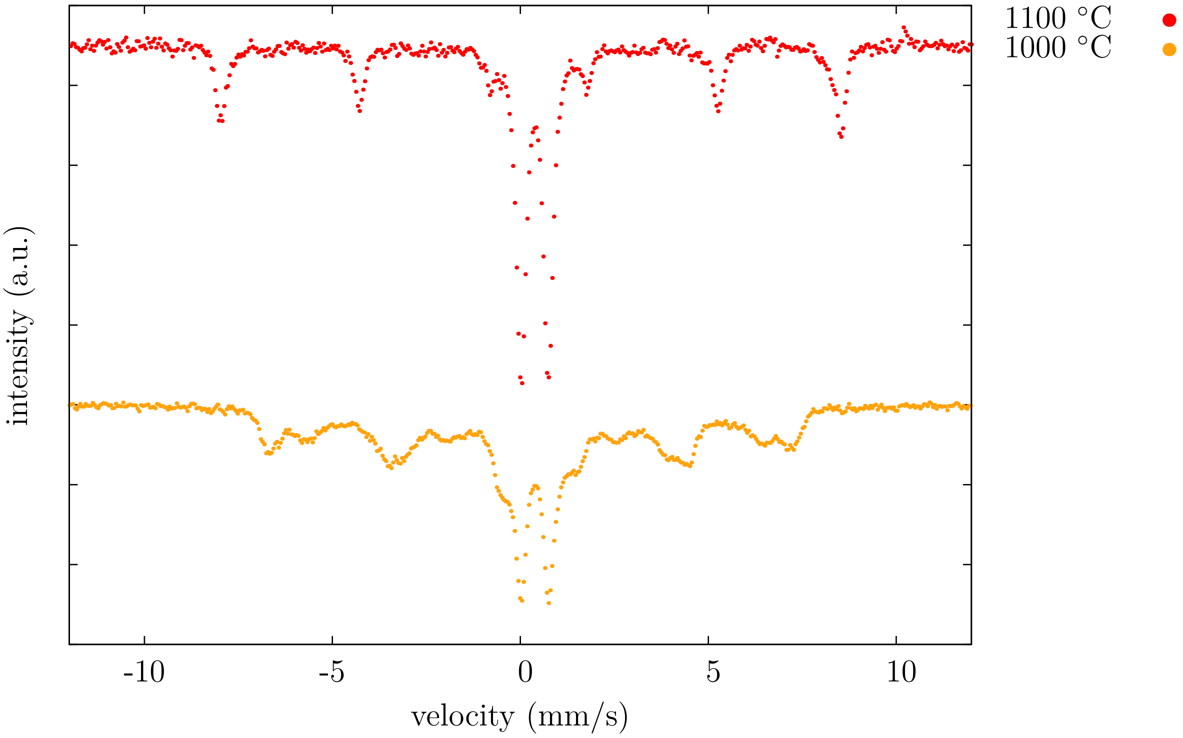

In the dependence of magnetisation on temperature shown in Fig. 6.4 the presence of ε-$\mathrm{Fe}_2\mathrm{O}_3$ can be seen, represented by the magnetic transition occurring at

Table 6.3: Subspectra of Mossbauer spectrum of the sample $Fe_{1.9}Sc_{0.1}O_3$ annealed at 1000 °C

subspectrum	δ (mm/s)	ΔE_Q (mm/s)	B_{hf} (T)	relative area (%)
doublet	0.38	0.76	-	26 %
sextet 1	0.39	-0.26	42.9	-
sextet 2	0.40	-0.08	37.4	-
sextet 3	0.24	-0.14	25.0	-

110-130 K. At low temperatures, the sample behaves as spin glass. This behaviour can be explained by the presence of a phase with diluted exchange interactions.

Figure 6.4: ZFC and FC magnetisation curves of the sample $Fe_{1.9}Sc_{0.1}O_3$ annealed at 1000 °C measured at 0.1 T

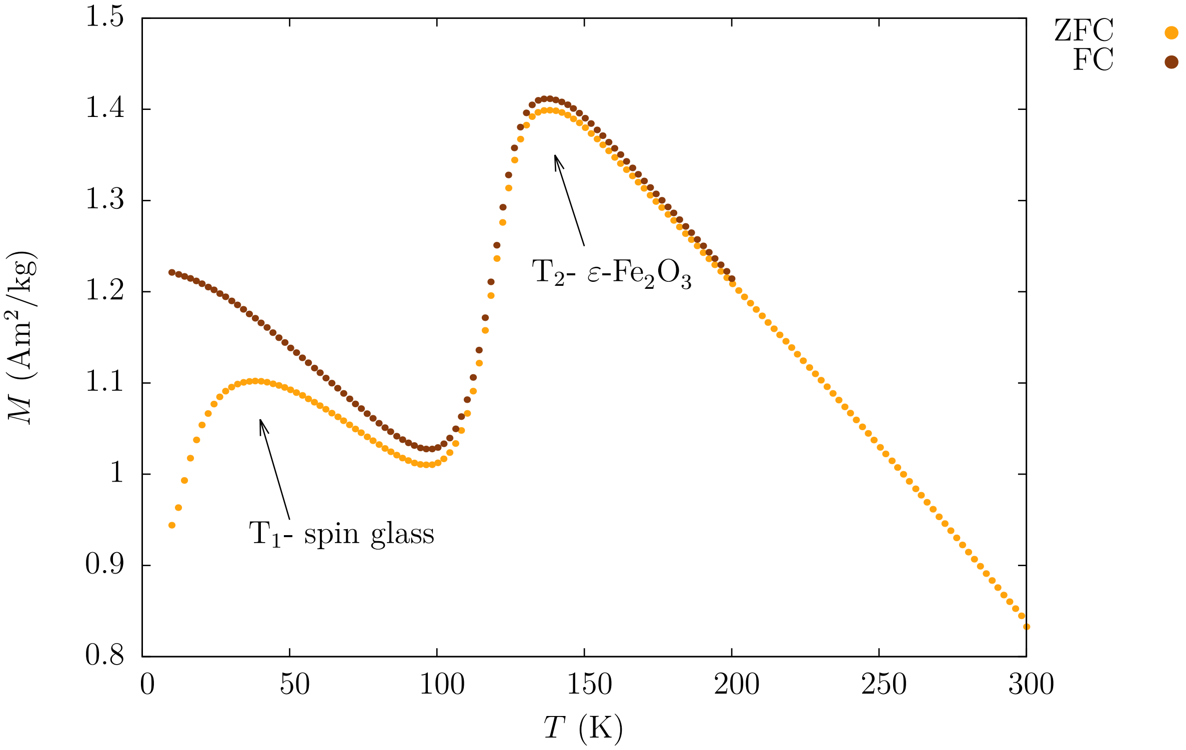

6.1.3 Sample annealed at 1100 °C

In PXRD results given in Fig. 6.1, there are no peaks at 61.3 and 63.6 °2θ corresponding to peaks of ε-phase. All intensive peaks of both α- and β-phase can be seen. Since the amorphous band at 22 ° 2θ is still present, crystallization of the matrix is not completed at this temperature in this sample. Approximate particles size at this temperature is 60 nm.

This is in agreement with the Mossbauer spectrum in Fig. 6.3; doublet of β-phase and sextet of hematite are observed and the molar ratio of the phases is 64 : 36. Since only one sextet is present, the sample contains no ε-phase.

Table 6.4: Diffraction peak assignemet of the PXRD of the sample $Fe_{1.9}Sc_{0.1}O_3$ annealed at 1100 °C; C is short for cristobalite

peak position (°2θ)	22.0	23.3	24.2	28.5	31.4	33.0	35.7
corresponding phase	C	β	α	C	C	$\alpha+\beta$	α
peak position (°2θ)	36.2	38.3	40.9	42.7	44.7	45.2	46.9
corresponding phase	C	β+C	α	C	C	β+C	C
peak position (°2θ)	48.5	49.5	54.1	55.2	62.4	65.8	
corresponding phase	C	α	α	β	α	β	

Table 6.5: Subspectra of Mossbauer spectrum of the sample $Fe_{1.9}Sc_{0.1}O_3$ annealed at 1100 °C

subspectrum	δ (mm/s)	ΔE_Q (mm/s)	B_{hf} (T)	relative area (%)
doublet	0.38	0.72	-	64
sextet	0.38	-0.21	51.2	36

6.2 Sample $Fe_{1.8}Sc_{0.2}O_3$

The sample was prepared in molar ratio in matrix 10:100. Powder X-ray diffractograms and Mossbauer spectra of samples annealed at 900 °C, 1000 °C and 1100 °C measured at room temperature are shown in Fig. 6.5 and Fig. 6.6.

6.2.1 Sample annealed at 900 °C

Results of powder X-ray diffraction are similar to those of sample $Fe_{1.9}Sc_{0.1}O_3$ annealed at 900 °C; amorphous band at 22 °2θ is present, what means that the silica matrix is present only in amorphous state. Peak positions at 35.7, 44.0, 57.3 and 62.4 °2θ are typical for spinel phase of Fe_2O_3. Since no peaks of α-, β- or ε-phase are present after annealing at 900 °C, the most probable phase formed is maghemite. As for the sample with lower substitution and the same annealing temperature, the particles size is approximately 3 nm.

Mossbauer spectrum measured at room temperature shows only one doublet. Doublet, that can be attributed to β-phase is narrow, typical width values are between 0.35 and 0.45 mm/s. This values would mean that the phase has good crystallinity. The doublet in the spectrum is wider and the parameters don't correspond to β-phase. After annealing of the sample at 900 °C, small particles of maghemite in superparamagnetic state are probably formed.

Table 6.6: Subspectra of Mossbauer spectrum of sample $Fe_{1.8}Sc_{0.2}O_3$ annealed at 900 °C

subspectrum	δ (mm/s)	ΔE_Q (mm/s)	width (mm/s)	relative area (%)
doublet	0.34	0.89	0.72	100

Measurements at low temperatures can give us information about composition of the samples, that are superparamagnetic at room temperature. Results of Mossbauer spectroscopy measured at 4.2 K given in Fig. 6.7 show one sextet, brown in the spectrum, with signal of iron from aluminium foil in the middle.

Figure 6.5: Powder X-ray diffractograms of samples annealed at 900 °C, 1000 °C and 1100 °C measured at room temperature

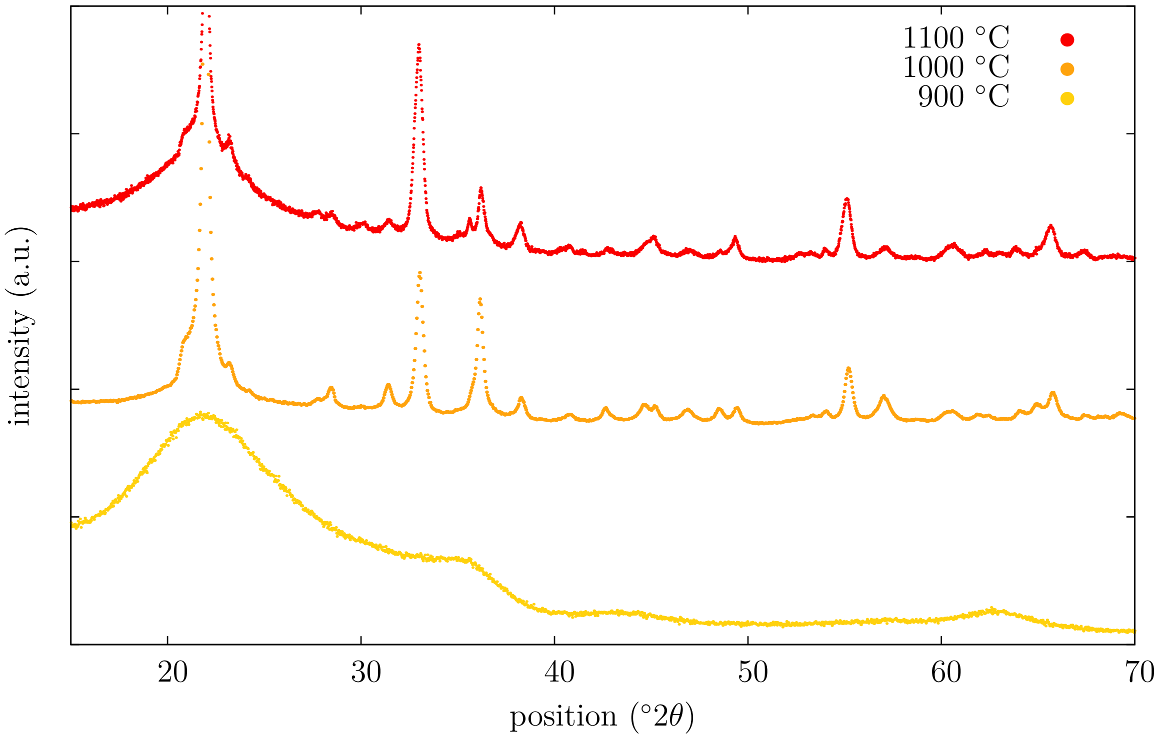

Spectrum is split into two sextets in applied magnetic field of 6 T, what is typical behaviour of ferrimagnetic compounds with iron atoms in nonequivalent tetrahedral and octahedral sites. As in the sample $Fe_{1.9}Sc_{0.1}O_3$ annealed at 900 °C, the only phase present is γ-Fe_2O_3.

Table 6.7: Subspectra of Mossbauer spectrum of sample $Fe_{1.8}Sc_{0.2}O_3$ annealed at 900 °C measured at 4.2 K without (top) and with applied magnetic field 6 T (bottom)

subspectrum	δ (mm/s)	ΔE_Q (mm/s)	B_{hf} (T)	relative area (%)
sextet 1	0.39	-0.02	49.5	49
sextet 2	0.48	0.02	51.6	36
sextet 1	0.36	-0.05	56.0	33
sextet 2	0.48	0.01	46.7	67

Figure 6.6: Mossbauer spectra of samples annealed at 900 °C, 1000 °C, 1070 °C and 1100 °C measured at room temperature

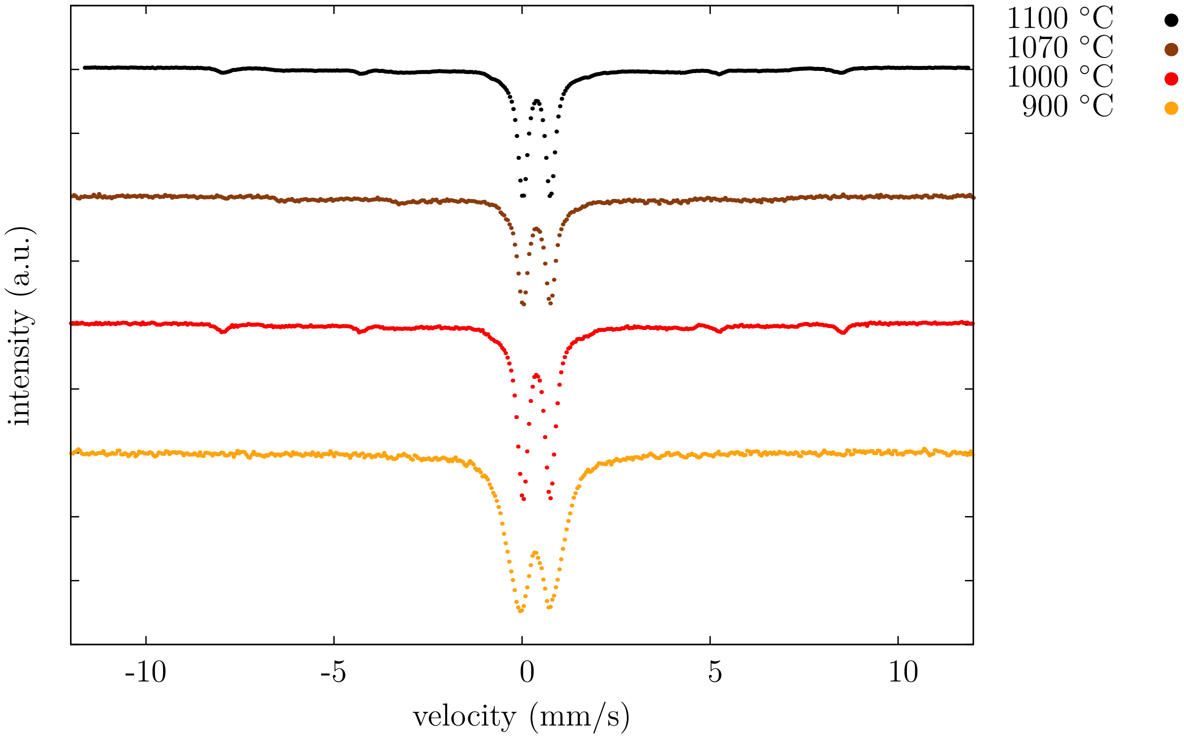

Figure 6.7: Mossbauer spectra of sample annealed at 900 °C measured in applied field 0 T and 6 T at 4.2 K

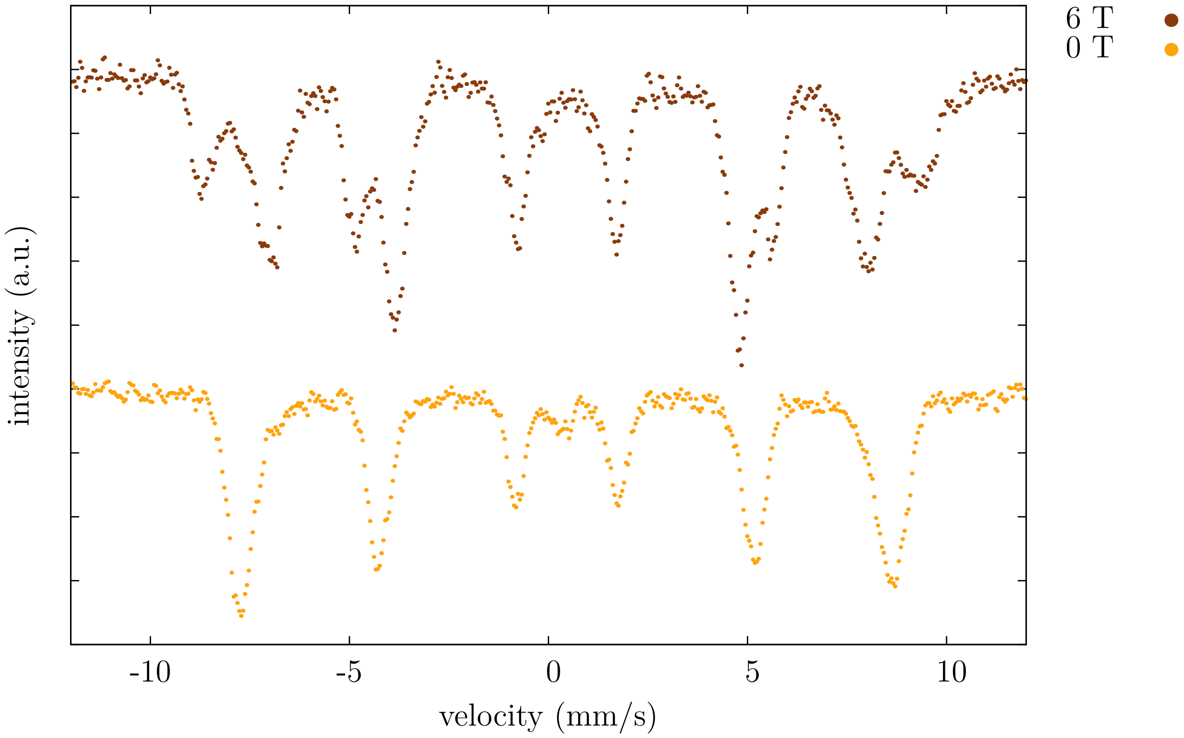

6.2.2 Sample annealed at 1000 °C

PXRD results are given in Fig. 6.5. As shown in the Tab. 6.8, peaks of β-Fe_2O_3 can be seen next to the broad amorphous band. Presence of α-phase is possible because all the strong diffractions except for the peak found at 24.3 °2θ are in overlap with either β-phase or cristobalite peaks. Particle size calculated using Scherrer equation is 25 nm.

Table 6.8: Peak attribution of the PXRD of the sample $Fe_{1.8}Sc_{0.2}O_3$ measured at 1000 °C; C is short for cristobalite

peak position (°2θ)	22.0	23.2	24.3	28.4	31.4	33.0	38.3	40.8	42.6	44.6
corresponding phase	C	β	α	C	C	β	β	β	C	C
peak position (°2θ)	45.2	46.9	48.5	49.4	54.0	55.2	57.0	62.5	65.7	67.4
corresponding phase	β	C	C	β	C	β	C	α	β	β

Mossbauer spectrum given in the Fig. 6.6 shows doublet of β-phase and small sextet of hematite. Molar ratio of Fe_2O_3 phases calculated from area is 92:8.

Table 6.9: Subspectra of Mossbauer spectrum of sample $Fe_{1.8}Sc_{0.2}O_3$ annealed at 1000 °C measured at room temperature

subspectrum	δ (mm/s)	ΔE_Q (mm/s)	B_{hf} (T)	relative area (%)
doublet	0.38	0.74	-	92
sextet	0.38	-0.21	51.1	8

Mossbauer spectra in Fig. 6.8 measured at decreasing temperature show magnetic transition of β-phase from superparamagnetic to blocked state that occurs at approximately 80 K. Quality of spectra at low temperatures is not as high as for measurement at room temperature, that is why the subspectrum of hematite is lost in the noise.

Table 6.10: Subspectra of Mossbauer spectrum of sample $Fe_{1.8}Sc_{0.2}O_3$ annealed at 1000 °C measured at 4.2 K without applied magnetic field

subspectrum	δ (mm/s)	ΔE_Q (mm/s)	B_{hf} (T)	relative area (%)
sextet 1	0.48	0.20	48.6	9
sextet 2	0.43	0.15	53.6	91

Mossbauer spectrum in Fig. 6.9 measured at 4.2 K shows low intensity doublet of iron in aluminium foil and two sextets. Parameters of the sextet 1 given in the Tab. 6.10 confirm the presence of hematite in the sample in less than 10 molar %. Spectrum measured at 4.2 K and 6 T shows broad peaks. These broad peaks are characteristic for antiferromagnetic compound measured in the applied magnetic field [40].

Figure 6.8: Mossbauer spectra of sample annealed at 1000 °C, measured at low temperature

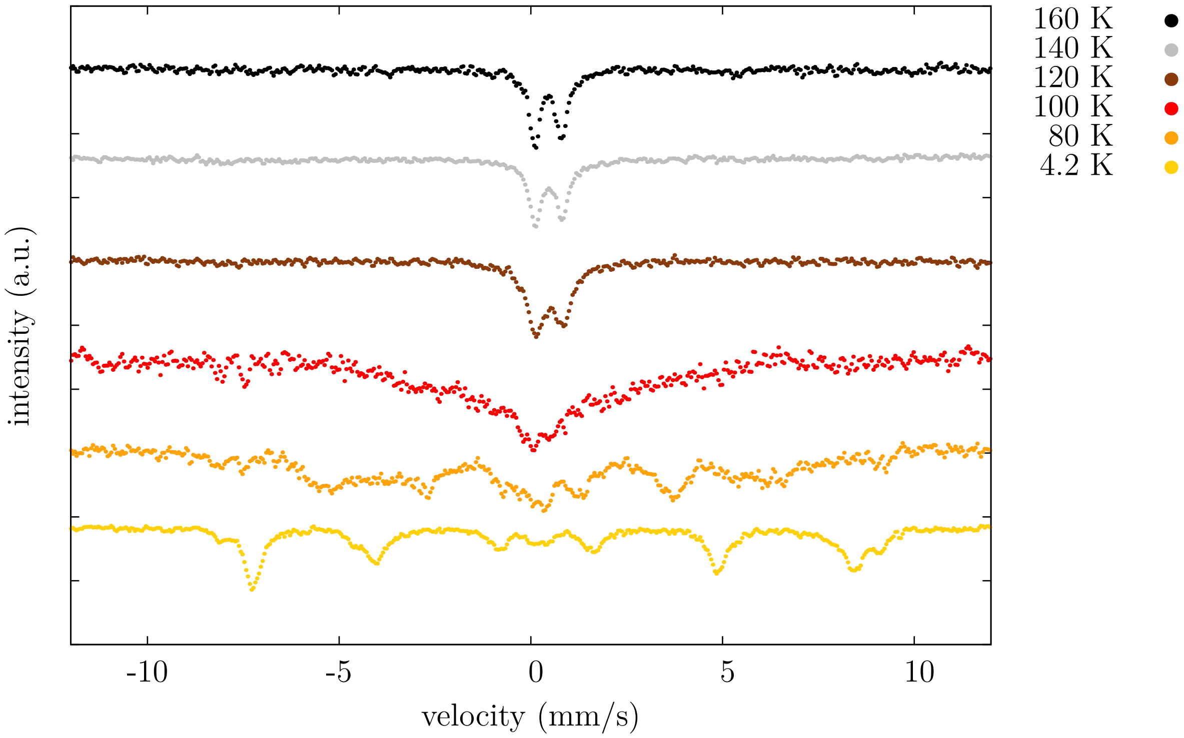

Figure 6.9: Mossbauer spectra of sample annealed at 1000 °C measured in applied field 0 T and 6 T at 4.2 K

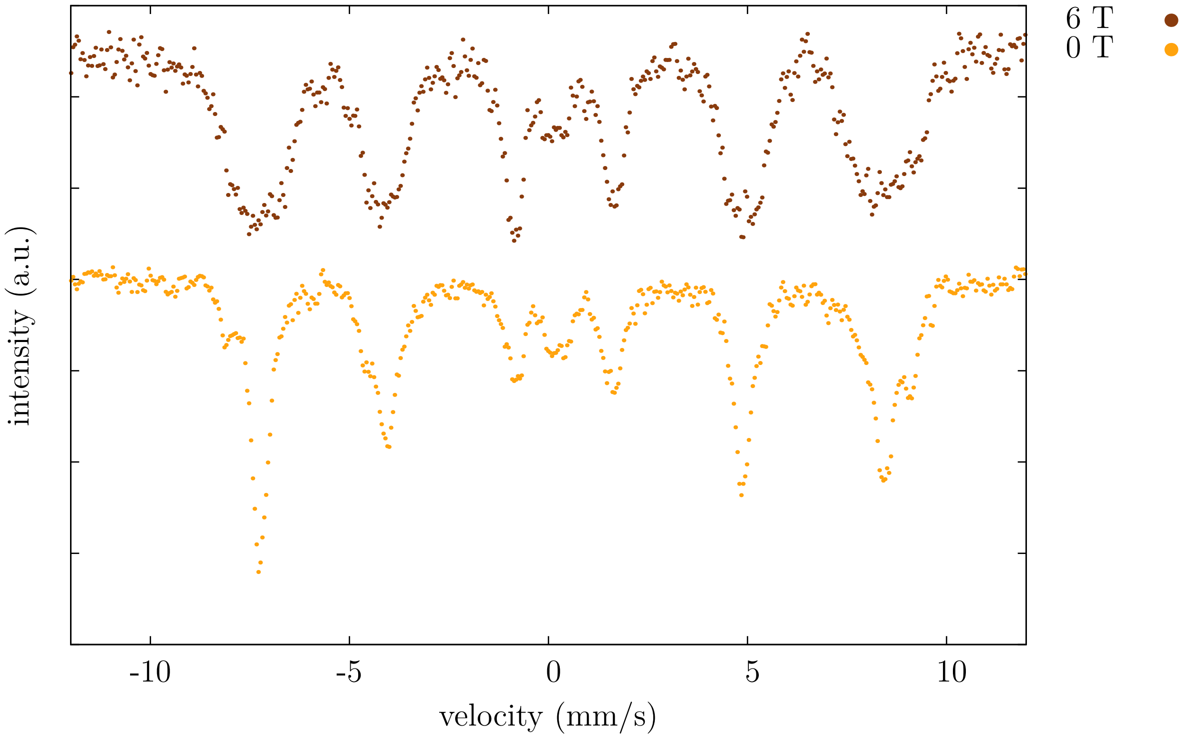

6.2.3 Sample annealed at 1100 °C

PXRD results in Fig. 6.5 show that sample contains mostly β-Fe_2O_3. Broad band of amorphous phases located at 22 °2θ is still present and next to the peaks of cristobalite and β-Fe_2O_3 peaks of low intensity of other phases can be seen. The peak positions match the peaks of maghemite, but the most intensive maghemite peak is overlapped with cristobalite peak. Since maghemite is the less stable phase of the iron(III) oxides at high temperatures, its presence in the sample after annealing at 1100 °C would be surprising. Another explanation is the presence of tridymite as the result of incomplete matrix crystalisation.

Particles size calculated using Scherrer equation is 24 nm.

Table 6.11: Peak assignment of the PXRD of the sample $Fe_{1.8}Sc_{0.2}O_3$ measured at 1100 °C; C is short for cristobalite

peak position (°2θ)	22.0	23.2	27.7	28.4	31.4	32.9	35.6
corresponding phase	C	C	β	γ?	C	β	β
peak position (°2θ)	36.2	38.2	40.8	42.7	45.0	46.9	49.3
corresponding phase	C	β	γ	C	β	C	β
peak position (°2θ)	55.0	57.2	60.5	62.3	65.6	67.3	
corresponding phase	C	β	C	C	β	β	

Mossbauer spectrum in Fig. 6.6 consists of a doublet that can be fitted with Lorentzian doublet of the β-phase and of hematite sextet of small intensity. There are no signals of γ- or ε-Fe_2O_3 to support the results of PXRD and the peaks in the diffractogram can be attributed to tridymite.

Table 6.12: Subspectra of Mossbauer spectrum of sample $Fe_{1.8}Sc_{0.2}O_3$ annealed at 1100 °C measured at room temperature

subspectrum	δ (mm/s)	ΔE_Q (mm/s)	B_{hf} (T)	relative area (%)
doublet	0.38	0.75	-	92
sextet	0.38	-0.23	50.8	8

6.3 Sample $Fe_{1.6}Sc_{0.4}O_3$ N

The sample was prepared in molar ratio in matrix 10:100. It was annealed at four temperatures, 900, 1000, 1050 and 1100 °C. This sample was studied with the electron microscopy that was performed on the samples annealed at 1000 and 1100 °C.

Figure 6.10: Powder X-ray diffractograms of samples annealed at 900 °C, 1000 °C and 1100 °C measured at room temperature

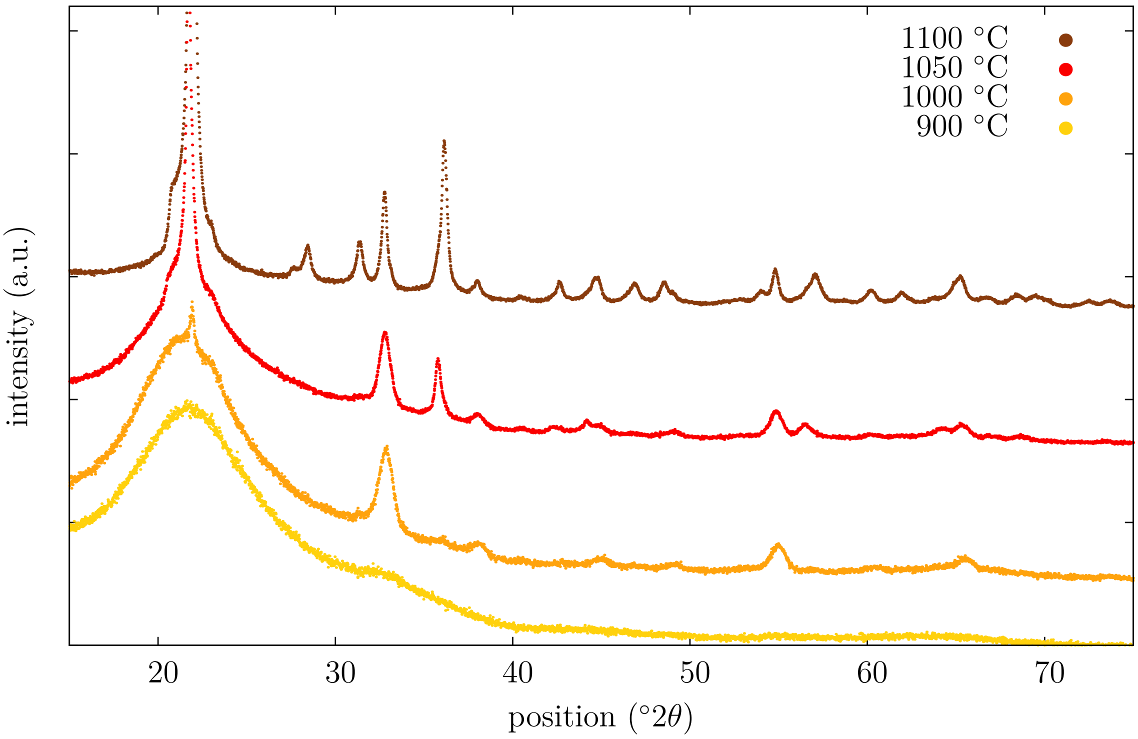

6.3.1 Sample annealed at 900 °C

Powder diffractogram of sample annealed at 900 °C given in Fig. 6.10 is different from those of samples $Fe_{1.9}Sc_{0.1}O_3$ and $Fe_{1.8}Sc_{0.2}O_3$ annealed at 900 °C, as shown in Fig. 6.12. That means that the phase formed at this temperature is no longer maghemite. In the diffractogram, only intensive broad band of amorphous SiO_2 and wide peaks of β-phase can be seen. Particles size calculated using Scherer equation is 5 nm.

Mossbauer spectrum measured at room temperature given in Fig. 6.11 shows that the sample contains particles in superparamagnetic state and particles of β-phase. Spectrum can be fitted with two Lorentzian doublets, one of them with parameters of β-phase. Subspectra parameters are listed in Tab. 6.13.

The width value 0.50 mm/s for the first doublet corresponding to β-phase is close to the values between 0.35 and 0.45 mm/s, that correspond to the β-phase with good crystallinity. This confirms the small particles size determined from PXRD.

Figure 6.11: Mossbauer spectra of samples annealed at different temperatures measured at room temperature

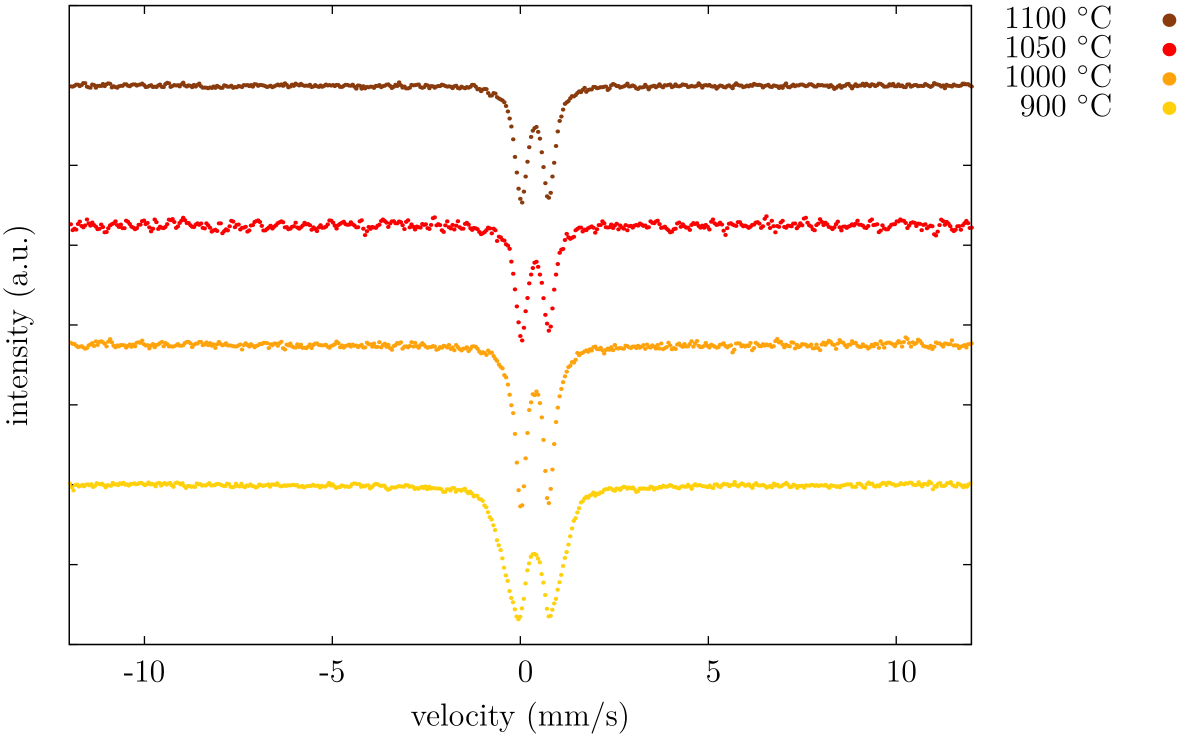

Figure 6.12: PXRD of samples with different substitution and same annealing temperature 900 °C

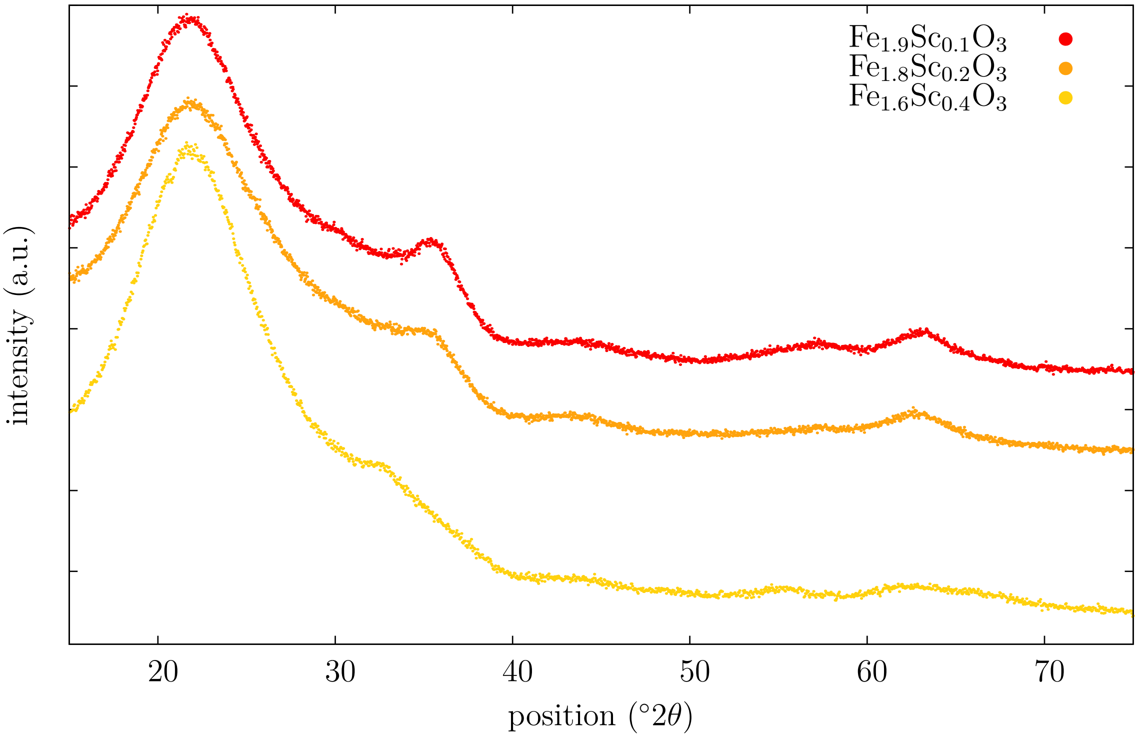

Table 6.13: Subspectra of Mossbauer spectrum of sample $Fe_{1.6}Sc_{0.4}O_3$ N annealed at 900 °C measured at room temperature

subspectrum	δ (mm/s)	ΔE_Q (mm/s)	width (mm/s)	relative area (%)
doublet 1	0.35	0.81	0.50	67
doublet 2	0.35	1.5	0.56	33

6.3.2 Sample annealed at 1000 °C

Powder diffractogram of this sample given in Fig. 6.10 shows a broad band of amorphous SiO_2 and two peaks of cristobalite. Matrix is almost fully amorphous, cristobalite peaks have low intensity. β-phase peaks are the only peaks present and particles size calculated from Scherer equation is 10 nm.

Table 6.14: Diffraction peak assignment of the PXRD of the sample $Fe_{1.6}Sc_{0.4}O_3$ N annealed at 1000 °C

peak position (°2θ)	21.9	32.8	36.0	38.0	45.1	49.1	54.9	65.3
corresponding phase	C	β	C	β	β	β	β	β

Figure 6.13: TEM picture of the sample $Fe_{1.6}Sc_{0.4}O_3$ N annealed at 1000 °C

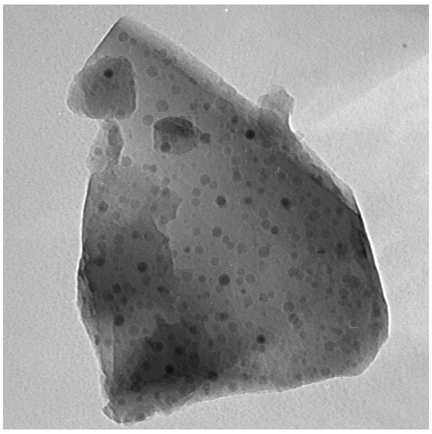

Mossbauer spectrum in Fig. 6.11 shows only a narrow doublet with isomer shift 0.38 mm/s and quadrupole splitting 0.76 mm/s; parameters typical for β-phase with good crystallinity.

Fig. 6.13 shows TEM picture of the sample annealed at 1000 °C, where we can see the nanoparticles of β-Fe_2O_3 embedded in the matrix. Magnification is 50 000 x and the particle size estimated from the electron microscopy is 8 ± 2 nm, what is in agreement with the results of the PXRD.

6.3.3 Sample annealed at 1050 °C

Powder diffractogram of the sample in Fig. 6.10 shows peaks of cristobalite and peaks of β-phase. There are also peaks of other phases that we were not able to identify. Particles size calculated from Scherer equation is 14 nm. Peak positions with attribution to the corresponding phase are listed in Tab. 6.15

Table 6.15: Peak assignment of the PXRD of the sample $Fe_{1.6}Sc_{0.4}O_3$ annealed at 1050 °C

peak position (°2θ)	32.8	35.8	38.0	42.2	44.1	49.0	54.8	56.5	64.1	65.3
corresponding phase	β	C	β	C	?	β	β	C	α	β

In Mossbauer spectrum in Fig. 6.11 doublet of β-phase with isomer shift 0.36 mm/s and quadrupole splitting 0.73 mm/s can be seen and the spectrum does not show presence of any other Fe_2O_3 phases.

6.3.4 Sample annealed at 1100 °C

This series of samples is the most suitable for the illustration of the crystallization of the matrix. In the Fig. 6.10, the narrowing of the amorphous band with the increasing annealing temperature can be seen. As the broad band narrows, the intensities of the peaks of cristobalite increase and finally become greater than the intensity of the peaks of β-phase in the sample annealed at 1100 °C.

Peak positions are listed in the Tab. 6.16. No peaks of hematite can be seen, the sample contains only β-phase in the matrix. Particles size is approximately 27 nm.

Table 6.16: Peak assignment of the PXRD of the sample $Fe_{1.6}Sc_{0.4}O_3$ annealed at 1100 °C

peak position (°2θ)	21.9	28.4	31.3	32.8	36.0	37.9	42.6	44.8
corresponding phase	C	C	C	β	C	β	C	β
peak position (°2θ)	46.9	48.5	54.0	54.8	57.0	60.2	61.9	65.3
corresponding phase	C	C	C	β	C	C	C	β+C

Mossbauer spectrum in Fig. 6.11 shows a doublet with isomer shift 0.38 mm/s and quadrupole splitting 0.74 mm/s. This parameters are typical for β-phase. No sextet of hematite can be seen, what is in agreement with results of PXRD. When scandium substitution is 20 molar %, pure β-phase stable at 1100 °C containing less than 1 % of other iron oxides phases can be prepared.

In the Fig. 6.14 the nanoparticles with the particle size 10 to 30 nm embedded in the silica matrix can be seen. In the picture on the left, we can see a single 20nm particle. In contrast to the amorphous matrix, a set of crystal planes can be seen.

Figure 6.14: TEM pictures of sample $Fe_{1.6}Sc_{0.4}O_3$ N annealed at 1100 °C

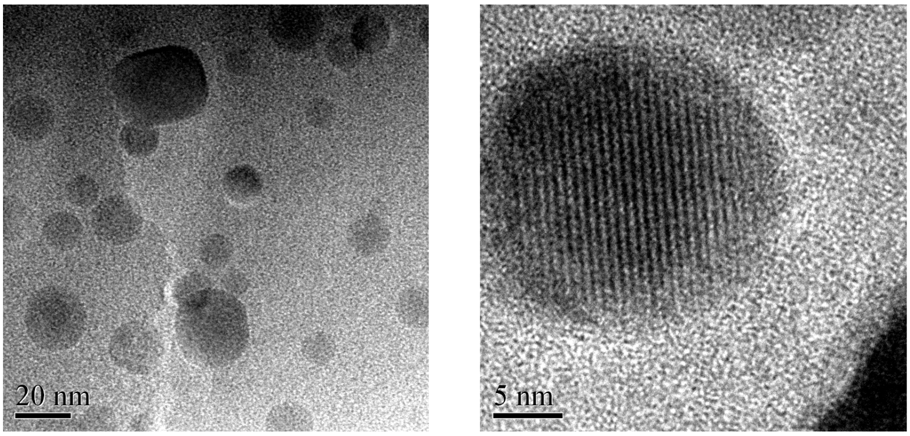

6.4 Sample $Fe_{1.6}Sc_{0.4}O_3$ V

The sample was prepared with the same scandium substitution as the sample described in the previous section, but the molar concentration of the active compound in the matrix was higher (20:100). This experiment was carried out in order to find whether the iron oxide concentration has an influence on the phase formation in the silica matrix.

Figure 6.15: Powder X-ray diffractograms of the samples annealed at 900 °C, 1000 °C and 1100 °C measured at room temperature

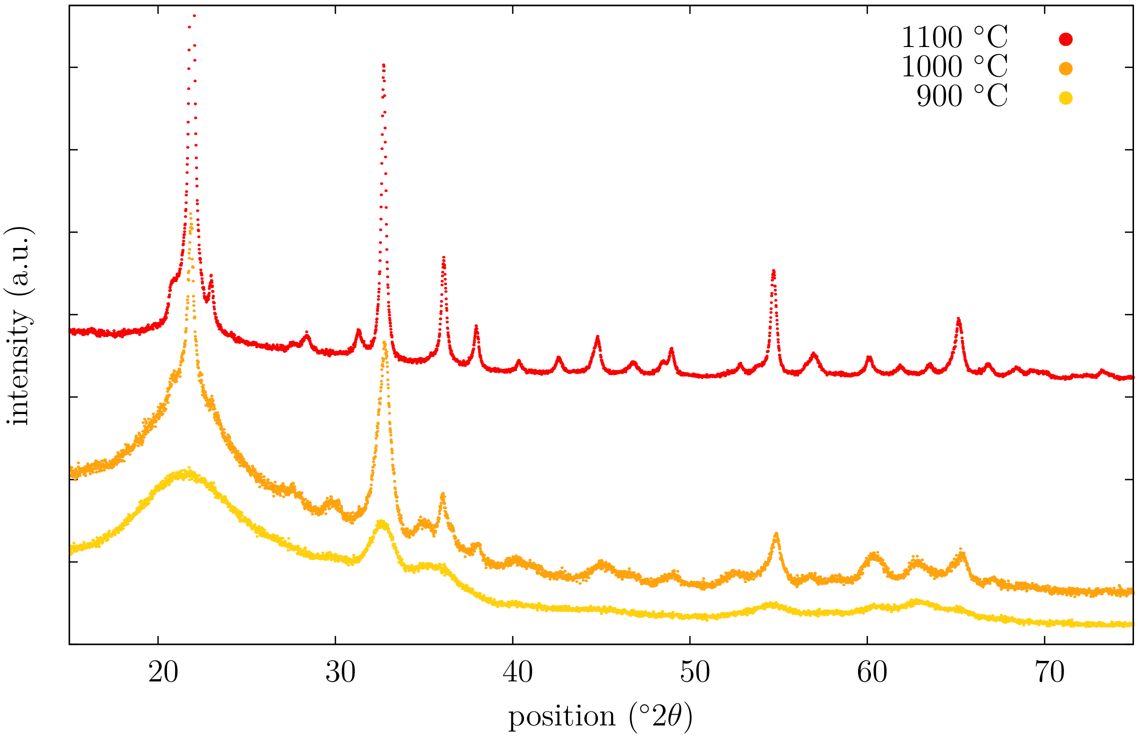

Figure 6.16: Mossbauer spectra of the sample $Fe_{1.6}Sc_{0.4}O_3$ V annealed at different temperatures, measured at room temperature

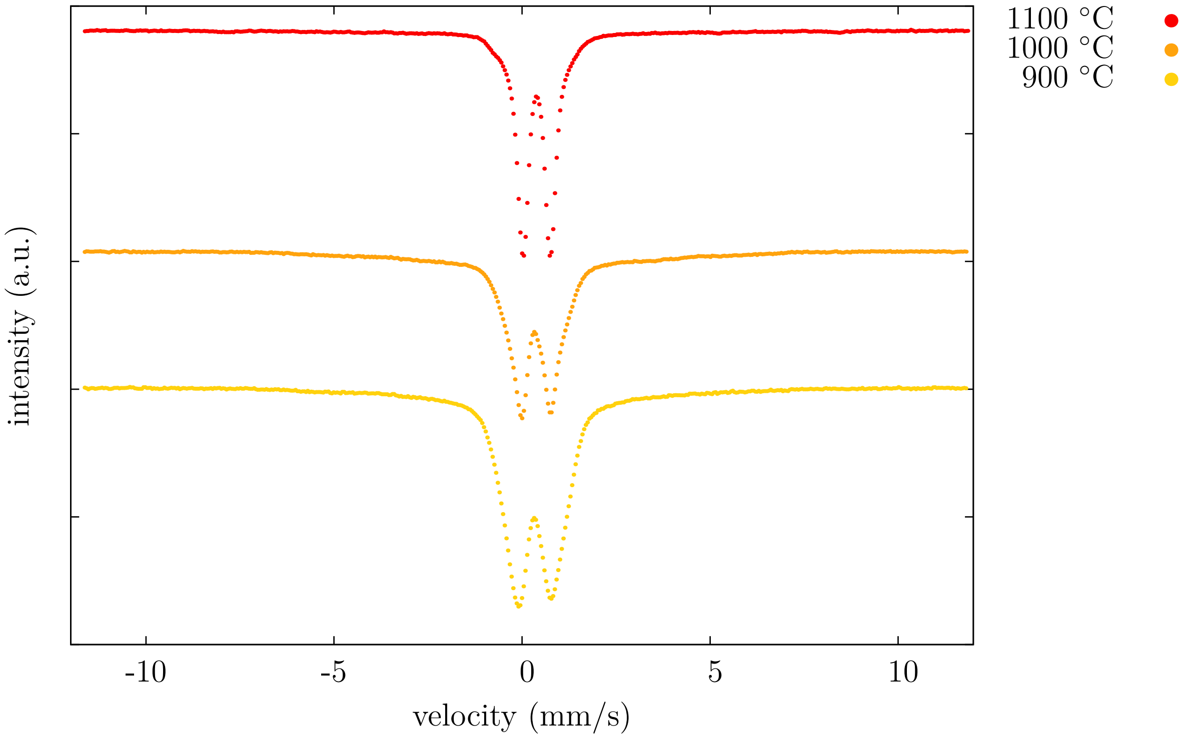

6.4.1 Sample annealed at 900 °C

In powder X-ray diffraction shown in Fig. 6.15, the broad band of amorphous SiO_2 and peaks of β-Fe_2O_3 located at 32.7, 54.4, 60.8 and 65.1 °2θ can be found. Next to that, there are also peaks that can be attributed to maghemite located at 35.7, 63.0 and 74.5 °2θ. Particle size calculated from PXRD using Scherer's equation is approximately 5 nm.

Mossbauer spectrum in Fig. 6.16 consists of a wide doublet which can be fittes with two wide overlapping doublets. Their parameters are listed in Tab. 6.17.

Table 6.17: Subspectra of Mossbauer spectrum of sample $Fe_{1.6}Sc_{0.4}O_3$ V annealed at 900 °C measured at room temperature

subspectrum	δ (mm/s)	ΔE_Q (mm/s)	width (mm/s)	relative area (%)
doublet 1	0.33	0.75	0.52	39
doublet 2	0.35	1.3	0.81	61

The broadening of the Mossbauer lines occurs due to the small particle size, which causes the distribution of the quadrupole splitting parameter. In the sample the small particles of β-phase in the superparamagnetic state are present.

6.4.2 Sample annealed at 1000 °C

Peaks positions of PXRD results given in Fig. 6.15 with corresponding phases are listed in Tab. 6.18. Next to the peaks of cristobalite and β-Fe_2O_3, four peaks of other phases can be seen. Those peaks probable belong to ε-Fe_2O_3, but the presence of maghemite is not excluded. Estimated particles size is 15 nm.

Table 6.18: Peak assignment of the PXRD of the sample $Fe_{1.6}Sc_{0.4}O_3$ V annealed at 1000 °C

peak position (°2θ)	21.9	27.7	29.7	32.8	34.8	36.0	38.1	40.1
corresponding phase	C	ε	ε	β	ε	C	β	β
peak position (°2θ)	44.9	49.2	52.5	54.9	60.3	62.6	65.3	
corresponding phase	β+C	β	β+C	β	β+C	ε	β	

Mossbauer spectrum shown in Fig. 6.16 can be fitted with a rather wide doublet of β-phase, another doublet probably of some other iron oxide phase in the superparamagnetic state and a wide singlet. No sextets of ε or α phase are present, subspectra are listed in Tab. 6.19.

Table 6.19: Subspectra of Mossbauer spectrum of the sample $Fe_{1.6}Sc_{0.4}O_3$ V annealed at 1000 °C measured at room temperature

subspectrum	δ (mm/s)	ΔE_Q (mm/s)	width (mm/s)	relative area (%)
doublet 1	0.36	0.77	0.44	73
doublet 2	0.37	1.5	0.59	27
singlet 1	0.18	-	10.8	-

In the Fig. 6.17, the dependence of magnetisation on temperature is shown. At low temperatures, the sample behaves as spin glass, what can be result of diluted exchange interactions in the structure with magnetic cations substituted by scandium. At temperature of 150 to 300 K, the magnetic transition of the ε-phase occurs. Compared to the sample $Fe_{1.9}Sc_{0.1}O_3$, the transition can be observed at higher temperatures due to the increased amount of scandium in the structure.

Although the Mossbauer spectroscopy and X-ray diffraction show the presence of β-phase, the sample does not show the antiferromagnetic behaviour. This can be explained by the fact that magnetisation of the antiferromagnetic β-phase has much lower values than magnetisation of ε-Fe_2O_3 and the changes of magnetisation due to the presence of antiferromagnetic compound are too small.

6.4.3 Sample annealed at 1100 °C

In the PXRD results in Fig. 6.15 next to the peaks of β-phase and cristobalite no other peaks can be seen. Particles size is approximately 39 nm.

Table 6.20: Peak assignment of the PXRD of the sample $Fe_{1.6}Sc_{0.4}O_3$ V annealed at 1100 °C

peak position (°2θ)	21.9	23.0	28.4	31.3	32.7	36.0	38.0	40.3	42.6	44.8
corresponding phase	C	β	C	C	β	C	β	β	C	β
peak position (°2θ)	46.8	48.4	48.9	52.9	54.7	56.9	60.1	61.9	63.4	65.1
corresponding phase	C	C	β	β	β	C	C	β	β	C

Figure 6.17: ZFC and FC magnetisation curves of the sample $Fe_{1.6}Sc_{0.4}O_3$ annealed at 1000 °C measured at 0.1 T

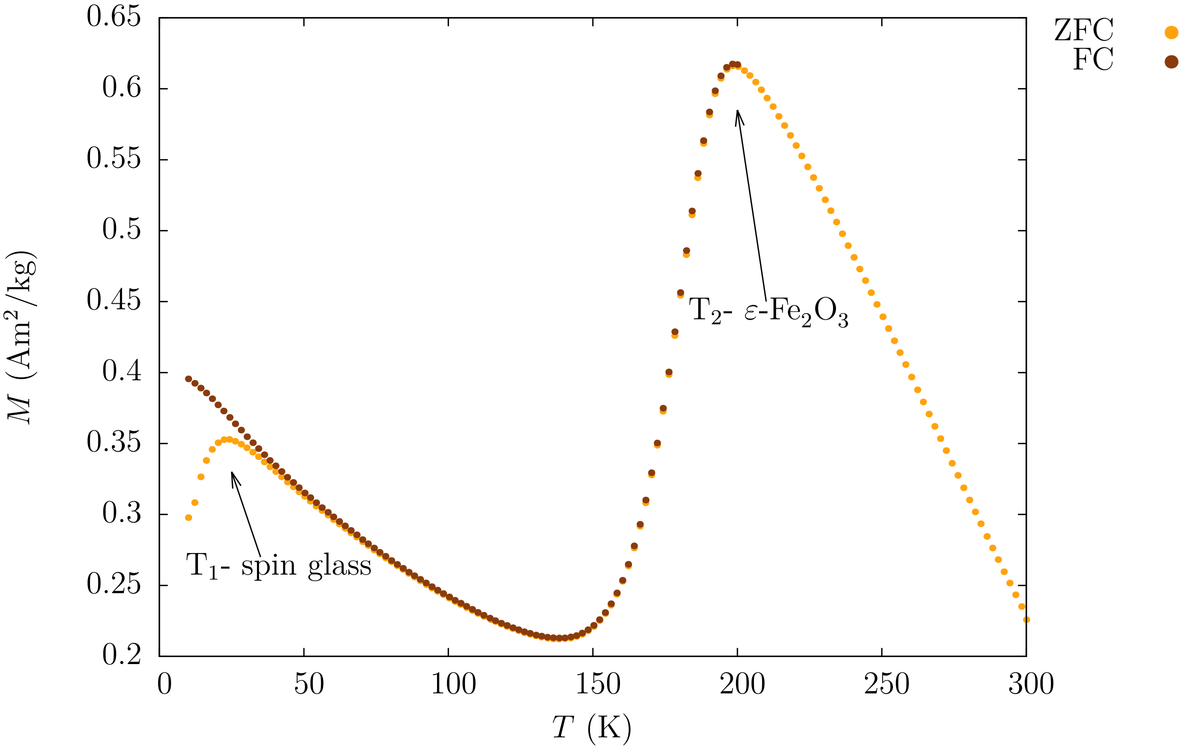

Mossbauer spectrum shown in Fig. 6.16 consists of a narrow doublet of β-Fe_2O_3 with isomer shift 0.38 mm/s and quadrupole splitting 0.75 mm/s. This parameters are the same as for the sample with lower substitution. Next to this narrow doublet, we can observe a shoulder that represents an admixture that we are not able to determine.

Mossbauer spectrum in Fig. 6.18 illustrates the magnetic transition of the β-phase from superparamagnetic to blocked state. Measurement at 100 K doesn't show any sextets next to the doublet of β-phase. At 80 K, magnetic ordering occurs and sextet of β-phase appears.

In spectrum measured at 4.2 K given in Fig. 6.19 a signal of iron from aluminium foil, sextet of β-phase and another sextet with molar ratio 77:23 can be seen. The subspectra are listed in Tab. 6.21.

Table 6.21: Subspectra of Mossbauer spectrum of the sample $Fe_{1.6}Sc_{0.4}O_3$ V annealed at 1100 °C measured at 4.2 K without applied magnetic field

subspectrum	δ (mm/s)	ΔE_Q (mm/s)	B_{hf} (T)	relative area (%)
sextet 1	0.50	0.10	47.5	77
sextet 2	0.49	0.74	49.9	23

Figure 6.18: Mossbauer spectra of the leached sample annealed at 1100 °C measured at low temperatures

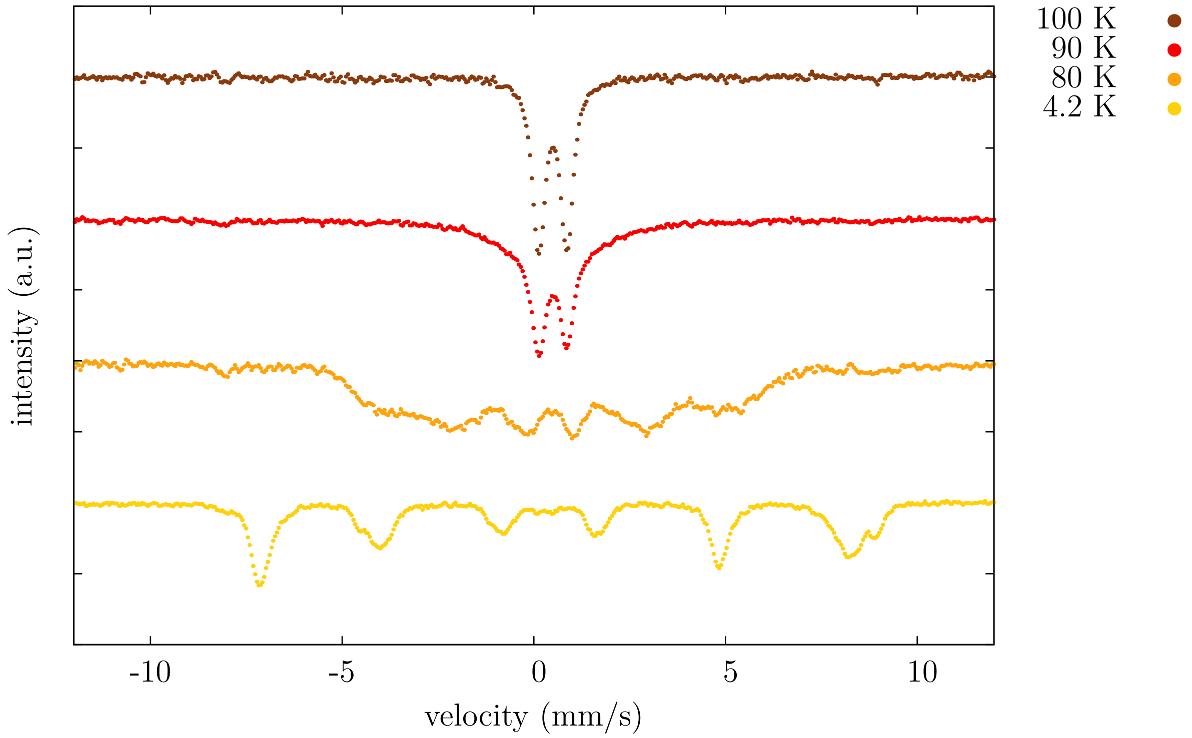

Figure 6.19: Mossbauer spectra of sample after leaching annealed at 1100 °C measured at 4.2 K in applied field 0 T and 6 T

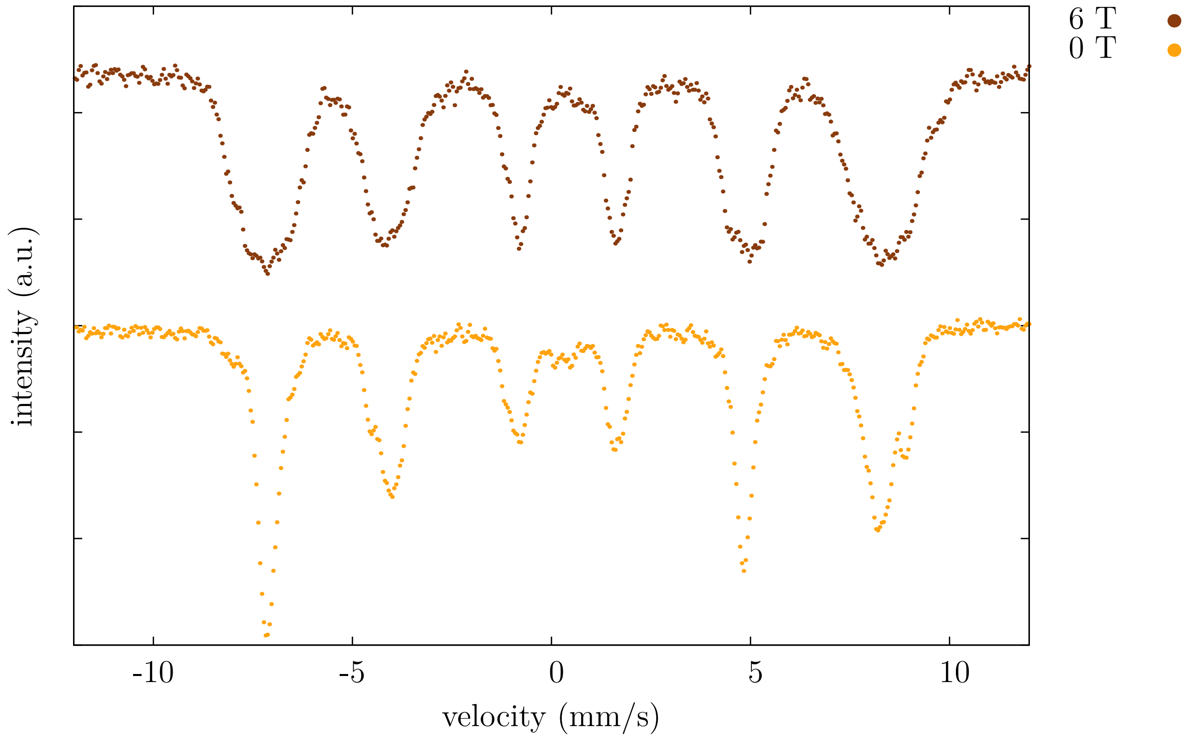

6.5 Sample $Fe_{1.5}Sc_{0.5}O_3$

Sample was prepared in molar ratio 20:100. It was annealed at five temperatures, 900, 1000, 1100, 1250 and 1300 °C. The sample annealed at 900 °C was leached.

Figure 6.20: PXRD of samples annealed at different temperatures measured at room temperature

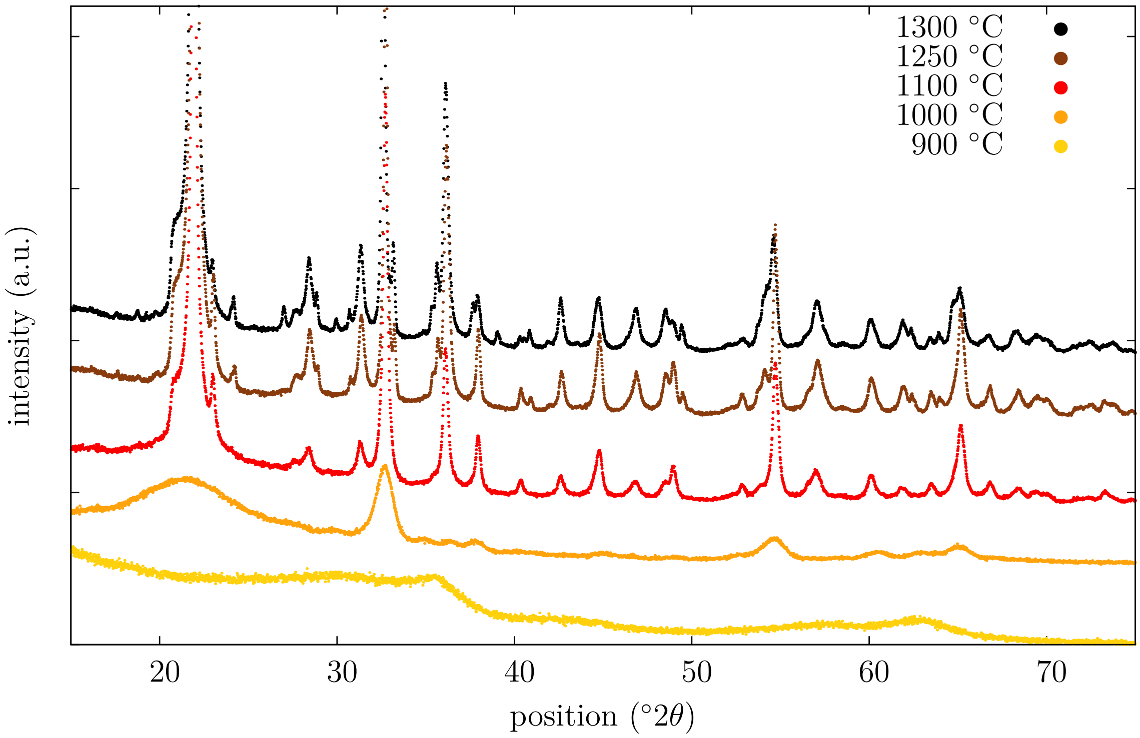

6.5.1 Sample annealed at 900 °C

In the PXRD results shown in Fig. 6.20 no peaks of β-Fe_2O_3 can be found. Probably, the only phase present is maghemite with particles size approximately 4 nm. Sample was leached, that's why no broad band of amorphous matrix can be seen.

Mossbauer spectrum in Fig. 6.21 doesn't show any sextets belonging to hematite, it shows only a doublet. The spectrum can be fitted with two doublets with parameters listed in Tab. 6.22. At room temperature, particles are probably in superparamagnetic state and only measurement at lower temperature would confirm presence of γ-phase in the sample.

Table 6.22: Subspectra of Mossbauer spectrum of sample $Fe_{1.5}Sc_{0.5}O_3$ annealed at 900 °C measured at room temperature

subspectrum	δ (mm/s)	ΔE_Q (mm/s)	width (mm/s)	relative area (%)
doublet 1	0.33	0.84	0.56	46
doublet 2	0.35	1.5	0.76	54

Figure 6.21: Mossbauer spectra of samples annealed at different temperatures measured at room temperature

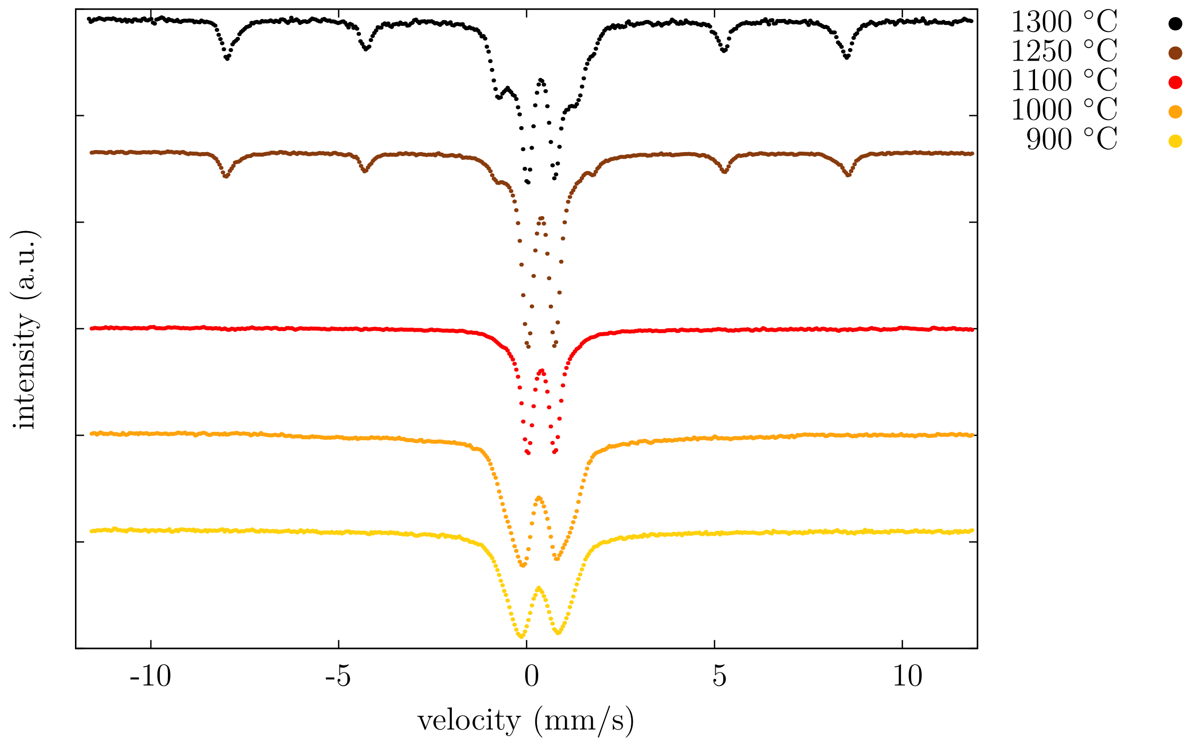

6.5.2 Sample annealed at 1000 °C

In this sample, at annealing temperature 1000 °C no crystallisation of matrix occured. In the PXRD results given in Fig. 6.20 there is only broad band of amorphous phases at 22 °2θ in the diffractogram. No peaks of hematite can be found, but next to the 7 peaks of β-phase two peaks at 35 and 36.5 °2θ of small intensity are present. This two peaks probably belong to ε-Fe_2O_3, other ε-phase peaks would be in overlap with the wide peaks of β-phase. β-phase particles size is approximately 10 nm.

Table 6.23: Peak assignment of the PXRD of the sample $Fe_{1.5}Sc_{0.5}O_3$ annealed at 1000 °C

peak position (°2θ)	29.9	32.6	34.8	36.5	37.8	45.0	54.5	60.5	63.1	64.9
corresponding phase	ε	β	β	ε	β	β	β	β	β	β

Mossbauer spectrum given in Fig. 6.20 shows the same problem with interpretation as the sample discussed in the previous section. Spectrum can be fitted with two doublets, their parameters are listed in Tab. 6.24. Compared to the sample annealed at 900 °C, the doublet 1 has the same parameters. The peaks become narrower and isomer shift approaches the typical value of isomer shift of β-phase 0.38 mm/s with the increasing heat treatment temperature. The parameters of the other doublet have changed only slightly and probably belong to particles in superparamagnetic state. Since no sextets of hematite or ε-phase can be seen, it is not possible to identify the present phases from the Mossbauer spectrum unambiguously.

Table 6.24: Subspectra of Mossbauer spectrum of sample $Fe_{1.5}Sc_{0.5}O_3$ annealed at 1000 °C measured at room temperature

subspectrum	δ (mm/s)	ΔE_Q (mm/s)	width (mm/s)	relative area (%)
doublet 1	0.35	0.82	0.47	40
doublet 2	0.37	1.5	0.75	60

6.5.3 Sample annealed at 1100 °C

Powder X-ray diffractogram of the sample annealed at 1100 °C is given in Fig. 6.20, peaks positions are listed in Tab. 6.25. In the sample only β-phase nanoparticles with particle size 39 nm are present.

Table 6.25: Peak assignment of the PXRD of the sample $Fe_{1.5}Sc_{0.5}O_3$ annealed at 1100 °C

peak position (°2θ)	21.9	23.0	27.6	31.3	32.7	36.0	37.9
corresponding phase	C	β	C	C	β	C	β
peak position (°2θ)	40.4	42.6	44.8	46. 9	48.4	49.0	52.8
corresponding phase	β	C	β	C	C	β	β
peak position (°2θ)	54.6	57.0	60.0	61.8	63.5	65.2	
corresponding phase	β	C	C	β	β	β	

In the Mossbauer spectra measured at room temperature given in Fig. 6.21 we can follow the further evolution of the spectra.

Doublet of β-phase is fully developed, with parameters corresponding to the values of β-Fe_2O_3. Peaks are narrow, what corresponds with the results of PXRD of this sample showing particles size of 39 nm. This particle size is large enough to show Mossbauer parameters without distribution. However the doublet 2 becomes even wider, its quadrupole splitting is higher and its area decreases. This doublet probably represents the particles in superparamagnetic state.

Table 6.26: Subspectra of Mossbauer spectrum of sample $Fe_{1.5}Sc_{0.5}O_3$ annealed at 1100 °C measured at room temperature

subspectrum	δ (mm/s)	ΔE_Q (mm/s)	width (mm/s)	relative area (%)
doublet 1	0.38	0.73	0.34	83
doublet 2	0.39	1.7	0.85	17

6.5.4 Sample annealed at 1250 °C

In the PXRD results given in Fig. 6.20, peaks of cristobalite and β-phase, but also peaks belonging to hematite can be found. In the diffractogram of the samples annealed at 1100, 1250 and 1300 °C, a peak appears that does not correspond to either cristobalite or any Fe_2O_3 phase. This peak can possibly belong to another modification of SiO_2, tridymite, that is usually formed at temperatures lower than temperatures needed for formation of cristobalite.

Size of the β-phase particles calculated using Scherrer equation is 63 nm.

Table 6.27: Peak assignment of the PXRD of the sample $Fe_{1.5}Sc_{0.5}O_3$ annealed at 1250 °C

peak position (°2θ)	20.8	22.0	23.0	24.2	28.4	31.3	32.7	33.2	35.7
corresponding phase	T	C	β	α	C	C	β	α	C
peak position (°2θ)	36.2	37.9	40.3	40.9	42.6	44.8	46.8	48.9	49.5
corresponding phase	C	β	β	α	C	C	C	β	α
peak position (°2θ)	54.7	57.1	60.1	61.8	62.4	63.9	65.1	66.8	68.4
corresponding phase	β	C	C	C	α	α	C	C	C

At this annealing temperature, the Mossbauer spectrum given in Fig. 6.21 shows the β-phase doublet and also the sextet of α phase. The presence of the sextet indicates the transformation of β-phase into hematite, that occurs at higher temperatures. Nevertheless, we can observe the presence of a doublet with remarkably high quadrupole splitting. The origin of the doublet is not clear and we were not able to match it to a specific iron oxide phase or magnetic state. This doublet also appears in the sample annealed at higher temperature.

Table 6.28: Subspectra of Mossbauer spectrum of sample $Fe_{1.5}Sc_{0.5}O_3$ annealed at 1250 °C measured at room temperature

subspectrum	δ (mm/s)	ΔE_Q (mm/s)	B_{hf} (T)	relative area (%)
doublet 1	0.38	0.73	-	71
doublet 2	0.34	2.0	-	8
sextet 1	0.37	-0.21	51.3	21

6.5.5 Sample annealed at 1300 °C

PXRD results of the sample are shown in Fig. 6.20 and peak positions are listed in Tab. 6.29. The sample was annealed at 1300 °C for 4 hours, but the peaks profiles have not changed significantly, only the peaks of hematite have higher intensity than in the diffractogram of sample annealed at 1250 °C.

In the diffractogram, peaks of cristobalite, β-phase and hematite are present. Presence of tridymite peaks is also possible. The SiO_2 matrix is fully transformed into tridymite and cristobalite, there is no wide peak of amorphous phases.

The average β-Fe_2O_3 particles size is 44 nm, what is less than for the sample annealed at lower temperature. It is probable that the transformation into hematite occurs from the surface of each particle. Particles cannot grow anymore and as the β- phase transforms, size of its crystals decreases.

Mossbauer spectrum given in Fig. 6.21 consists of two doublets and a sextet.

Parameters of the most intensive doublet are typical for β-phase, presence of the sextet shows that a part of the sample is transformed to α phase. However, compared to sample annealed at 1250 °C, the decrease in the β-phase doublet intensity is not compensated by the increase in the intensity of hematite sextet and we observe the increase in the intensity of doublet 2.

Table 6.29: Peak assignment of the PXRD of the sample $Fe_{1.5}Sc_{0.5}O_3$ annealed at 1300 °C

peak position (°2θ)	20.7	21.9	23.0	24.2	28.4	31.3	32.5	33.2	35.6
corresponding phase	T	C	β	α	C	C	β	α	α
peak position (°2θ)	36.1	37.9	40.3	40.9	42.6	44.7	46.9	48.5	48.9
corresponding phase	C	β	β	α	C	C	C	C	β
peak position (°2θ)	49.4	54.6	57.0	60.0	61.8	62.4	63.9	65.1	66.8
corresponding phase	α	β	C	C	C	α	α	C	C

Table 6.30: Subspectra of the Mossbauer spectrum of sample $Fe_{1.5}Sc_{0.5}O_3$ annealed at 1300 °C measured at room temperature

subspectrum	δ (mm/s)	QUA (mm/s)	B_{hf} (T)	relative intensity (%)
doublet 1	0.38	0.75	-	46
doublet 2	0.32	1.94	-	28
sextet 1	0.37	-0.20	51.0	26

6.6 Sample $Fe_{1.4}Sc_{0.6}O_3$ V

The sample was prepared in the molar ratio of substituted iron(III) oxide and SiO_2 20:100 and was annealed at three different temperatures, 900, 1000 and 1100 °C.

6.6.1 Sample annealed at 900 °C

Powder X-ray diffraction results in Fig. 6.22 consist of broad band of amorphous matrix at 22 °2θ and four peaks of β-phase at 32.5, 37.8, 54.3 and 64.2 °2θ. No peaks of other phases are present. Particles size calculated using Scherrer's equation is 3 nm.

Mossbauer spectrum given in Fig. 6.23 shows broad peaks that can be fitted with two overlapping Lorentzian doublets. The first of the doublets, the narrow one, belongs to β-Fe_2O_3. Another doublet probably represents superparamagnetic particles of a Fe_2O_3 phase we are not able to determine unambiguously.

Table 6.31: Subspectra of Mossbauer spectrum of sample $Fe_{1.4}Sc_{0.6}O_3$ V annealed at 900 °C

subspectrum	δ (mm/s)	ΔE_Q (mm/s)	width (mm/s)	relative area (%)
doublet 1	0.34	0.96	0.47	56
doublet 2	0.35	1.60	0.53	44

6.6.2 Sample annealed at 1000 °C

The sample annealed at 1000 °C was leached in order to eliminate the broad band belonging to amorphous silica in PXRD results (given in Fig. 6.22). We can observe five peaks of β-phase and two peaks located at 18.1 and 20.1 °2θ having low intensity. The nature of these peaks is unclear. However, there is also a broad

Figure 6.22: Powder X-ray diffractograms of samples annealed at 900 °C, 1000 °C and 1100 °C measured at room temperature. The samples annealed at 1000 °C and 1100 °C were leached

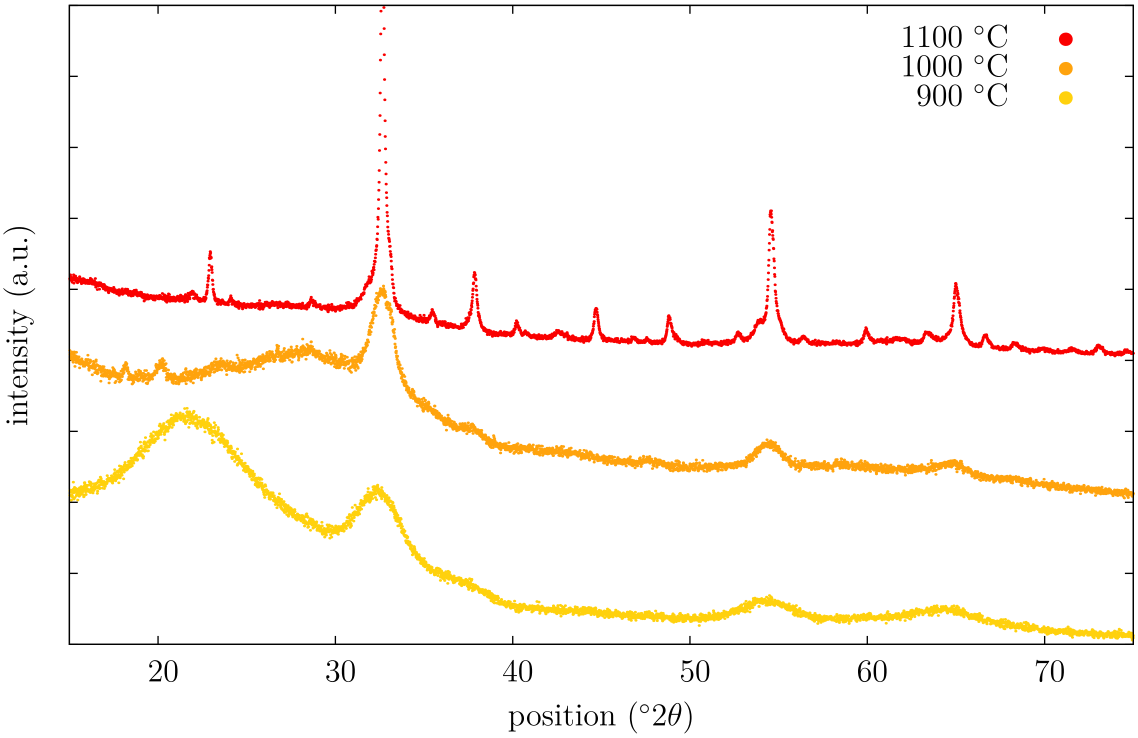

band with the maximum located at 28.5 °2θ, probably representing the reminder of silica matrix. Particles size is 6 nm.

Table 6.32: Peak assignment of the PXRD of the sample $Fe_{1.4}Sc_{0.6}O_3$ V annealed at 1000 °C

peak position (°2θ)	18.1	20.1	32.7	37.7	47.9	54.3	64.6
corresponding phase	?	?	β	β	β	β	β

Mossbauer spectrum shown in Fig. 6.23 can be fitted with a Lorentzian doublet with isomer shift 0.33 mm/s and quadrupole splitting 0.84 mm/s. The peak width is 0.68 mm/s. This value is significantly higher than the value that would correspond to particles with good crystallinity. Particles are present in superparamagnetic state and the sample probably contains β-Fe_2O_3.

6.6.3 Sample annealed at 1100 °C

The sample annealed at 1100 °C was leached and the diffractogram given in the Fig. 6.22 is simple. Next to the peaks of β-phase few peaks of cristobalite appear. When the most intensive signal is reduced, peaks of α-phase are also present. The sample contains β-Fe_2O_3 and hematite and the size of the β-Fe_2O_3 particles calculated using the Scherrer equation is 43 nm.

Mossbauer spectrum given in Fig. 6.23 consists of three subspectra; doublet of β-phase with molar content 68 %, sextet of hematite with molar content 3 %

Figure 6.23: Mossbauer spectra of samples annealed at different temperatures measured at room temperature

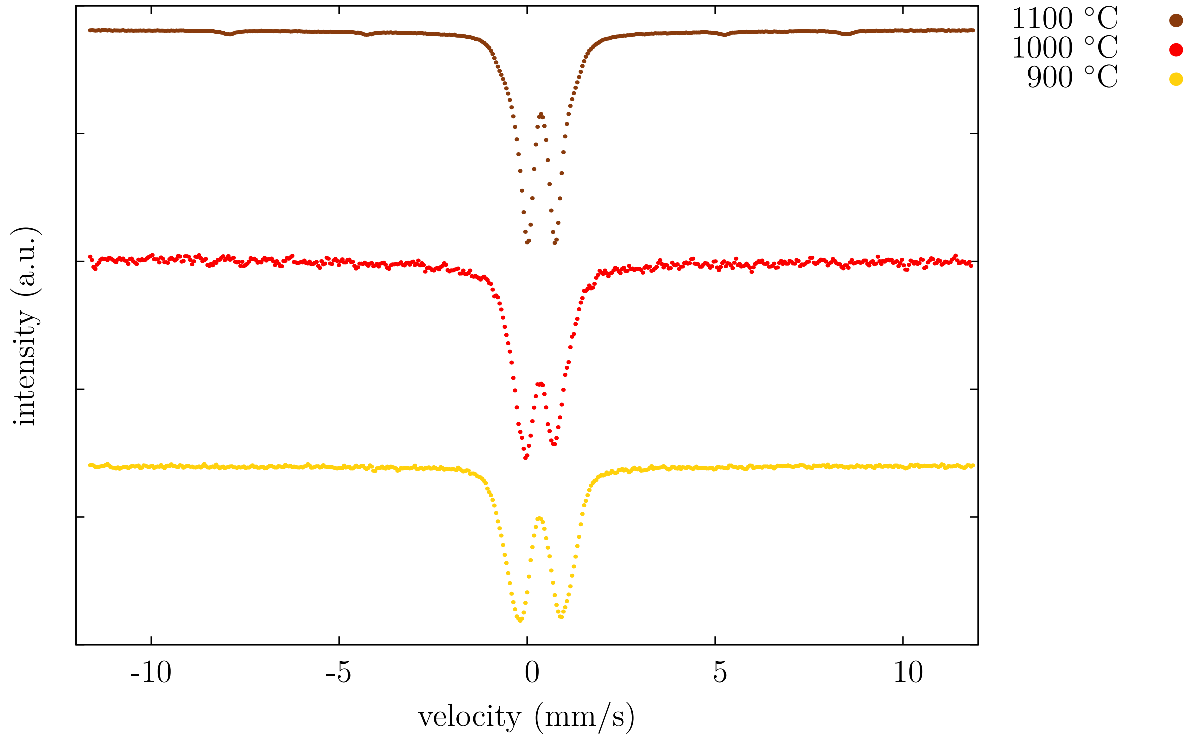

Table 6.33: Peak assignment of the PXRD of the sample $Fe_{1.4}Sc_{0.6}O_3$ V annealed at 1100 °C

peak position (°2θ)	21.9	22.9	24.1	28.6	32.6	35.5	37.8	40.2
corresponding phase	C	β	α	β	β	β	β	C
peak position (°2θ)	42.5	44.7	46.8	48.8	52.7	53.9	54.5	
corresponding phase	C	β	α	β	β	α	β	
peak position (°2θ)	56.4	59.9	63.3	65.0	66.6	68.2	73.0	
corresponding phase	β	C	C	β	β	β	β	

and another doublet with Lorentzian profile.

In the spectra given in Fig. 6.24, transition of superparamagnetic β-Fe_2O_3 to blocked state at temperatures around 30 K can be seen. Compared to the sample $Fe_{1.8}Sc_{0.2}O_3$, the blocking temperature has changed significantly. Although the particles size is larger than in the sample $Fe_{1.8}Sc_{0.2}O_3$ annealed at 1000 °C, (43 resp. 25 nm), the blocking temperature has decreased from 80 K for the sample with low substitution to 30 K for the sample with the high substitution. The measurements at low temperatures were carried out for shorter time, the background is larger than for measurements at room temperature and for this reasons we cannot see the sextet belonging to hematite as its intensity is too low.

Mossbauer spectrum in Fig. 6.25 measured at 4.2 K consists of three subspectra with parameters listed in tab. 6.35. The sextet 1 corresponds to the β-phase. The low intensity sextet can correspond to the small particles of hematite, where the Morin transition is suppressed, but its intensity is insignificant. We were not able to determine the origin of the doublet using the Mossbauer spectroscopy. In the applied field of 6 T at the temperature of 4.2 K the spectrum shows only broad sextet, corresponding to the presence of the antiferromagnetic compound.

Figure 6.24: Mossbauer spectra of leached sample annealed at 1100 °C measured at low temperatures

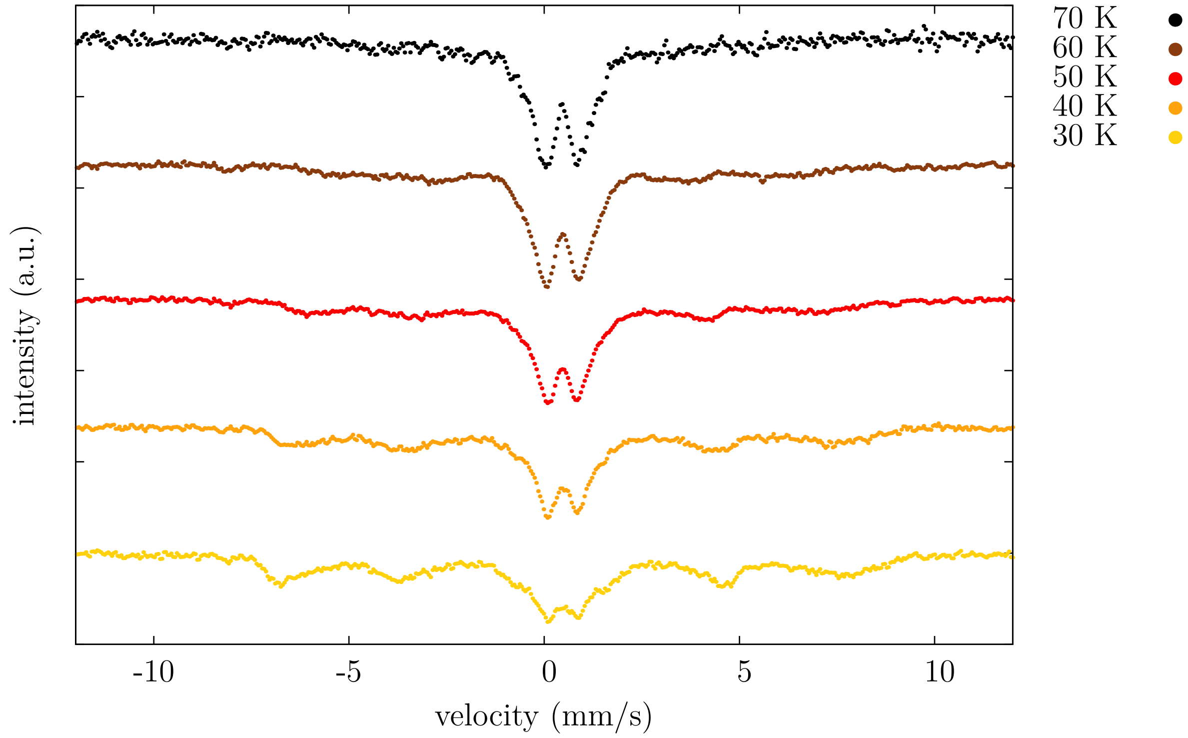

Table 6.34: Subspectra of Mossbauer spectrum of sample $Fe_{1.4}Sc_{0.6}O_3$ V annealed at 1100 °C, measured at room temperature

subspectrum	δ (mm/s)	ΔE_Q (mm/s)	B_{hf} (T)	relative area (%)
doublet 1	0.37	0.73	-	69
doublet 2	0.36	1.4	-	28
sextet 1	0.39	-0.26	51.0	3

Table 6.35: Subspectra of Mossbauer spectrum of sample $Fe_{1.4}Sc_{0.6}O_3$ V annealed at 1100 °C, measured at 4.2 K without applied magnetic field

subspectrum	δ (mm/s)	ΔE_Q (mm/s)	B_{hf} (T)	relative intensity (%)
sextet 1	0.48	0.073	46.9	95
sextet 2	0.43	-0.18	52.9	1
doublet 1	0.45	2.38	-	4

Figure 6.25: Mossbauer spectra of the sample after leaching annealed at 1100 °C measured at 4.2 K in applied field 0 T and 6 T

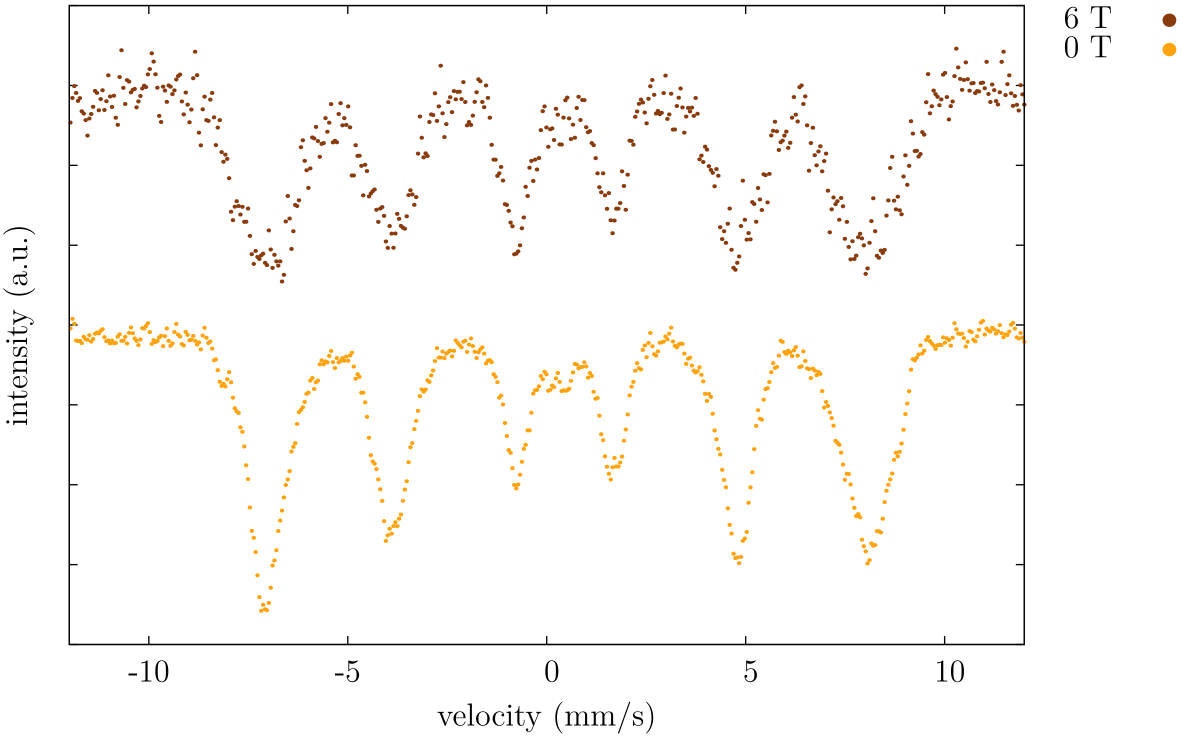

6.7 Sample $Fe_{1.4}Sc_{0.6}O_3$ N

The sample was prepared in lower concentration in matrix and sample was annealed at four different temperatures, 900, 1000, 1100 and 1250 °C.

6.7.1 Sample annealed at 900 °C

In powder X-ray diffraction results given in Fig. 6.26, four wide peaks can be seen. The broad band at 22 °2θ is typical for amorphous phase, next to that, there are four peaks of β-phase located at 32.5, 37.4, 54.3 and 64.3 °2θ. Particles size calculated using Scherrer's equation is 4 nm.

However, the ZFC and FC magnetisation curves in the Fig. 6.27 do not show the antiferromagnetic behaviour of the sample. Due to the increased scandium content (30 molar %), the exchange interactions in β-Fe_2O_3 are weak and magnetisation depends on temperature as $1/T$ following the Curie law for paramagnetic materials.

6.7.2 Sample annealed at 1000 °C

PXRD of the sample is given in Fig. 6.26. The band of amorphous phase at 22 °2θ is still present at this annealing temperature. No signs of cristallization of matrix appear in the diffractogram. Four peaks of β-Fe_2O_3 at 32.5, 37.7, 44.6, 54.4 and 64.7 °2θ are wide, particles size calculated using Scherrer's equation is approximately 7 nm. No peaks of other phases are present.

Figure 6.26: Powder X-ray diffractograms of the samples annealed at 900 °C, 1000 °C and 1100 °C measured at room temperature

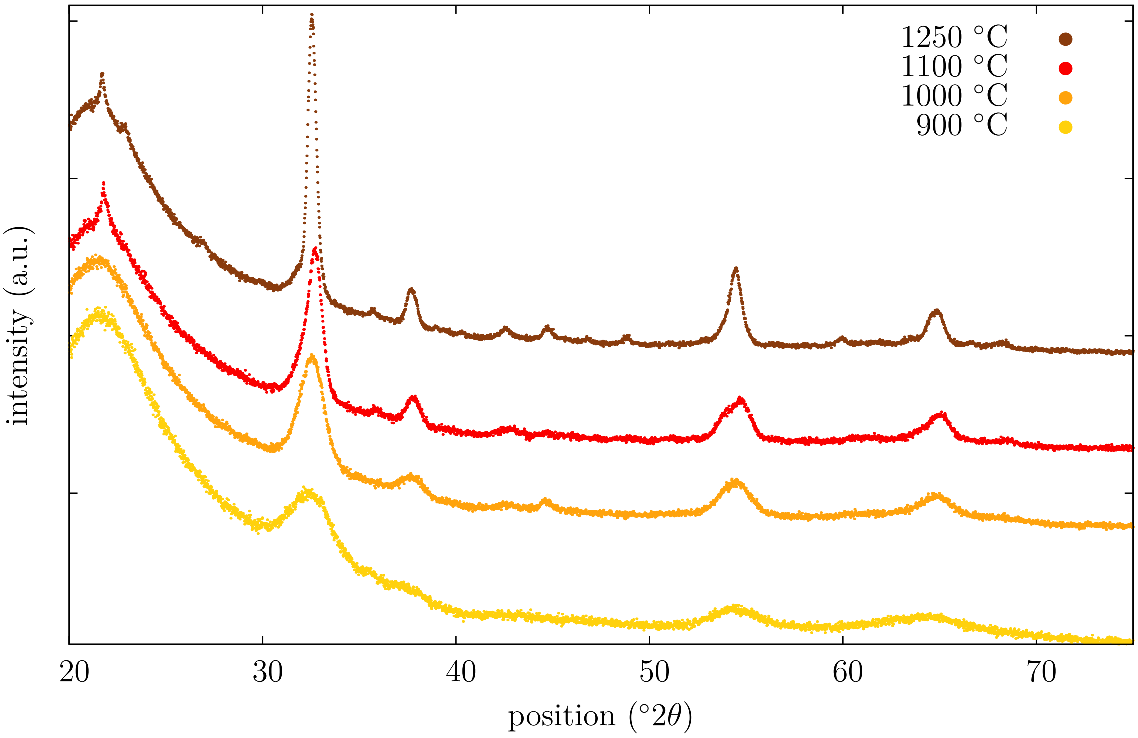

Figure 6.27: ZFC and FC magnetisation curves of the sample $Fe_{1.4}Sc_{0.6}O_3$ annealed at 900 °C measured at 0.1 T

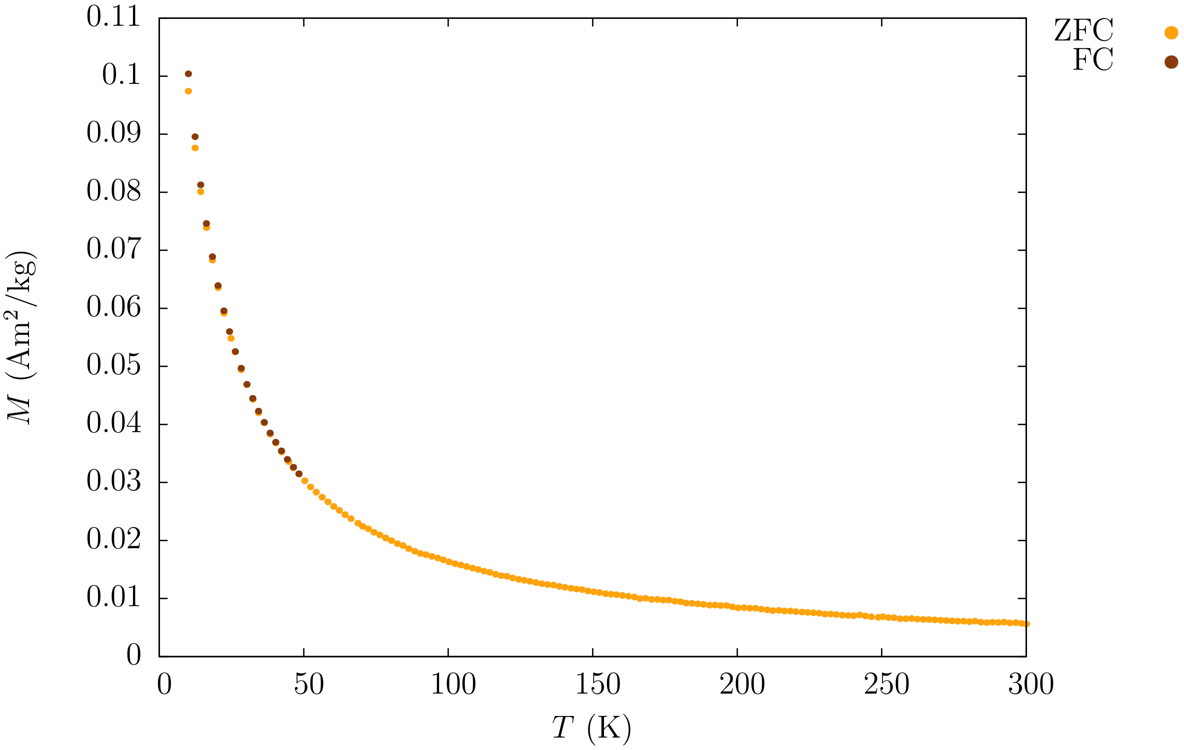

Figure 6.28: Mossbauer spectra of the samples annealed at different temperatures measured at room temperature

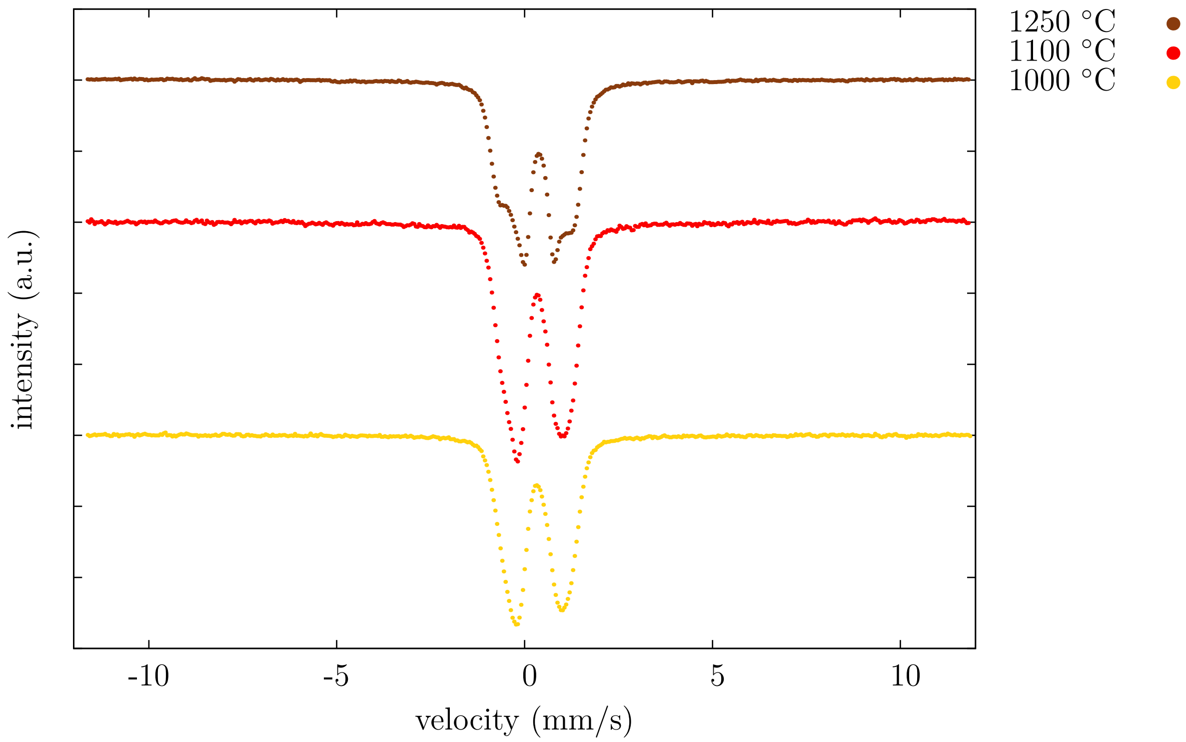

Mossbauer spectrum given in Fig. 6.28 consists of a doublet that can be fitted with a Voigt profile doublet with isomer shift 0.36 mm/s, quadrupole splitting 1.3 mm/s and width 0.67 mm/s.

The profile of this doublet looks different from the doublets of larger β-phase particles. The shoulders are narrower than for Lorentz profile doublet and quadrupole splitting is higher. The distribution of the particles size lead to distribution in the surface atoms number. The atoms on the surface of the particle have different chemical surrounding than the atoms inside, what leads to distribution of the Mossbauer parameters. This distribution is usually Gaussian, that's why the fit with Voigt doublet, which represents the convolution of the Gaussian and Lorentzian profile doublet was used. This fit was then more accurate.

The peak width value is significantly higher than for the phases with good crystallinity. Since no other signals, especially no sextets can be seen, small particles probably of β-phase in superparamagnetic state are present in sample.

6.7.3 Sample annealed at 1100 °C

In this sample, crystallization of the matrix occured. The peak of cristobalite at 22 °2θ appeared, but its intensity is not higher than the intensity of the most intensive peak of β-phase. PXRD results in Fig. 6.26 show ten peaks; two peaks of cristobalite and six peaks of β-Fe_2O_3. Presence of hematite is also possible. The peak assignment is given in Tab. 6.36. Particles size calculated using Scherrer equation is 10 nm.

Mossbauer spectroscopy results given in Fig. 6.28 are almost the same as for

Table 6.36: Diffraction peaks assignment of the PXRD of the sample $Fe_{1.4}Sc_{0.6}O_3$ N annealed at 1100 °C

peak position (°2θ)	32.6	35.9	37.8	44.8	51.0	53.9	54.7	64.8	68.4
corresponding phase	β	C	β	β	C	α	β	β	β

the sample described in the previous section. Spectrum can be fitted with a Voigt doublet with isomer shift 0.36 mm/s, quadrupole splitting 1.3 mm/s and width 0.72 mm/s, what is even more than for the previous sample. The sample probably contains small particles with wide particles size distribution.

6.7.4 Sample annealed at 1250 °C

Powder X-ray diffractogram given in Fig. 6.26 shows peaks of β-phase, a broad band of amorphous phases and the cristobalite peak located at 22 °2θ. β-phase has particularly transformed into hematite. The peaks are narrower than in the samples annealed at lower temperatures, the particles size is 20 nm. Peak assignment is given in the Tab. 6.37.

Table 6.37: Peak assignment of the PXRD of the sample $Fe_{1.4}Sc_{0.6}O_3$ N annealed at 1250 °C

peak position (°2θ)	22.9	32.5	35.7	37.7	42.5	44.7
corresponding phase	β	β	C	β	C	β
peak position (°2θ)	46.8	48.8	54.4	59.9	65.0	68.1
corresponding phase	C	$\alpha + \beta$	$\alpha + \beta$	β	$\alpha + \beta$	C

In Mossbauer spectrum in Fig. 6.28, two subspectra are present. The parameters are listed in tab. 6.38. δ and ΔE_Q of the more intensive doublet are close to typical isomer shift and quadrupole splitting of bulk β-phase. Quadrupole splitting of another doublet is very high and this doublet probably belongs to small particles in superparamagnetic state present in the sample.

Table 6.38: Subspectra of Mossbauer spectrum measured at room temperature of sample $Fe_{1.4}Sc_{0.6}O_3$ N annealed at 1250 °C

subspectrum	δ (mm/s)	ΔE_Q (mm/s)	width (mm/s)	relative intensity (%)
Voigt doublet 1	0.38	0.85	0.42	55
Voigt doublet 2	0.34	2.0	0.46	45

The ZFC and FC magnetisation curves given in Fig. 6.29 do not show the antiferromagnetic behaviour. Compared to the sample with the same scandium concentration annealed at 900 °C, the particles are larger and the structure is more developed. Due to the high scandium amount, the exchange interactions are weak. This leads to the short-distance magnetic ordering and the spin glass behaviour.

Figure 6.29: ZFC and FC magnetisation curves of the sample $Fe_{1.4}Sc_{0.6}O_3$ annealed at 1250 °C measured at 0.1 T

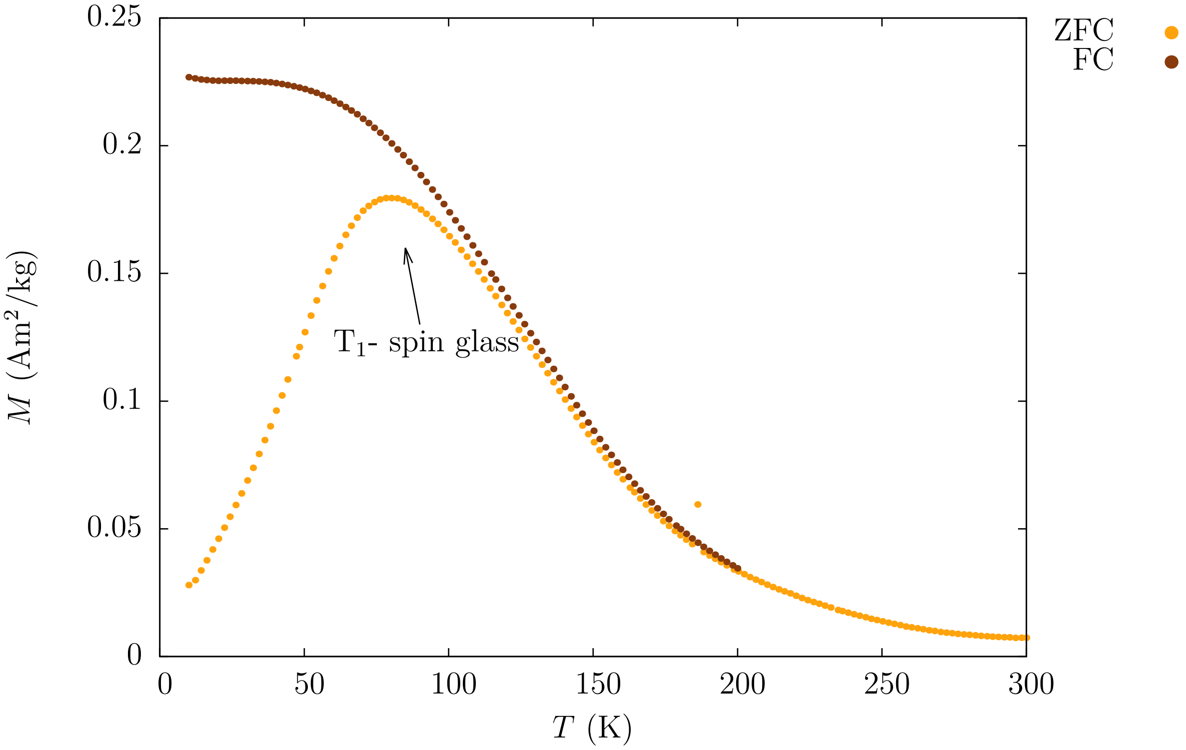

6.8 Lattice parameters

In the diffractograms of all β-$Fe_{2-x}Sc_xO_3$ samples, we can see a shift of the β-phase peak positions. The lattice parameters calculated from the peak position shift for each sample are higher than the standard lattice parameter of β-phase 9.4040 Å and increase with the increasing scandium content.

The reason for the increased lattice parameter is the random distribution of scandium ions in the lattice. Scandium atoms have higher radius and if they are substituted for iron in the lattice, the lattice parameter of the iron (III) oxide increases. Since scandium (III) oxide has the structure of bixbyite, which is isostructural with β-Fe_2O_3, this substitution leads to stabilization of the β-phase structure up to high temperatures. [17]

The plot in the Fig. 6.30 shows the dependence of the lattice parameters of all samples on the scandium content for samples annealed at different temperatures. Scandium content represents the stoichiometric coefficient x from $Fe_{2-x}Sc_xO_3$. The black line represents Végard law, it links the standard value 9.4040 Å for x=0 and the lattice parameter of Sc_2O_3 9.8310 Å for x=2. The uncertainty of lattice parameters is calculated as a standard error of the mean. The multiple values for the samples with x=0.4 and 0.6 represent the lattice parameters of the samples with different concentration of β-phase in matrix.

Figure 6.30: Dependence of the lattice parameter of β-Fe_2O_3 on the scandium substitution for different annealing temperatures

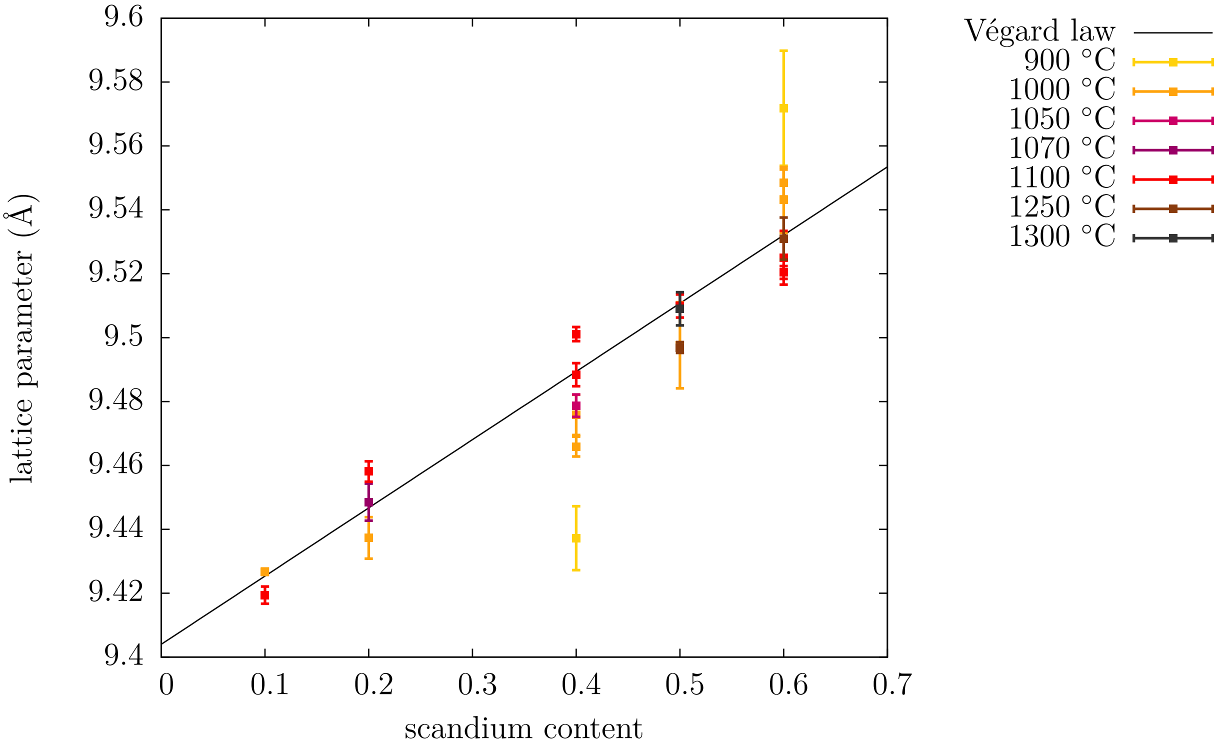

We can see, that the data follow the Végard law within the range of statistical uncertainty. The sample with scandium substitution 0.1 follows the law almost ideally. The lattice parameter value for the sample annealed at 1000 °C is located on the black line and the value for the sample annealed at 1100 °C is only slightly lower. The situation is similar for the samples where x = 0.2. In this case, the parameter of the sample annealed at 1070 °C is located on the line, the value for the sample annealed at 1000 °C is slightly lower and for annealing temperature 1100 °C slightly higher.

The lattice parameters of the samples with x=0.4 and 0.6 annealed at 900 °C are different. The uncertainty of the values is higher than for the samples annealed at higher temperature and the datapoints don't follow the black line that represents Végard law. This behaviour can have different explanations.

First explanation is that at this temperature part of the scandium atoms is present in the amorphous phases in matrix and the real composition of the β-phase has lower scandium content. Then, however, both values should be lower than the predicted value, what is not true for the sample with x=0.6.

The discrepancy between the lattice parameter and Vegard's law can also by explained by imprecise determination of peak positions. If we look at the diffractogram, we can see that the peaks of all samples annealed at 900 °C are very wide. That's why the peak positions obtained by fitting the diffractogram and also lattice parameters calculated using the peak positions can be strongly affected in this case. This is confirmed by the fact that the standard deviations for datapoints that are not in agreement with Végard law are much higher than standard deviations of the lattice parameters of samples annealed at higher temperatures. This would also explain that the lattice parameter is higher than that predicted by Végard law.

Fig. 6.31 and 6.32 show the dependence of the lattice parameter on the scandium content x for the samples annealed at 1000 °C and 1100 °C. We can see that the datapoints for the samples annealed at 1100 °C follow the Végard law better.

Fig. 6.33 and 6.34 show that the lattice parameter increases with the increasing temperature. This could be explained by the fact that scandium incorporates into the lattice more efficiently at higher temperatures, but also by the fact that lattice parameter of a material depends on the particle size, if the size is lower than a critical value.

Qi et al. [46] estimated the magnitude of the particle size effect for the palladium clusters. The relative increase in lattice parameter would be in order of 0.01 % for the increase in particle size from 5 to 40 nm.

The increase in the lattice parameters of here discussed β- phase samples is in order of 0.1 % for the increase in particle size from 5 nm to 40 nm and the effect of scandium substitution and uncertainty of the measurement are significantly higher than the effect of the particles size increase.

In the Fig. 6.35, there is no obvious dependence of the lattice parameter on the annealing temperature and the values for samples annealed at 900 and 1000 °C are significantly higher than the theoretical parameter. The scandium incorporation effect is probably not as strong for higher scandium concentration as for the samples with lower substitution.

In the Fig. 6.34 and 6.35 we can see that the values of the lattice parameters for samples with higher concentration in matrix are higher than for the samples with lower concentration.

The effect of the matrix on the lattice parameters can be estimated by the changed lattice parameter of the sample after leaching. The lattice parameters of

Figure 6.31: Dependence of the lattice parameter of scandium-substituted β-Fe_2O_3 on the scandium substitution for the samples annealed at 1000 °C

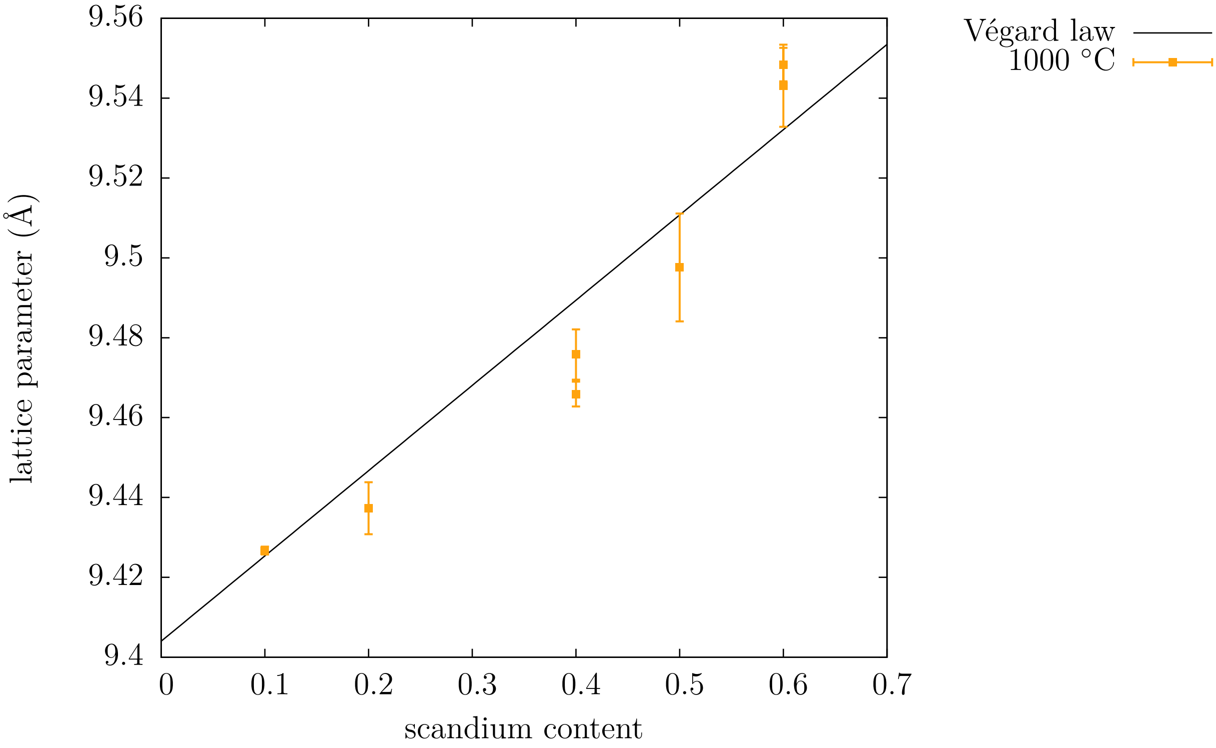

Figure 6.32: Dependence of the lattice parameter of scandium-substituted β-Fe_2O_3 on the scandium substitution for the samples annealed at 1100 °C

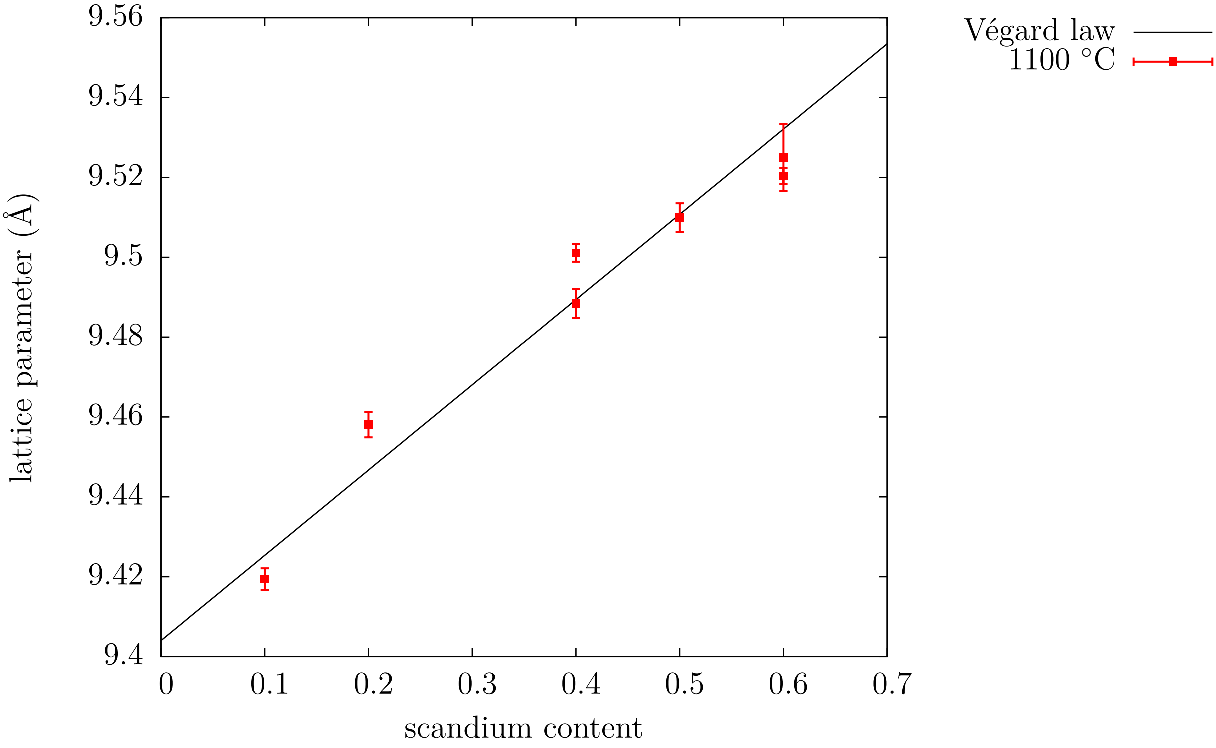

the leached and non-leached samples with x=0.6 annealed at 1100 °C are 9.5204 and 9.5037 Å. The difference is 0.2 %, and so it is possible that the matrix affects the lattice parameter of the embedded particles due to the different coefficient of thermal expansion of the matrix and embedded particles.

Figure 6.33: Dependence of the lattice parameter of scandium-substituted β-Fe_2O_3 on the annealing temperature for the samples with scandium substitution 0.2

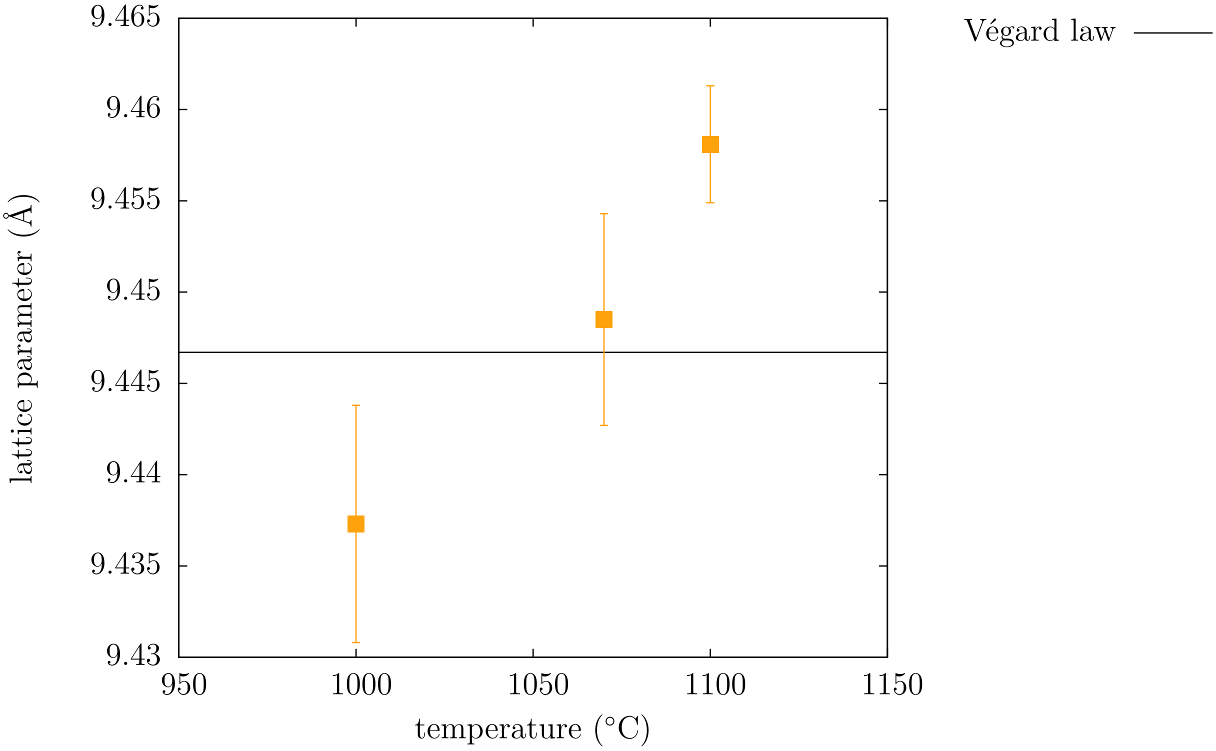

Figure 6.34: Dependence of the lattice parameter of scandium-substituted β-Fe_2O_3 on the annealing temperature for the samples with scandium substitution 0.4 and different concentration in matrix

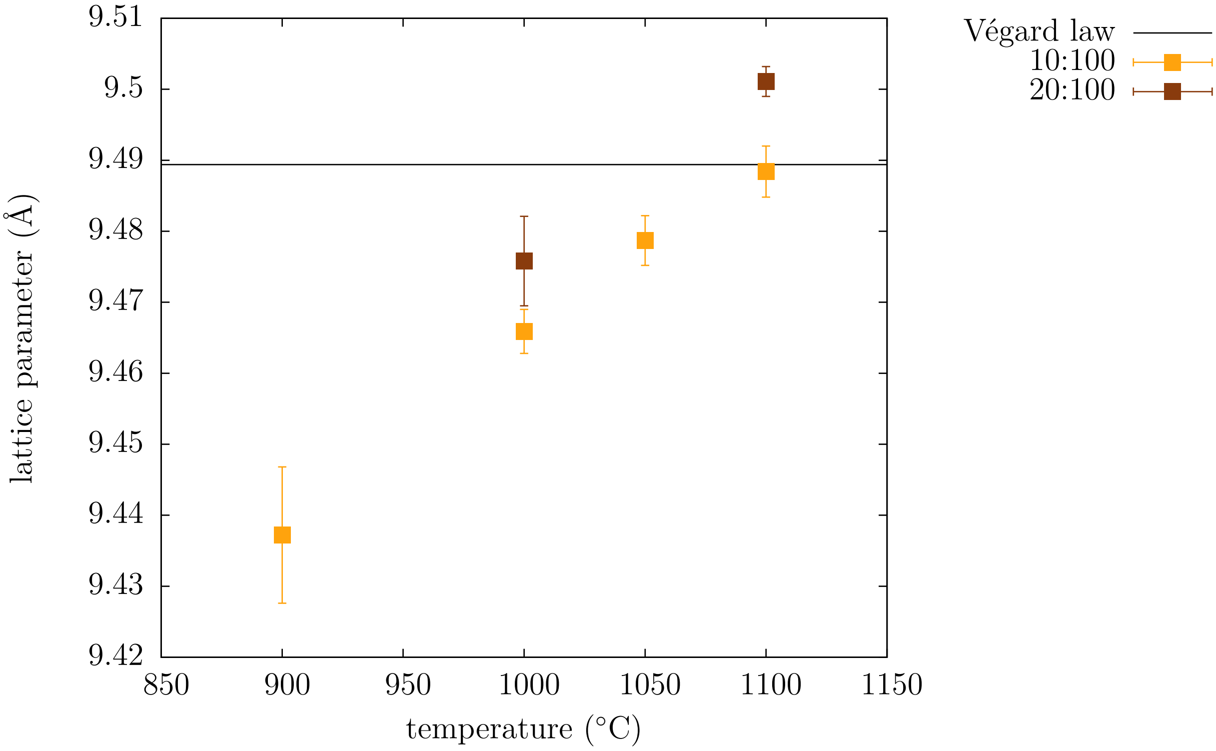

Figure 6.35: Dependence of the lattice parameter of scandium-substituted β-Fe_2O_3 on the annealing temperature for the samples with scandium substitution 0.6 and different concentration in matrix

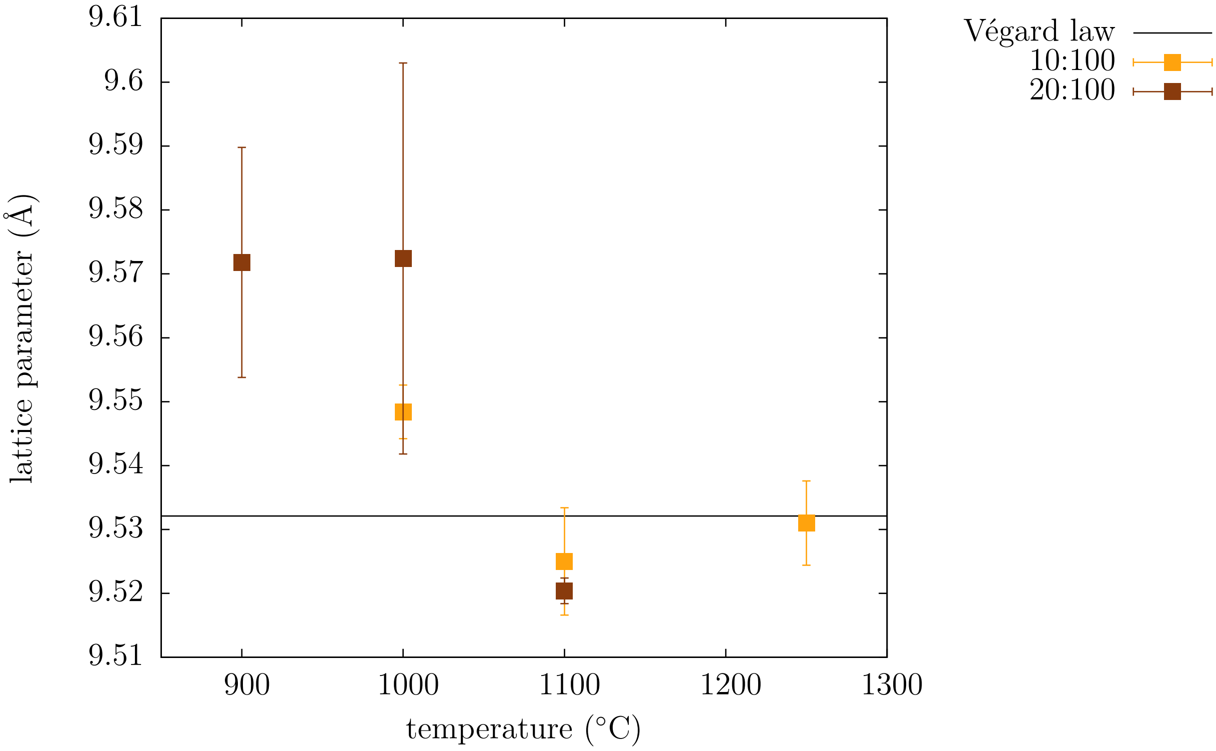

7. Conclusions

The samples of the system Fe_2O_3/SiO_2 substituted with scandium were prepared using sol-gel method. The prepared samples were characterized by powder X-ray diffraction, Mössbauer spectroscopy, electron microscopy and magnetic measurements.

The dependence of the phase composition on the scandium content, annealing temperature and the concentration of the active compound in the SiO_2 matrix was found.

The samples with nominal composition $Fe_{2-x}Sc_xO_3$ annealed at 900 °C showed the presence of γ-Fe_2O_3 except for the samples of higher scandium substitution rate (for $x = 0.4$ and 0.6), where during annealing at 900 °C the β-Fe_2O_3 was formed.

The phase composition of the samples annealed at 1000 °C depended on the scandium content; the samples with the lower scandium content contained mostly ε-Fe_2O_3 while higher substitution rate (x =0.4 to 0.6) led to stabilization of β-phase.

After annealing at 1100 °C, the samples contained β-Fe_2O_3, but the presence of α-Fe_2O_3 (hematite), the most stable phase among the iron(III) oxides was also found. The molar content of hematite in the samples annealed at this temperature did not exceed 10 %.

With the increasing annealing temperature, β-Fe_2O_3 was transformed into hematite and the molar content of hematite increased.

The presence of scandium in the crystal structure was confirmed by the change of the lattice parameter, depending on the scandium substitution rate according to Végard law.

Particle size calculated from Scherrer equation showed increase with increasing annealing temperature. Characteristic particle size value was 4 nm for the samples annealed at 900 °C, for the samples annealed at 1000 °C it was 13 nm and with the increasing temperature it reached 30 to 50 nm in the samples annealed at 1100 °C.

The dependence of the particles size on the concentration of the active compound in the matrix was found. In the samples of nominal composition $Fe_{1.6}Sc_{0.4}O_3$ and $Fe_{1.4}Sc_{0.6}O_3$, the higher concentration in matrix led to formation of larger particles.

The dependence of the blocking temperature on the scandium content was studied. While the sample $Fe_{1.9}Sc_{0.1}O_3$ showed the blocking temperature of 80 K, in the sample of nominal composition $Fe_{1.6}Sc_{0.4}O_3$, the blocking temperature decreased to 30 K.

This study showed that scandium has influence on the phase formation in the system Fe_2O_3/SiO_2. The formation of β-Fe_2O_3 can be controlled by the scandium substitution and this effect can be probably explained by the same crystal structure of Sc_2O_3 and Fe_2O_3.

References

[1] Cornell, R. M., Schwertmann, U. The Iron Oxides. WILEY-VCH verlag GmbH & Co. KGaA Weinheim, 2003.

[2] D. Hradila, T. Grygar, J. Hradilová, P. Bezdička *Applied Clay Science* **22** (2003) 223 – 236

[3] R. A. Dictor, A. T. Bell *Journal of Catalysis* Vol. 97, Issue 1, Jan. 1986, 121–136

[4] W. B. Ingler Jr., S.U.M. Khan *Electrochem. Solid-State Lett.* 2006 volume 9, issue 4, G144-G146

[5] Blake R. L., Hessevick R. E., Zoltai T., Finger L. W. *American Mineralogist* 51 (1966) 123-129 The structure generated using the Diamond software from the cif file.

[6] Bonnevie-Svendsen, M. (1958). *Naturwissenschaften* 45, 542

[7] Braun, H., Gallagher, K. J. *Nature physical science* Vol. 240 November 6 1972

[8] Carraro G., Barreca D., Maccato Ch., Bontempi E., Depero L.E., Fernández C.J., Caneschi A. *CrystEngComm* 2013, 15, 1039

[9] Ikeda, Y., Takano, M., Bando, Y. *Bull. Inst. Chem. Res.*, Kyoto Univ., 64, 249, 1986

[10] Danno T., Asaoka H., Nakanishi M., Fujii T., Ikeda Y., Kusano Y., Takada J. *Journal of Physics: Conference Series* 200 (2010) 082003

[11] Danno T., Nakatsuka D., Kusano Y., Asaoka H., Nakanishi M., Fujii T., Ikeda Y., Takada J. *Cryst. Growth Des.* 2013, 13, 770-774.

[12] Ben-Dor L., Fischbein E., Kalman Z. *Acta Cryst.* (1976). B32, 667

[13] Ben-Dor, L.; Fischbein, E.; Felner, I.; Kalman, Z. *J. Electrochem. Soc.* 1977, 124, 451-457. The structure generated using the Diamond software from the cif file.

[14] Pecharroman C., Gonzalez-Carreno T., Iglesias J. E. *Physics and Chemistry of Minerals*, 1995, Volume 22, Number 1, Page 21 The structure generated using the Diamond software from the cif file.

[15] Sakurai, S.; Jin Jian; Hashimoto, K.; Ohkoshi, S. *J. Phys. Soc. Jpn.* 2005;74(7) 1946–1949. The structure generated using the Diamond software from the cif file.

[16] Machala, L., Tuček, J., Zboril, R. *Chem. Mater.*, 2011, 23 (14), pp 3255–3272

[17] Bréard, Y., Fjellvag, H., Hauback, B. *Solid State Communications.* 151 (2011) 223–226

[18] Gich, M., Frontera, C., Roig, A., Taboada, E., Molins, E., Rechenberg, H. R., Ardisson, J. D., Macedo, W. A. A., Ritter, C., Hardy, V., Sort, J., Skumryev, V. and Nogués, J. *Chem. Mater.* 18 (2006) 3889

[19] Tucek, J.; Zboril, R.; Namai, A.; Ohkoshi, S. *Chem. Mater.* 2010, 22, 6483.

[20] Sergreev, G.B., Klabunde, K. J. Nanochemistry. Elsevier, Amsterdam, 2013. ISBN: 978-0-444-59397-9

[21] Kreibig, U. Z. Phys. D.-Atoms, Molecules and Clusters 1986, 3, 239–249.

[22] N. Takeo. Disperse Systems, Wiley-VCH, 1999. ISBN: 978-3527294589

[23] Klabunde, K. J. Free Atoms, Clusters and Nanosized Particles, Academic Press: San Diego, New York, Boston, London, Sydney, Tokio, 1994.

[24] Cao, G., Wang, Y. Nanostructures and nanomaterials. Imperial college press, London, 2004.

[25] Edelstein, A. S., Cammaratra, R. C. Nanomaterials: synthesis, properties and applications. CRC press, 1998. ISBN: 978-0750305785

[26] Cushing, B.L, Kolesnichenko, V.L, O'Connor, C.J. *Chem. Rev.* 2004, 104, 3893-3946

[27] Wright, J.D., Sommerdijk, N.A.J.M.: Sol-Gel Materials Chemistry and applications. Taylor & Francis Group, 2001. ISBN: 978-9056993269

[28] Brinker, C. J., Scherer, G. W. Sol-Gel science: The Physics and Chemistry of Sol-Gel Processing. Gulf Professional Publishing, 1990. ISBN: 978-0121349707

[29] Coltrain, B.K., Melpolder, S.M., Salva, J.M. *Proc. IV Int. Conf. Ultrastructure Processing of Ceramics, Glasses and Composites,* Wiley, New York, 1989.

[30] Aelion, R., Loebel, A., Eirich, F. *J. Am. Chem. Soc.*, 72, 5705 (1950)

[31] Klein, L.C. *Ann. Rev. Matter. Sci.,* 15, 227 (1985)

[32] Stober,W., Fink, A., Bohn, E. *Journal of colloid and interface science*, 26, 62-69 (1968)

[33] Niznansky, D., Rehspringer, J.L. *Journal of Non-Crystalline Solids* 180 (1995) 191-196

[34] Valvoda, V., Polcarová, M., Lukáč, P. Základy strukturní analýzy. Karolinum, Praha 1992. ISBN: 80-7066-648-X

[35] Vegard, L. *Zeitschrift für Physik*, Volume 5, Issue 1, pp.17-26

[36] Dlouhá, J. Mossbaueruv jev a jeho využití. SNTL, Praha, 1968.

[37] Dickson, D. P. E., Berry, F. J. Mossbauer spectroscopy. Cambridge university press, 2005. ISBN: 978-0-521-01810-4

[38] Brent Fultz, “Mössbauer Spectrometry”, in Characterization of Materials. Elton Kaufmann, Editor (John Wiley, New York, 2011).

[39] Murad, E., Johnston, J. H. “Iron oxides and oxyhydroxides“ in Moossbauer spectroscopy applied to inorganic chemistry, Vol.2. Plenum, New York, 1987.

[40] Pankhurst, Q. A., Pollard, R. J. *J. Phys.: Condensed matter* 2 (1990) 7329-7337.

[41] Zboril, R., Mashlan, M., Petridis, D. *Chem. Mater.* 2002, 14, 969-982

[42] Kittel, Ch. Introduction to Solid State Physics. Czech translation, Academia, Prague, 1985.

[43] Krupička, S. Fyzika feritů a příbuzných magnetických kysličníků. Academia, Praha, 1969.

[44] Bowles, J., Jackson, M., Chen, A., Solheid, P. *The IRM quarterly*, Vol. 19. No. 3.

[45] Binder, K.; Young, A. P. (1986), "Spin glasses: Experimental facts, theoretical concepts, and open questions", *Reviews of Modern Physics* 58: 801–976

[46] Qi, W. H., Wang, M. P., Su, Y. C. *Journal of Materials Science Letters.* 21, 2002, 877 – 878